

POLITECNICO DI MILANO
SCUOLA DI INGEGNERIA INDUSTRIALE E DELL'INFORMAZIONE
CORSO DI LAUREA MAGISTRALE IN INGEGNERIA MATEMATICA



A Mathematical Model to Predict
Glioblastoma Invasion: use of patient-specific
diffusion tensor imaging data in simulations

Master thesis

RELATORE

Prof. Davide AMBROSI

CORRELATORE

Prof. Pasquale CIARLETTA

Dott.ssa Chiara GIVERSO

TESI DI LAUREA DI:

Maria Cristina COLOMBO

MATR. 782447

Anno Accademico 2013-2014

Alla mamma e al papà,
a Fra e ad Emma,
a Dolly

Contents

List of Figures	v
List of Tables	vi
Abstract	vii
Sommario	viii
Ringraziamenti	1
Introduction	5
1 Biological Framework	10
1.1 What is a cancer?	10
1.2 Introduction to brain tumors	13
1.2.1 An overview of brain tumors	13
1.2.2 Classification of gliomas	13
1.3 Glioblastoma Multiforme	16
1.3.1 Hallmark features	18
1.3.2 Diagnosis and treatment	20
2 Diffusion Tensor Imaging	22
2.1 Diffusion Weighted Measurements	23
2.2 Diffusion Tensor Imaging Technique	28
3 Mathematical Model	34
3.1 A continuum theory of mixtures	34
3.1.1 Kinematics	35
3.1.2 The mass balance equation for mixtures	37
3.2 Diffuse interface model for tumor growth	39
3.2.1 Model formulation	39
3.2.2 Constitutive equations	41
3.2.3 Nutrient diffusion	45
3.3 Parameter estimation	47

<i>CONTENTS</i>	iii
3.4 The complete model formulation	49
4 Numerical Implementation	52
4.1 Mesh creation	53
4.1.1 Medical image segmentation	53
4.1.2 Mesh generation	55
4.2 Modeling tensor D and tensor T	58
4.3 Model implementation	64
4.3.1 Continuous weak formulation	64
4.3.2 Numerical model	69
5 Sensitivity Analysis	71
5.1 Preparing the test cases	71
5.2 Sensitivity analysis	76
5.2.1 Cellular evolution: parameters M and k_n	76
5.2.2 Nutrient evolution: parameters δ_n and S_n	77
5.3 Observations and conclusions	80
6 Numerical Tests	85
6.1 Simulating butterfly glioma	86
6.1.1 Numerical implementation of the clinical case	86
6.1.2 Numerical results	91
6.2 Simulating glioblastoma regrowth after resection	96
6.2.1 Numerical implementation of the clinical case	97
6.2.2 Numerical results	101
Conclusions	107
A Code Documentation	110
A.1 Mesh Construction - Numerical background	110
A.2 Code implementation - The FEniCS project	113
Bibliography	126

List of Figures

1.1	How cancer starts	12
1.2	How cancer spreads	12
1.3	Glial tissue's supportive functions	15
1.4	Example of butterfly glioblastoma	19
1.5	Glioblastoma resection	21
2.1	Magnetic field gradients and their effects on the MRI signal	25
2.2	The relationship between water motion and gradient application	26
2.3	Different degrees of DWI in relation to the b factor	28
2.4	Diffusion tensor components	30
2.5	Diffusion components in relation to fibers orientation	31
2.6	Scheme of diffusion properties via ellipsoid visualization	33
2.7	Depiction of the eigenvalues, mean diffusivity, FA and a color map of the fiber orientation	33
3.1	Schematic diagram of cells' behavior in relation to Σ	45
3.2	Nutrients diffusion through ECM	47
3.3	Exerted pressure in a glioblastoma	50
4.1	T1 image used for mesh creation	54
4.2	Segmented images of the brain.	54
4.3	Segmented glioblastoma tumor overlapped to the brain map	54
4.4	Mesh surface before and after smoothing and cleaning steps	55
4.5	3D mesh before and after the refinement of the tumoral area	56
4.6	Labeled mesh	57
4.7	Diffusion tensor - medical images	59
4.8	Patient-specific components of tensor \mathbf{D}	62
4.9	Mean Diffusivity	62
4.10	Patient-specific components of tensor \mathbf{T}	63
4.11	Initial normal profile of the cellular fraction	65
4.12	Initial distribution of ϕ on the brain mesh - plane xy	65
4.13	Initial tumor shape	66
4.14	Initial distribution of n on the brain - plane xy	67

5.1	Initial normal profile of ϕ	75
5.2	Initial ϕ concentration on the brain mesh - plane xy	75
5.3	Legend of the symbols Δx , Δy and Δz	76
5.4	How profiles are obtained	81
6.1	Anatomy of the corpus callosum	87
6.2	Frontal and occipital butterfly glioblastoma	87
6.3	Fractional anisotropy - medical image	88
6.4	Location of initial tumor	89
6.5	Initial configuration of ϕ and n	89
6.6	Plot of k_n over a clipped mesh along xy and yz planes.	91
6.7	ϕ concentration in relation to T_{xx} values	93
6.8	ϕ concentration in relation to T_{ii} values	94
6.9	ϕ concentration in relation to k_n	95
6.10	ϕ concentration at t=25 days in relation to k_n - isotropic simulation	96
6.11	Manually segmentation of glioblastoma	97
6.12	Different regions on the mesh	98
6.13	3D sketched of the tumor mass and survivor cells	98
6.14	k_n concentration over a clipped mesh	99
6.15	S_n concentration over a clipped mesh	100
6.16	Diagonal components of tensor \mathbf{T}	100
6.17	Diagonal components of tensor \mathbf{D}	101
6.18	Refined mesh - Resection test	101
6.19	ϕ and n concentration development in plane xz - resection test	104
6.20	ϕ and n concentration development in plane yz	104
6.21	Detail of ϕ and n at t=20 days	105
6.22	Clipped thresholded ϕ and n concentration in relation to D_{xx}	105
6.23	Clipped thresholded ϕ and n concentration in relation to k_n	106
6.24	Volumetric growth of glioblastoma	106
A.1	The FEniCS project	114

List of Tables

1.1	Type of cells, tissues and tumors	14
1.2	WHO grading system for gliomas	16
1.3	Incidence rates, age and sex, and survival of patients with gliomas	17
3.1	Parameters Estimation	49
5.1	Biological parameters - Sensitivity analysis I	77
5.2	Biological parameters - Sensitivity analysis II	77
5.3	Numerical results concerning ϕ - Sensitivity analysis I	78
5.4	Numerical results concerning ϕ - Sensitivity analysis II	79
5.5	ϕ profile - Sensitivity analysis I	82
5.6	Plots of n variables at $t = 0$ - Sensitivity analysis II	83
5.7	ϕ and n profile at the final time step - Sensitivity analysis II . . .	84
6.1	Diagonal components tensor T in the ROI	90
6.2	ϕ and n concentration, clipped mesh xy plane - butterfly and isotropic simulations	92
6.3	Tumor volume overlapped to the maps of T_{ii}	94
6.4	ϕ and n concentration at different time steps - Resection test . . .	103

Abstract

Even though brain tumors account for only 2-3% of all cancers, they are responsible for 7% of the years of life lost from cancer before the age of 70. Among them, the most aggressive is the glioblastoma, a highly malignant cancer that arises in the neuroglia, the supportive tissue of the neurons. Glioblastoma presents long extensions that infiltrate deeply the white matter, following the alignment of the fibers. From the medical viewpoint, this peculiarity makes it difficult to treat. For the same reasons, in the last years, biomathematical modeling applied to infiltrative brain tumor has gained in importance. Indeed, a good model could offer a better understanding of the microstructural dynamics of the cancer and thus it could be helpful to predict its evolution. In this study, we propose a diffuse interface binary mixture model which consists of a fourth order non-linear equation for the cancerous cellular fraction coupled with a reaction diffusion equation for the nutrient component. The model takes into account the mechanical dynamics, e.g. adhesive forces or viscous interactions among cells, and the chemotactic cellular movement in response to certain environment factors. Moreover, we include brain tissue heterogeneity and anisotropy in the model by the introduction of patient-specific diffusion tensor imaging data, thanks to which we manage to probe brain fibers architecture. The aim of this research is to demonstrate the importance of considering anisotropy, heterogeneity and patient-specific data into mathematical models in order to better predict the tumor growth. Specifically, we deal with the theoretical and the numerical framework of the mathematical model proposed. Starting from a real MR of a patient affected by glioblastoma and using imaging techniques, we create a patient-specific computational mesh and we extract the necessary data from the DTI medical images. Then we develop numerical codes making use of an open-source software name FEniCS. To study the anisotropic development of the tumor in relation to the biological parameters presented in the model, we perform a sensitivity analysis on a homogeneous geometry. Finally, we provide two numerical tests that simulate common clinical situations.

Sommario

Sebbene i tumori cerebrali rappresentino solamente il 2-3% delle diagnosi tumorali, essi sono i responsabili del 7% di morti annue causate dal cancro prima dei 70 anni di età. Tra di essi il più aggressivo è il glioblastoma, un cancro altamente maligno che si sviluppa nella neuroglia, il tessuto di supporto dei neuroni. Il glioblastoma presenta lunghe estensioni che infiltrano la materia bianca in profondità, seguendone l'allineamento delle fibre, e che rendono questo tipo di tumore molto difficile da trattare. Per questa ragione, negli ultimi anni, la modellizzazione matematica dei tumori cerebrali infiltrativi ha acquisito sempre più importanza. Un buon modello può infatti offrire una migliore comprensione delle dinamiche microstrutturali del cancro e di conseguenza potrebbe essere utile nel predire la sua evoluzione. In questo progetto, proponiamo un modello di miscela binaria ad interfaccia diffusa che consiste di un'equazione del quarto ordine per la frazione volumica cellulare accoppiato con un'equazione di diffusione reazione per la componente dei nutrienti. Il modello prende in considerazione le dinamiche meccaniche, come le forze di adesione o le interazioni viscosse che hanno luogo tra le cellule, e il movimento chemotattico cellulare causato da fattori chimici presenti nell'ambiente extracellulare. Inoltre, abbiamo introdotto nel modello l'eterogeneità e l'anisotropia, caratteristiche peculiari del tessuto cerebrale, utilizzando i dati medici reali del tensore di diffusione, grazie al quale possiamo anche conoscere l'architettura delle fibre cerebrali. Lo scopo di questa ricerca è dimostrare l'importanza di introdurre l'eterogeneità, l'anisotropia e i dati paziente-specifici nel modello matematico così che la predizione della crescita tumorale sia migliore e più veritiera. Nello specifico, in questo lavoro di tesi, ci siamo occupati dello sviluppo teorico e numerico del modello proposto. In particolare, attraverso tecniche di imaging medico, abbiamo creato una mesh computazionale di un cervello estrapolando la geometria da una risonanza magnetica di un paziente affetto da glioblastoma e abbiamo estratto i dati reali da introdurre nel modello dalle immagini mediche del tensore di diffusione. Abbiamo inoltre sviluppato codici numerici utilizzando un software open-source chiamato FEniCS. Per studiare la crescita anisotropa del tumore in relazione ai parametri biologici presenti nel modello, abbiamo realizzato un'analisi di sensibilità su una geometria omogenea. Infine, abbiamo proposto due test numerici che simulano situazioni cliniche comuni.

Acknowledgments

Desidero ringraziare tutti coloro che mi hanno sostenuto e aiutato durante questo periodo di tesi.

Innanzitutto, vorrei ringraziare il mio relatore ufficiale, il professore Pasquale Ciarella, per avermi proposto un argomento così interessante e ostico. Le nozioni matematiche e numeriche che ho acquisito in questo anno sono notevoli, ma ancor più notevole è stata l'esperienza da "ricercatrice" che ho sperimentato. Ho potuto comprendere, almeno un po', cosa significa essere un ingegnere matematico che fa ricerca, che tenta di comunicare con altre figure che molto spesso non capiscono il suo linguaggio, che cerca di trovare modelli là dove nessuno ci ha mai pensato prima. Ho avuto modo di mettermi a confronto e di conoscere il mondo della medicina, che sempre mi ha affascinato e spaventato.

Colgo l'occasione dunque per ringraziare i medici dell'Istituto Neurologico Carlo Besta per essere stati disponibili e per aver soddisfatto le mie richieste. In particolare, ringrazio il dottor Carlo Boffano per aver fornito i dati medici di cui necessitavo e senza i quali questo progetto non avrebbe potuto essere realizzato; e il dottor Francesco Acerbi per aver risposto ai miei dubbi e per aver dimostrato particolare interesse e fiducia verso questa ricerca.

Vorrei ringraziare ora le persone che mi hanno aiutato nell'affrontare e nello sviluppare questo lavoro. Ringrazio Elena Faggiano per avermi insegnato le tecniche base di imaging e per essere stata disponibile ad incontrarmi, e Matteo Manica, il quale indirettamente mi ha fornito i codici numerici dai quali sono partita. Più di tutti vorrei ringraziare la mia correlatrice, la dottoressa Chiara Givero, il cui aiuto

è stato fondamentale per la buona riuscita di questo progetto. La ringrazio profondamente perché ha sempre risposto ad ogni mia domanda e ha sempre sanato ogni mio dubbio, la ringrazio perché mi sono sentita libera (forse fin troppo) di esprimere ogni mia perplessità e paura, la ringrazio perché ha ascoltato i miei sfoghi e mi ha salvato da possibili esaurimenti nervosi. A lei in parte devo il fatto che sono arrivata fin qui.

Desidero ora ringraziare i miei cari e i miei amici, che insieme a me hanno vissuto e affrontato il periodo universitario.

Un grazie enorme va alla mia famiglia, perché, nonostante tutti i difetti che abbiamo, siamo la famiglia migliore del mondo. Vorrei ringraziare il papà per avermi sempre sostenuto, economicamente e moralmente, e per avermi dato la possibilità di arrivare fino a qui, fino ai 25 anni, senza fare nulla e senza farmi mancare nulla. Ringrazio la mamma per essere la mamma, per essere "tutto", per avermi aiutato sempre, per aver dato importanza ad ogni mio respiro e ad ogni mia lacrima, per aver vissuto con me ogni mio affanno e per avermi spronato a fare meglio quando avevo paura. La ringrazio perché mi diceva sempre di smettere di studiare e perché mi trascinava al supermercato per farmi prendere un po' d'aria. Ringrazio mia sorella maggiore Francesca, per aver condiviso con me tutta la sua vita, per essere unica, per avermi dato consigli, per aver instaurato con me un rapporto speciale, irriproducibile, vero. Ringrazio mia sorella minore Emma, perché è il sole di questa casa, perché riesce a farci ridere e a farci litigare, perché ci fa impazzire e ci fa sognare, perché mi fa vivere il liceo una seconda volta e perché, da quando Fra si è laureata, ha condiviso con me il tavolo della cucina. Ringrazio Dolly, anche se non c'è più. Mi manca da morire, ogni giorno di più. È il ricordo più vivido e ricorrente nei miei pomeriggi di studio. Mi ha tenuto compagnia nei periodi invernali dormendo sulla sedia al mio fianco, quando la mia famiglia andava a fare compere il sabato pomeriggio, e si è fatta invidiare nei periodi estivi quando mi preparavo per le sessioni estive e lei sonnecchiava nell'angolo più fresco della casa.

Desidero ringraziare i miei compagni e amici di università e in particolare il gruppo degli "Ingegneri Matematici Belli Ma Non Troppo" per aver reso questi anni di studio un po' meno sofferti, trasformando le sere di studio in biblioteca in archi-party. Vi ringrazio perché abbiamo saputo mantenere i nostri obblighi senza dimenticare di divertirci. Vi ringrazio perché avevate un modo di vivere e di pensare uguale al mio, ed è stato bello trovare un gruppo di amici così affiatato in un periodo della vita dove le amicizie vanno disperdendosi. Vi ringrazio per tutto, per avermi dato un letto a Milano, per aver reso questa città anche un po' mia, per le serate all'Alcatraz, per le cene di Natale, per le cene e basta, per le gite fuori porta, per ogni esame affrontato, per ogni minima stupidata che abbiamo fatto, per tutto. Vorrei ringraziare il mio gruppo di calcolo ed, in particolare, il mio gruppo del Compatto per aver condiviso le fatiche del quarto anno e per aver odiato e continuare ad odiare quelli di finanza. Vorrei ringraziare sopra tutti e tutto Elisa e Francesca, perché siete "belle belle belle". Ringrazio Elisa perché è stata un appoggio sicuro in questi ultimi anni, e, nonostante all'inizio ci tenevamo alla larga forse perché io piangevo troppo e lei aveva collanine con croci al contrario, si è rivelata un'amica sincera. E' la mia Miley. Ringrazio Francesca perché mi fa sentire importante e perché parla tanto. Non mi sono mai annoiata con lei e mi fa vedere la vita da un punto di vista diverso. Mi ha spiegato che differenza ci fosse tra cipria e fard e mi ha sgridato quando avevo comportamenti infantili.. anche se ci resto male ogni volta, so che lo fa per farmi diventare migliore. Ringrazio Luigi, per essermi stato vicino in questi ultimi due anni durante i quali ha saputo sempre ascoltare le mie lamentele e i miei deliri. Ringrazio la sua sensibilità e la sua capacità di analizzare la vita e le persone che ci circondano.

Ringrazio le mie amiche del liceo, Silvia, Dani e Lara, per esserci sempre e per essere cresciute con me in questi 10 anni. Più di tutti, un grazie sincero va a Silvia, perché la sua amicizia è stata unica e preziosa.

Ringrazio anche la mia squadra di Kung Fu, la mia insegnante e il Kung Fu in sé.

In questi anni di frequentazione, ho avuto modo di staccare la spina dal mondo astratto della matematica e di imparare a muovermi nella geometria reale, di avere coscienza dello spazio, impegnandomi in qualcosa di fisico e accorciando le distanze tra pensiero e movimento.

Ed infine ringrazio Jacopo, solo perché vuole essere ringraziato per battere il suo stesso record di ringraziamenti su tesi universitarie. Dovrei anche ringraziare il suo computer, perché grazie ai suoi quattro core, mi ha aiutato moltissimo ad abbattere i tempi delle simulazioni. Dovrei forse però ringraziare Jacopo anche per essermi stato sempre vicino quest'anno e per avermi sempre e incondizionatamente sopportato, per aver cercato con me soluzioni che da sola non riuscivo a trovare, per aver accolto le mie lacrime sulla sua spalla e per aver risposto ad ogni mio sorriso con un sorriso. Lo ringrazio perché quando ho perso le speranze e quando sono stata stanca di lottare e di pensare, la sua presenza mi ha fatto dimenticare tutto e tutti. Lo ringrazio perché è curioso ed intelligente e ha sempre dimostrato interesse alle cose che facevo e studiavo, nonostante non ci capisca molto di matematica. Lo ringrazio perché è un cuc, e spero che lo rimanga per sempre.

Introduction

Primary brain tumors are the most aggressive and lethal forms of cancer [75], and, although they account for only 2-3% of all human malignancies, they are nevertheless responsible for 7% of lives lost from cancer before the age of 70 per year [19]. In human brain, moreover, more than 120 different tumor types can be found among which gliomas are the most prevalent form [23]. They are tumors that arise from neoplastic glial cells, the supportive tissue of the neurons, and account for the 30-40% of all brain and central nervous system primary tumors and the 80% of the all malignant brain tumors [21, 23].

The most common and also the most malignant glioma is the **glioblastoma**, which will be the clinical focus of this dissertation. Despite of therapies (surgery resection, chemotherapy or radiotherapy), glioblastoma has a life expectancy, after been diagnosed, of only fourteen months [69, 75], while only 5% of patients has a five years survival [21]. Thus, this disease represents a real challenge for present day oncology. Moreover, its capability of penetrating diffusely along the white matter fibers leads to a wide tumoral area underestimated by conventional imaging technology, such as computed tomography (CT) and magnetic resonance imaging (MRI). Consequently, invasive glial neoplasms are difficult to be completely resected, and while all visible tumor cells can be removed, the invisible infiltrating tumor components are left behind. For this reason, the extent of resection in glioblastoma medical treatment has been a big dilemma in the last decades. Furthermore, another challenging aspect of surgery is related to the location of the tumor. As a matter of fact, tumor resection could be potentially harmful if the tu-

mor is located near a sensitive area of the brain such those which control language, movement, vision or other important functions.

To better detect tumors and evaluate their invasiveness, in the early 90s a new imaging technique called Diffusion Tensor Imaging (DTI) was developed [30]. The DTI is the only non-invasive method for characterizing the microstructural organization of tissue *in vivo*, so it is understandable why this technique has attracted huge interest and has enjoyed a rapid uptake by clinical and neuroscientific communities.

At the same time, a big help to present day oncology is potentially represented by biomathematical modeling. During the last decades, indeed, the capability of tumor to grow and invade the surrounding tissue has gained also the attention of the mathematical and the physical research communities. The goal of this new field of research is to understand the dynamics behind tumor growth and expansion in relation to the specific features of the environment in which the neoplasm is evolving in order to provide a good mathematical model able to predict tumor evolution, to improve therapy planning and to prognosticate the result of a specific form of treatment. Thus, during the last fifty years, driven by the ambition of providing a good and truthful model, theoreticians have proposed different mathematical models, covering various morphological and functional aspects of carcinogenesis.

As concerns the field of infiltrative brain tumor, such as gliomas, the basic spatio-temporal model was suggested by J.D. Murray in the early 1990s. He proposed a simple conservative diffusion equation for cells concentration observing that the main aspect of the cancer was the uncontrolled proliferation of cells and the capability of them to invade and diffuse in the host tissue. The model can be stated as:

the rate of change in tumor cell population =
the diffusion (motility) of tumor cells + the net proliferation of tumor cells.

Under the assumption of a classical gradient-driven Fickian diffusion, this state-

ment leads to the mathematical formulation of the following equation:

$$\frac{\partial c}{\partial t} = \nabla \cdot (D \nabla c) + \rho c \quad (1)$$

where $c(\mathbf{x}, t)$ is the tumor cell density at location \mathbf{x} and time t , D is the diffusion coefficient representing the net motility of glioma cells and ρ represents the net proliferation rate of glioma cells [22]. In the last ten years, Swanson et al. have been working on the development of this kind of model, introducing brain anisotropy [71], angiogenesis [73], and modeling therapeutic response [72].

In contrast to diffuse models, in the mid-1990s, **multiphase models**, whose theoretical framework has to be found in the theory of mixture, started to be used in biological research and in particular in the study of tumors. The multiphase approach was novel insofar as the tumor is considered as a continuum comprising two or more interacting constituents, called *phases*. The mechanical aspects of biological tissues are also introduced in governing equations, which are now driven from mass and momentum balances. Among multiphase models, an interesting model was proposed by Byrne and Preziosi [8] in the early 2000s. They proposed a **binary model** in which the tumor cells phase and the extracellular water phase are taken into account and they showed that cellular motion is a consequence of interaction between cells instead of being determined by random motility. In the same period Ambrosi and Preziosi [1] have explained the necessity to propose some postulates for cell velocity and the corresponding displacement field in order to close the model, derived from the mixture theory. In the same area of research, in 2007 Lowengrub et al. [83] developed, analyzed and numerically simulated a **diffuse interface continuum model**, which was derived using the energy variation statement and thus it was thermodynamically consistent.

Following [1, 8, 83] in the present work we propose, analyze and simulate a diffuse interface binary mixture model of glioblastoma tumor growth. The model is well posed and consists of a fourth order non-linear equation for the tumoral

cells' volume fractions coupled with a reaction-diffusion equation for the nutrient component. We consider the oxygen as the main source of supply and we hypothesize that the vasculature is homogenous in the whole domain. The model takes into account the mechanical aspects involved in tumor evolution, such as adhesive forces or viscous interactions, and the micro-local environment conditions such as the oxygen levels. Hence, in the governing equation of the cellular fraction we consider a term of flux of mass which, biologically, is due to a particular phenomenon of cellular migration called **chemotaxis**. Indeed, it has been experimentally demonstrated [16] that a cell can perform a directed migration in response to certain increasing gradient of chemoattractants, such as nutrients. Furthermore, observing that the glioblastoma is a highly infiltrative tumor, whose extensions diffuse deeply along white matter structures, we introduce the concept of **anisotropy** thanks to **patient-specific diffusion tensor imaging** data. As mentioned, this technique provides a tensor that describes the spatial diffusion of the water molecules in cerebral tissues and, comparing the diffusion values along each direction, we are able to know which is the structure of the fibers and which are the preferential directions of movement. Indeed, a water particle will move more easily along a fiber than perpendicularly to it because, along that path, it will not find any obstacles. In consequence, handling with the diffusion tensor we obtain a new tensor that we call **tensor of preferential directions** and that we include in the chemotactic term. By the inclusion of the anisotropic tensor of preferential directions, the model is thus able to reproduce the cellular motion along the fibers of the white matter. Finally, we suppose that the oxygen particles coherently with the water molecules and thus the diffusive behavior of the nutrients can be actually described by the water diffusion tensor, obtained directly from the medical images.

In our work we also deal with the implementation of the computational mesh and the numerical codes necessary to simulate the model. In particular, we obtain the computational mesh extracting the geometry from a magnetic resonance of a patient affected by glioblastoma, gently provided by Istituto Neurologico Carlo Besta,

and we discretize and numerically solve the problem using the **finite elements method** implemented in FEniCS. Consequently, we focus on simulating two specific clinical cases: the first concerns the growth of a butterfly glioblastoma, a kind of astrocytoma that arises in the midline of the brain and assumes a peculiar shape; the second deals with a common medical situation in which the glioma is not completely removed by surgical intervention and tumoral cells are left behind. We thus investigate the potential occurrence of metastasis in the site of resection.

The work is organized as follows: in **Chapter 1**, we describe the biological framework of the research, such as the phenomenon of carcinogenesis, and in particular we focus on brain tumors and on glioblastoma malignancy and features. In **Chapter 2**, diffusion MRI technique is briefly described and the details on diffusion tensor imaging, useful to understand the mathematical model, are given. The first part of **Chapter 3** is dedicated to the theory of mixture while in the second part the mathematical model is introduced. In the last part of this chapter the ranges of the biological parameters of the glioblastoma are discussed. In **Chapter 4** the numerical formulation is provided. In the first part we describe the imaging and the computational techniques used to create the 3D brain mesh. In the second part of the chapter, it is explained how the diffusion tensor information are introduced in the model and how the tensor of the preferential directions is obtained. Finally in the last part of Chapter 4, the continuous and discrete weak formulation is developed and some details about the numerical method adopted are provided. In **Chapter 5**, the sensitivity analysis to the biological coefficients present in the model is presented. In **Chapter 6** we describe and numerically simulate the cases of interest mentioned before. All the codes we make use of and more details about numerical methods are provided in **Appendix A**.

Chapter 1

Biological Framework

In this chapter we provide a biological framework of the problem in order to better understand which reasons are guiding our work and why a mathematical model of glioblastoma is highly required. So, in the first section we briefly explain the process of *carcinogenesis*, which literally means "the creation of a cancer". In the second section we focus on brain tumors and, among them, we concentrate on a specific group of brain cancers named gliomas. In the third section we illustrate the features of the glioblastoma, whose biological description is the object of this dissertation.

1.1 What is a cancer?

A multicellular organism can thrive only when all its cells function in accordance with the rules that govern cell growth and reproduction. In a healthy body cells control their proliferation and program their death (apoptosis) in the various tissues so as to optimize body repair and healing. Sometimes it can happen that this process breaks down, i.e. a mutation or an epimutation occurs in the DNA of a cell and it acquires abnormal functions. In a normal cell, when the DNA is damaged the cell either repairs the harm or the cell dies. In abnormal cells, the DNA is not repaired and the cell doesn't die as it should but it survives and continues to

proliferate, generating new cells that have the same damaged DNA. This leads to a mass of abnormal cells that grows out of control: the tumor (figure 1.1).

A tumor can be *benign*, not cancerous, which grows slowly and typically has clear borders that do not spread into other tissues, or *malignant*, i.e. the cancer, which grows rapidly, invades the surrounding tissue and metastasizes.

The formation of a cancer is a multistage process in which abnormal cells change the micro-environment to favor their survival. As a matter of fact, at the beginning, the cancer is just a microscopic nodule which does not have access to the vascular network and receives nutrients and growth factors via diffusion through the host (healthy) tissue. For example, the typical distance an oxygen molecule will diffuse before being uptake is approximately $100\mu\text{m}$ [13, 17, 57]. As time proceeds, tumor cells accumulate and the insufficiency of the existing vasculature to supply all cancerous cells may cause acute and chronic lack of oxygen (leading to hypoxia) and nutrient (e.g. glucose, leading to hypoglycemia). An avascular tumor cannot grow beyond a certain size, generally $1\text{-}2\text{ mm}^3$ [46]. Thus, a tumor only grows further if the cancerous cells acquire through mutations the ability to release pro-angiogenic growth factors (TAFs) in order to drive angiogenesis.

The *angiogenesis* is the formation of new capillaries throughout the tumor mass which is induced by growth factors (e.g. VEGF) secreted by tumoral cells [80]. In this way the tumor has a direct supply of nutrients and growth promoting factors. Once a tumor is vascularized, it can grow larger and even shed cells into vessels, leading to satellite tumors in distant parts of the body (metastases) (figure 1.2). The formation of metastasis is the predominant cause of mortality due to cancer [40].

How cancer starts

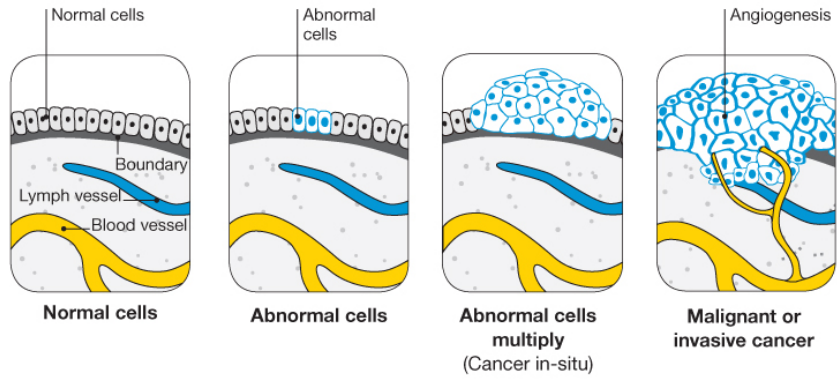


Figure 1.1: Physiologically cells grow and multiply in an orderly way. If a mutation in the DNA of a cell occurs, this mechanism breaks down and cells grow out of control. A mutation in the DNA could be caused from exposure to exogenous agents such as UV light, X-rays, chemicals, tobacco products, and viruses or for endogenous factors (naturally occurring), figure from [50].

How cancer spreads

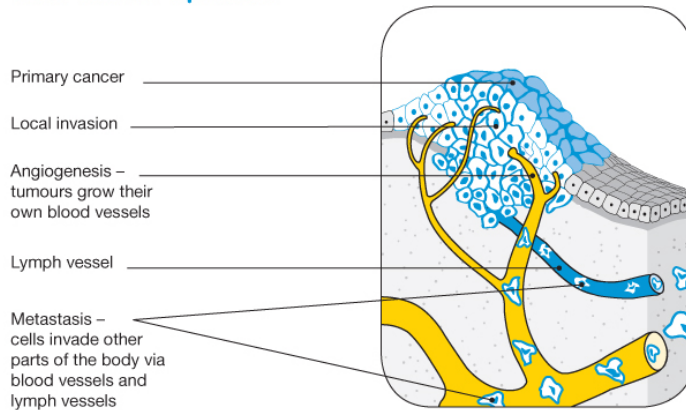


Figure 1.2: Once a tumor is vascularized, cancerous cells manage to move throughout the body using the blood or lymph systems, destroying healthy tissue in a process called invasion and it leads to metastasis, figure from [50].

1.2 Introduction to brain tumors

1.2.1 An overview of brain tumors

There are over than 120 types of brain tumors and spinal cord tumors: they can appear in the brain itself or in lymphatic tissue, in cranial nerves, in the meninges or in the pituitary or in the pineal gland. Brain tumors are named after the type of cells they arise from or the area they grow in. For instance, gliomas, the majority of malignant brain tumors in adult, take the name from the neoplastic glial cells as well as meningiomas take their name from the meninges, thin layers that envelope the central nervous system (CNS) [79]. Tumors can be divided in *primary* tumors, i.e. tumors that start in cells of the brain and may spread to other parts of the brain or to the spine, but rarely to other organs, or *metastatic* or secondary brain tumors, that begin in another part of the body and then spread to the brain [66]. In table 1.1 we classificate and describe the principal primary CNS tumors on the basis of the type of cell or tissue they arise from [79].

Concerning the epidemiology of the disease, in Europe, the standardized incidence of primary CNS cancers ranges from 4.5 to 11.2 cases per 100,000 men and from 1.6 to 8.5 per 100,000 women, while the 5-year survival rate is 17% for males and 19% for females. The statistic estimations have been obtained by Crocetti et al. [14] studying patients affected by CNS cancers in the period between 1995 and 2002.

1.2.2 Classification of gliomas

Gliomas make up 80% of all malignant brain tumors [21] and, despite their frequency, the etiology of these tumors remains largely unknown. The common gliomas affecting the cerebral hemispheres of adults are named "diffuse" gliomas due to their propensity to infiltrate extensively throughout the brain parenchymia. These gliomas are classified histologically as astrocytomas, oligodendrogliomas,

Tumor Type	Cell / Tissue Origin	Cell / Tissue Description	Tumor Description
Gliomas	Neuroglia	It is the supportive (gluey) tissue of the brain (figure 1.3). It maintains the ionic milieu of nerve cells, it modulates the rate of nerve signal propagation and the synaptic action by controlling the uptake of neurotransmitters, and prevents from neural injury [61].	see subsection (1.2.2)
Medulloblastoma	Neuroectodermal cells	They are very early forms of nervous system that are probably involved in brain cell development.	It develops in the cerebellum and it is highly malignant. It affects children.
Meningioma	Meninges	They are layers of tissue that line and protect the brain.	It accounts for 1 out of 3 primary brain tumors and they are usually benign. Many meningiomas are asymptomatic.
Pituitary tumors	Pituitary gland and hypothalamus	They both make hormones that help regulate the activity of many other glands in the body, such as thyroid gland.	They account for the 8% of tumor and they are nearly benign. Symptoms are related with an excess or a lack of hormones produced by the glands.
Pineal tumors	Pineal gland	It is a small endocrine gland situated deep within the brain, between the cerebral hemispheres. It makes melatonin, the hormone that regulates sleep.	They accounts for only 1 to 2% of brain tumors.
Schwannomas	Schwann cells	These cells surround and insulate cranial nerves and other nerves.	They make up about the 8% of CNS tumors. They are almost always benign and can arise in any nerves. In relation to the function of the nerve they start from, Schwannomas can cause different symptoms, such as acoustic or balance problems.

Table 1.1: Classification and description of the principal primary Central Nervous System tumors on the basis of the type of cell or tissue they arise from [79].

ependymomas, or tumors with morphological features of both astrocytes and oligodendrocytes, termed oligoastrocytomas. Astrocytomas arise from astrocytes, star-like cells (figure 1.3) that help support and nourish neurons and maintain an appropriate chemical environment for neuronal signaling. Oligodendrogliomas are tumors formed by oligodendrocytes, the cells that make myelin, a fatty substance that surrounds and isolates the nerve cell axons and which helps neurons to send electric signals. Ependymomas come from ependymocytes, the glial cells that make up the ependyma, the membrane that lines the ventricles of the brain and the central canal of the spinal cord. Gliomas are further categorized on the basis of the pathologic evaluation and the histological degrees of malignancy of the tumor. The most widely used current classification of human gliomas is the one proposed by the World Health Organization in 2007 [39] which we schematize in table 1.2. In table 1.3 we report population-based incidence rates (per 100000 person per year), age, sex and survival of patients which have been affected by gliomas in 1992-1997 in US [52].

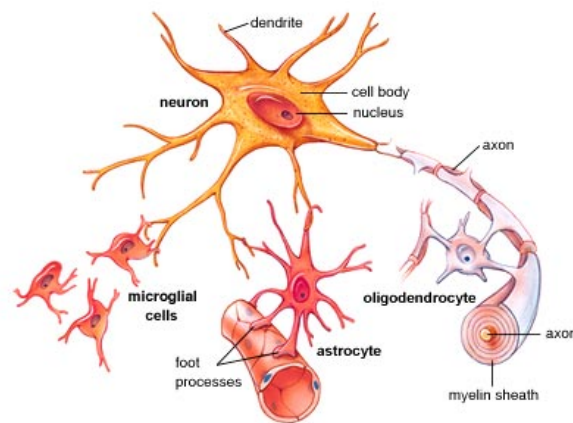


Figure 1.3: Neuroglia performs a supportive function for neurons. It is composed by microglial, that is the main form of active immune defense in the central nervous system and accounts for the 10-15% of the glial cells, and macroglial, derived from the ectodermal tissue, that is mainly composed by astrocytes (cells with a star-like appearance), oligodendrocytes, ependymocytes and Schwann cells. Figure taken from [61].

WHO grading system		
Grade	Description	Type of glioma
I	Benign and slow growing Cells look almost normal under a microscope Usually associated with long-term survival Rare in adults	Pilocytic astrocytoma
II	Relatively slow growing Sometimes spreads to nearby normal tissue and comes back (recurs) Cells look slightly abnormal under a microscope Sometimes comes back as a higher grade tumor	Diffuse astrocytoma Oligodendroglioma Oligoastrocytoma
III	Malignant = cancerous Actively reproduces abnormal cells Tumor spreads into nearby normal parts of the brain Cells look abnormal under a microscope Tends to come back, often as a higher grade tumor	Anaplastic Astrocytoma Anaplastic Oligodendroglioma Anaplastic Oligoastrocytoma Anaplastic Ependymoma
IV	Most malignant, fast growing Easily spreads into nearby normal parts of the brain Actively reproduces abnormal cells Cells look very abnormal under a microscope Tumor forms new blood vessels to maintain rapid growth Tumors have areas of dead cells in their center (called necrosis)	Glioblastoma - Gliosarcoma - Giant Cell Glioblastoma

Table 1.2: WHO grading system applied to gliomas: grade I is assigned to the more circumscribed tumors with low proliferative potential, grade II defines diffusely infiltrative tumours, grade III is assigned to those showing anaplasia and mitotic activity and grade IV (glioblastoma) describes tumours that show microvascular proliferation and/or necrosis [39, 21].

1.3 Glioblastoma Multiforme

In the present work, we focus on glioblastoma (GBM) tumor, an astrocytoma grade IV, the most common and aggressive among gliomas, that accounts for 15% of all primary central nervous system tumors and 55% of all gliomas [21].

On the basis of clinical presentation, glioblastomas have been further subdivided into the primary or secondary GBM subtypes. The vast majority of glioblastomas are primary glioblastomas (90% of GBMs) which develop rapidly de novo in el-

Tumor	WHO grade	Incidence Rate	M:F ratio	Mean age at diagnosis	Survival			
					1 year	2 years	5 years	10 years
Pilocytic astrocytoma	I	0.23	1.09	17	95%	93%	89%	86%
Diffuse Astrocytoma	II	0.13	1.46	47	73%	60%	45%	34%
Oligodendroglioma	II	0.34	–	42	88%	80%	66%	47%
Ependymoma/ Anaplastic Ependymoma	II/ III	0.23	1.29	35	86%	79%	66%	55%
Anaplastic Astrocytoma	III	0.49	1.20	50	60%	43%	28%	19%
Anaplastic Oligodendrocytes	III	0.10	1.15	46	75%	57%	38%	25%
Glioblastoma	IV	2.96	1.26	62	28%	8.2%	2.9%	1.8%

Table 1.3: Population-based data of incidence rates (per 100,000 person per year), age and sex, and survival of patients with gliomas in 1992-1997 in United States adjusted to the 2000 US (see [52])

derly patients, without clinical or histologic evidence of a less malignant precursor lesion. In contrast, secondary glioblastomas progress from low-grade diffuse astrocytomas or anaplastic astrocytomas. They manifest in younger patients, have a lesser degree of necrosis, are preferentially located in the frontal lobe, and carry a significantly better prognosis. Histologically, primary and secondary glioblastomas are largely indistinguishable, but they differ in their genetic and epigenetic profiles [53, 55].

Glioblastoma was observed for the first time in 1863-1865 by Virchow, known as the father of pathology, who was the first to identify a large group of intracranial tumors whose origin was in the glial tissue of the brain. He gave the name *glioma* to these new growths and he described such neoplasm as slow-growing, infiltrating vascular masses with hemorrhages, cysts and degenerated areas. In 1925 Globus and Strauss [15] proposed the name *spongioblastoma multiforme* since, to the naked eye, glioblastoma appears as a well circumscribed mass, globular or spherical, with a highly variegated cut surface due to necrosis, fatty degeneration and hemorrhages and it is characterized by a necrotic core surrounded by anaplas-

tic cells [27]. In 1926 the term *glioblastoma multiforme* was introduced as an alternative form of spongioblastoma by Percival Bailey and Harvey Cushing [2], two American surgeons who created the first major system of classification for brain tumors. They claimed that glioblastoma originates from primitive precursors of glial cells called glioblasts. In 1979 the first edition of the World Health Organization (WHO) Classification of Tumors of the Nervous System was published and glioblastomas were not yet recognized as astrocytic neoplasms but listed in a group of "poorly differentiated and embryonal tumors" [55]. Only after the introduction of immunohistochemistry it has been discovered that glioblastoma is actually an extreme manifestation of anaplasia and dedifferentiation of astrocytes.

For unknown reasons, glioblastoma occurs commonly in Caucasians, Asians males over 50 years old, without any genetic predisposition [54]. The prevalent symptom is a progressive memory, personality, or neurological deficit [66], in addition to common symptoms such as seizure, nausea, vomiting and headache. Glioblastoma has median survival of about 14.6 months while for 30% of the cases survival could reach two years, [33]. However, there are reports that some patients can live for more than 10 years after diagnosis. A common feature among those patients is that they are typically younger than 40 years at the time of diagnosis [9, 65].

1.3.1 Hallmark features

Glioblastoma is defined by the hallmark features of uncontrolled cellular proliferation, diffuse infiltration, propensity for necrosis, robust angiogenesis, intense resistance for apoptosis and rampant genomic instability [19]. As reflected by the old epithet *multiforme*, GBM presents with significant heterogeneity on the cytopathological, transcriptional and genomic levels. The tumor may take on a variety of appearances, depending on the amount of hemorrhage, necrosis, or its age.

These tumors may be firm or gelatinous. Considerable regional variation in appearance is characteristic. Secondary to necrosis, some areas are firm and white, some are soft and yellow, and still other are cystic with local hemorrhage. Moreover, glioblastomas have a large variability in size and infiltration beyond the visible tumor margin is always present [62].

Glioblastoma forms in the cerebral white matter and grows quickly along the fibers or along vessels and it seems that it follows the physical structures in the extracellular matrix of the neighboring brain [23]. The tumor may arise in any part of the Central Neural System but the frontal and the temporal lobes are the most frequently affected. The central part of the brain is often involved, and a classical appearance is provided by the butterfly type, in which the tumor extends in both hemispheres [27] as depicted in figures 1.4. Malignant cells carried in the cerebrospinal fluid may invade and migrate away from the main tumor within the brain; however, glioblastomas rarely spread elsewhere in the body.

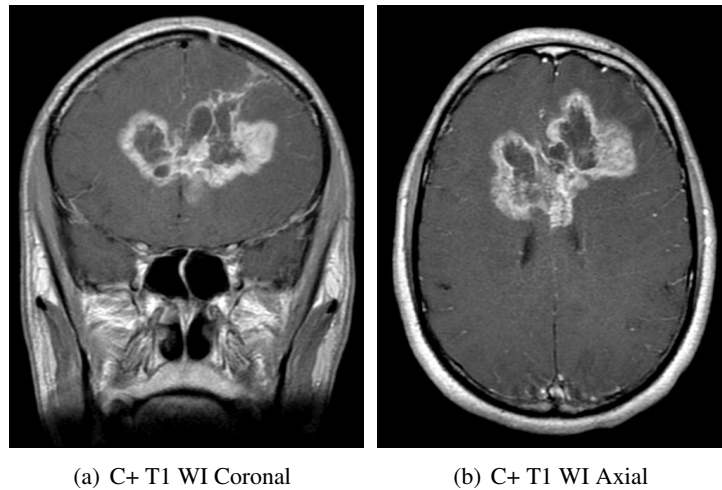


Figure 1.4: C+ (contrast-enhanced) T1 MRI WI (weighted) of a butterfly glioblastoma. If the tumor arises in the central part of the brain, it spreads in both hemispheres and thus it shows a butterfly appearance.

1.3.2 Diagnosis and treatment

Brain tumors are very difficult to be treated due to the following factors: tumor cells are very resistant to conventional therapies, many drugs cannot cross the blood brain barrier to act on the tumor and brain has a very limited capacity to repair itself [34]. Moreover, concerning glioblastoma, its treatment remains even more difficult. As a matter of fact, this tumor is heterogeneous, it is often located in a region that is beyond the reach of local control and its highly diffusive nature makes the complete removal almost impossible. Therefore, the treatment of patients with malignant gliomas is made on different levels and encompasses surgery, radiotherapy, and chemotherapy.

For the diagnosis, conventional imaging techniques, such as computed tomography (CT or CAT scan) and magnetic resonance imaging (MRI), are commonly used to pinpoint the tumor. Depending on the patient, other exams could be requested; e.g. magnetic resonance spectroscopy (MRS) is used to examine the tumor's chemical profile and determine the nature of the lesions seen on the MRI. Upon an initial diagnosis, the first step in treating the glioblastoma is to remove as much of tumor as possible, without injuring brain tissue (figure 1.5). In the last years, the diffusion tensor imaging technique, which will be described in more details in Chapter 2, has gained in importance since it provides parametric maps that help to visualize different aspects of the tissue micro-structure which may help the neurosurgeons to avoid disrupting important nerve connections within the brain itself. However, high-grade tumors are surrounded by a zone of migrating, infiltrating tumor cells that invade surrounding tissues and thus removing the entire tumor could be very difficult and, almost always, impossible. Anyway, gross tumor resection immediately decompresses the brain reducing the intracranial pressure and, due to the consequent reduction in neoplastic cells in the surgical cavity, probably increases the likelihood of response to radiotherapy and/or chemotherapy; it may, moreover, delay progression. Always after surgery, when the wound is healed,

radiation therapy can begin. The goal of radiation therapy is to kill tumor cells selectively while leaving normal brain tissue unharmed. In standard external beam radiation therapy, multiple sessions of standard-dose "fractions" of radiation are delivered to the tumor site as well as a margin in order to treat the zone of infiltrating tumor cells. Each treatment induces damage to both healthy and normal tissue but by the time the next treatment is given, most of the normal cells have repaired the damage, but the tumor tissue has not. In addition, the patient is treated concomitant with chemotherapy, by which special drugs designed to kill tumor cells are administered. Nowadays, the standard drug used is the temozolomide, which has shown to give survival benefits with minimal additional toxicity. The current standard of care, that is the Stupp protocol, has led to a significant improvement in patient survival. This protocol consists of adjuvant radiotherapy after resection plus continuous daily temozolomide (75 mg per square meter of body-surface area per day, 7 days per week from the first to the last day of radiotherapy), followed by six cycles of adjuvant temozolomide (150200 mg per square meter for 5 days during each 28-day cycle) [68]. Because traditional methods of treatment are unlikely to result in a prolonged remission of GBM tumors, researchers presently are investigating several innovative treatments in clinical trials [49, 74].

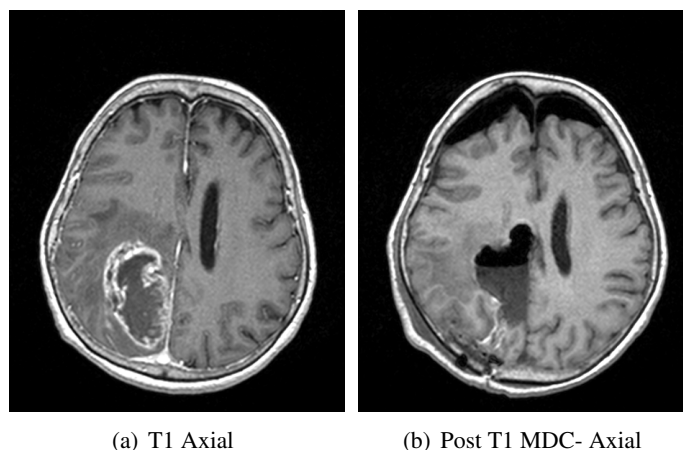


Figure 1.5: Example of glioblastoma resection. The figures have been gently provided by the *Istituto Neurologico Carlo Besta*.

Chapter 2

Diffusion Tensor Imaging

Diffusion imaging is a magnetic resonance imaging method introduced in the mid-1980s [37]. It focuses on the random translational motion of molecules, mainly water, which, during the typical diffusion time of about 50 msec [37, 47], move in the brain over a distance of $10\mu m$ [37, 47], bouncing, crossing, or interacting with many tissue components such as cell membrane, fibers and macromolecules. Since these movements encounter different obstacles and vary in according to the tissue or certain pathological modifications (such as intracellular edema, abscess, tumor), diffusion data provides indirect information on the structure surrounding these water molecules and on the geometric organization of the brain. Indeed, the overall effect observed in a diffusion MRI image voxel reflects, on a statistical basis, the displacement distribution of the water molecules present within this voxel and it allows to probe tissue structure at a microscopic scale, well beyond the usual image resolution. A useful analogy is the shape of ink dropped on a piece of paper. After the ink is dropped, it begins to spread due to the thermal motion of its molecules and the shape of the ink stain can reveal something about the underlying structure of the paper. If the shape of the ink stain is circular, it is called *isotropic diffusion*. If the stain is elongated along a precise direction, it is called *anisotropic diffusion*. Diffusion-weighted (DW) magnetic resonance (MR) imaging is currently the only MR imaging technique that provides in vivo information on water diffusion within

tissues, involving the use of phase-defocusing and phase-refocusing gradients. We briefly describe this technique in the first section of the present chapter.

A further development of DWI is the diffusion tensor imaging (DTI) technique, which was introduced in the mid-1990s [37]. It studies the directions of water molecule motion to characterize diffusion behavior in biological tissues and it makes use of the concept of anisotropy to estimate the axonal organization of the brain. Namely, water moves more easily along the axonal bundles rather than perpendicular to those bundles for the fact that there are fewer obstacles in that direction. Thus, studying the directions of diffusion of water molecules, it is possible to gain access to the microscopic organization of the tissue in which the diffusion takes place. The information of the anisotropic structure of the tissue are summarized in a tensor of diffusivity, which gives the name to this technique. We describe DTI method in section 2.

2.1 Diffusion Weighted Measurements

In order to better understand the diffusion tensor imaging technique, it is useful to briefly illustrate how diffusion-weighted imaging (DWI) works. In particular, in the following we explain how the MR signal is recorded and the relationship between the diffusion of water molecules in tissues and the intensity of the signal measured by MR imaging. As mentioned, diffusion weighted imaging (DWI) focuses on measuring the random Brownian motion of water molecules within a voxel of tissue and it is based on diffusion weighted sequences by which medical images are obtained. These images present a contrast which is namely influenced by the difference of motion of water molecules.

The information that can be acquired from a DW MRI image are: S , the MR signal recorded into a voxel, PD , the proton density which represents the water concentration, T_1 and T_2 , the relaxation times (decay times) after excitation which are related to environment factors, and D , the diffusion coefficient. These parameters

are related by the equation

$$S = PD \left(1 - e^{-TR/T_1}\right) e^{-TE/T_2} e^{-bD} \quad (2.1)$$

where TR and TE are respectively related to the timing of excitation (called repetition time) and the preparation period (called echo time) of the MR signal whereas b is the diffusion weighted factor. In this equation it is important to note that the magnitude of signal from water S is the information we obtain from the MR scanners while TR , TE and b are imaging parameters that we can control and, changing these parameters, we can change the contribution (*weighting*) of T_1 , T_2 and D to the signal [47].

To understand the b term, we first have to introduce the concept of magnetic field gradient pulse. In figure 2.1, the effect of a gradient pulse is explained with a schematic diagram.

We consider the signals generated by two different water molecules (red and blue circles) in two different position along the Y axis (for instance). In time period I, both molecules see the homogeneous magnetic field applied and thus the spins have the same frequency. Then, in time period II, the Y gradient is applied and the spin in blue position is exposed to a lower magnetic field than the one in the red position and so it resonates at a lower frequency. After the gradient pulse ends (time period III), the signals from the water molecules begin to have the same frequency but their phases are shifted according to

$$\Delta\varphi = \varphi_1 - \varphi_2 = \gamma G \delta (y_1 - y_2) \quad (2.2)$$

where γ is the gyromagnetic ratio of proton, G is the constant gradient strength, δ is the duration of the gradient pulse application and y_i the position of the spin with respect to the gradient. In time period IV, an other Y gradient is applied with the opposite polarity and, interestingly, the phase shift is unwound. In fact, in this period, water molecules in the blue position start to resonate at higher frequency

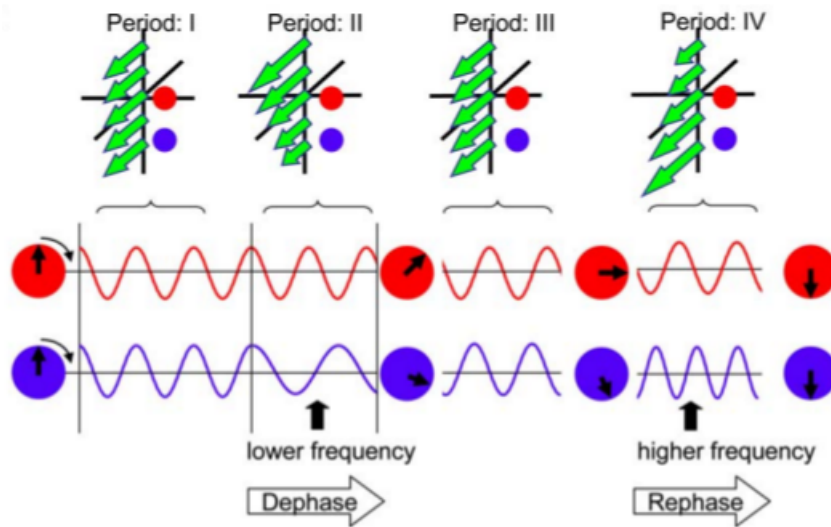


Figure 2.1: Magnetic field gradient and their effects on the MRI signal [47]. Y gradients are applied at time periods II and IV. The durations of the period II and IV are the same, but the orientations of the gradient are opposite. Water signals from two different locations are shown by red and blue colors. The signal frequency is proportional to the strength of the magnetic field B_0 , represented by the green arrows. The figure is taken in [47].

and then the perfect refocusing of the phase occurs.

However, the perfect refocusing of the phase occurs only if the particles do not change their initial position. For this reason, in the diffusion measurement, the phase difference $\Delta\varphi$ is used to compute water motion in the direction of the gradient of the magnetic field.

In order to better explain the concept, we consider the figure 2.2, in which water molecules and the relative spin phase, sketched as circles with black arrows, are illustrated within a voxel. When the first gradient is applied, a phase shift depending on the position of the spin is introduced between the molecules and the spins are dephased. After a time interval Δt , a second gradient pulse for the phase refocusing is applied. The refocusing is perfect only when the water molecules do not move between the two pulses. If there is translational motion of water molecules, perfect refocusing would fail. Because the signal at each voxel represents the sum

of the signal from all the water molecules in that sample, the imperfect refocusing leads to a signal loss. It is important to notice that, as show by equation (2.1), the higher the diffusion coefficient D is, the more signal loss we expect. The term b is related to the intensity of the gradient application G and to the time separation between the two gradient pulses Δt [44] :

$$b = \gamma^2 G^2 \delta^2 \left(\Delta t - \frac{\delta}{3} \right). \quad (2.3)$$

The important point is that we can control the amount of the b values as all the quantities in (2.3) can be set, and we can expect a different amount of signal loss. In fact, the longer the separation Δt is and the more time there is for water molecules to move around which is reflected in a higher signal loss.

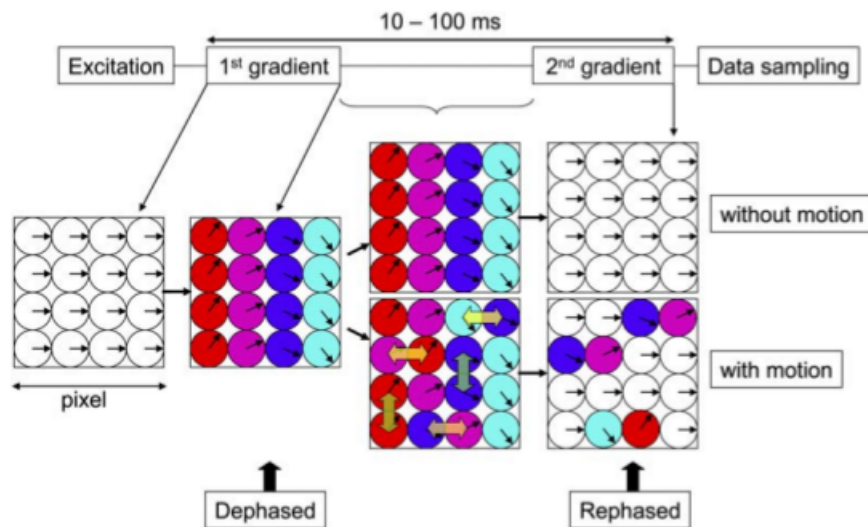


Figure 2.2: The effect of gradients application on the motion of water molecules. If there is molecular diffusion, a total phase shift is introduced. In absence of water motion, gradients have no consequence. The figure belongs to [47].

Consequently, in order to compute the diffusion coefficient of water molecules it is sufficient to perform two measurements with different b values, while other imaging parameters (TE and TR) remain the same. In particular, one of the two measurements must be done with a null b value. So, the signal loss due to the diffusion process is governed by the Stejskal-Tanner equation [67]:

$$S = S_0 e^{-bD} \quad (2.4)$$

where S_0 is the signal intensity without diffusion sensitization, that is obtained from (2.1) setting $b = 0$. In this way, the diffusion coefficient, D , can be calculated from the signal intensity differences between these two studies:

$$D = -\frac{1}{b} \ln \left(\frac{S}{S_0} \right). \quad (2.5)$$

Since biological tissues can be considered anisotropic mediums because of the architecture of the tissue itself or the presence of obstacles, the D diffusion parameter is substitute with an *apparent diffusion coefficient ADC* [36]:

$$S = S_0 e^{-bADC}. \quad (2.6)$$

The reason for which the adjective *apparent* is used is related to the fact that what is measured is not the *real* diffusion coefficient. For instance, the *ADC* of water in parenchymia is much smaller than that of the cerebrospinal fluid. This could be due to the more viscous environment but also due to many obstacles. Namely, when the barriers are aligned along one orientation, the *ADC* depends on the measurement orientation, e.g. measurements along the structures lead to higher *ADC* (less obstacles) and viceversa measurements perpendicular to them lead to smaller *ADC* (more barriers).

In other words, to sum up the present section, in order to estimate the apparent diffusion coefficient along a specific direction it is necessary to apply a magnetic field

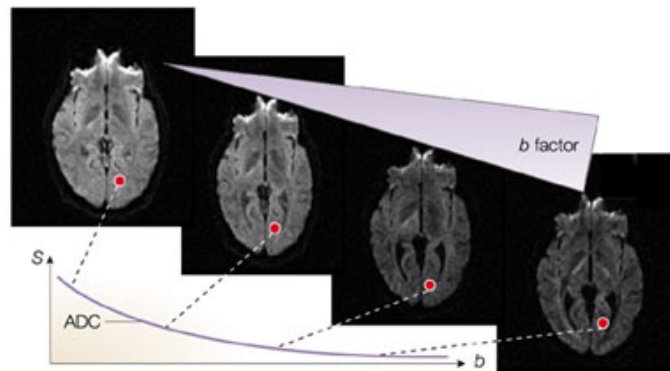


Figure 2.3: In practice, different degrees of diffusion-weighted images can be obtained using different values for the b factor. The larger the b factor, the more the signal intensity (S) becomes attenuated in the image. This attenuation is modulated by the diffusion coefficient. In fact, the signal in structures with fast diffusion (for example, water-filled ventricular cavities) decays rapidly with increasing b , whereas the signal in tissues with low diffusion (for example, grey and white matter) decreases more slowly. By fitting the signal decay as a function of b , one obtains the apparent diffusion coefficient (ADC) for each elementary volume (voxel) of the image, [35]. Nowadays, it is used a b value in the range of $700\text{-}1000\text{ s/mm}^2$, [78]

along that direction and perform two measurements, one of which with a null b : thus, a measure along the X , Y , and Z axis will lead to the computation of ADC_x , ADC_y and ADC_z . In the next section, the diffusion tensor imaging, a technique that summarizes and the information from the $ADCs$ is introduced.

2.2 Diffusion Tensor Imaging Technique

In tissues, such as brain gray matter, where the measured apparent diffusivity is largely independent of the orientation of the tissue (i.e. isotropic), it is usually sufficient to characterize the diffusion properties of the tissue with the ADC . However, in anisotropic media, such as in white matter, where the measured diffusivity is known to depend upon the orientation of the tissue, a single ADC cannot characterize the orientation-dependent water mobility. In this case, a mathematical object, describing molecular mobility along each direction and correlations

between these directions, is required. This object is a second order tensor called *diffusion tensor* [3] and it consists of 9 components that are included in a 3×3 symmetric matrix (i.e. $D_{ij} = D_{ji}$, with $i, j = x, y, z$). The diffusion tensor D has the following form:

$$D = \begin{pmatrix} D_{xx} & D_{xy} & D_{xz} \\ D_{xy} & D_{yy} & D_{yz} \\ D_{xz} & D_{zy} & D_{zz} \end{pmatrix}$$

where D_{xx}, D_{yy}, D_{zz} represent the magnitude of diffusivity along the x, y, z directions and D_{xy}, D_{xz}, D_{yz} represent the magnitude of diffusion along one direction arising from a concentration gradient in an orthogonal direction (see figure 2.4).

According to (2.4), the signal attenuation of the MR signal is

$$S = S_0 e^{-\mathbf{bD}} = S_0 e^{-\sum_{ij} b_{ij} D_{ij}} \quad (2.7)$$

$$= S_0 e^{-(b_{xx} D_{xx} + b_{yy} D_{yy} + b_{zz} D_{zz} + 2b_{xy} D_{xy} + 2b_{xz} D_{xz} + 2b_{yz} D_{yz})} \quad (2.8)$$

with

$$b_{ij} = \gamma^2 G_i G_j \delta^2 \left(\Delta t - \frac{\delta}{3} \right). \quad (2.9)$$

In this formalism, the diffusion-weighting factor b incorporates the direction and magnitude of the applied diffusion gradient vector (G_x, G_y, G_z).

In order to describe the diffusion, the components of the tensor have to be evaluated. Since the tensor is symmetric, only six components are independent and consequently seven diffusion measurements are required at least for each voxel of the image: one measurement is necessary to evaluate S_0 , while six measurements are made along six non collinear directions.

We remark that the values of the components depend on the orientation of the sample respect to the laboratory reference system, defined by the directions of the spatial encoding gradients. Hence, the tensor cannot be uniquely described.

However, it exists a reference frame $[x', y', z']$ that coincides with the principal directions of diffusivity and thus it is determined by the local anatomy. In the

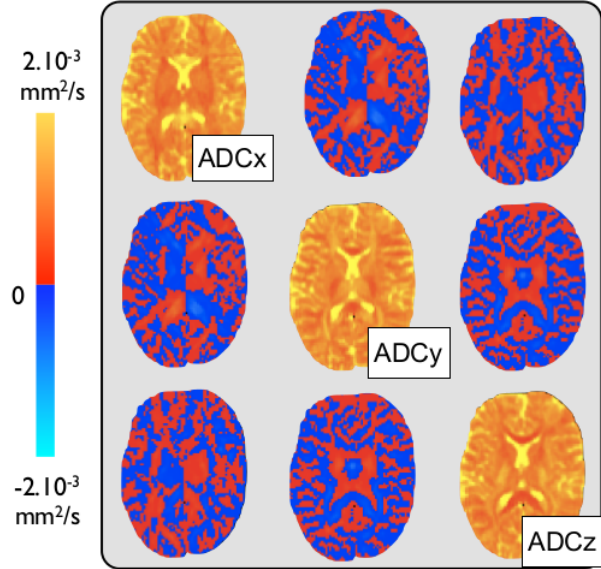


Figure 2.4: Components of the diffusion tensor \mathbf{D} . Diagonal elements D_{xx} , D_{yy} , D_{zz} are proportional to the diffusion displacement coefficients (ADCs) along the three directions of the experiment coordinate system. Off-diagonal elements are proportional to the correlations (covariances) of displacements along these directions (figure from [24]).

reference frame, the off diagonal terms are null (i.e. the orthogonal directions appear non correlated) and the tensor is reduced to a diagonal matrix (figure 2.5). This is called *main axes reference system* and it can be mathematically obtained by the diagonalization of the diffusion tensor. Hence, the problem consists in finding the eigenvalues and the eigenvectors of the matrix \mathbf{D} :

$$\mathbf{D}\mathbf{e}_i = \lambda_i\mathbf{e}_i \quad \text{for } i = 1, 2, 3 \quad (2.10)$$

which in matrix form is

$$\mathbf{D}\mathbf{E} = \mathbf{\Lambda}\mathbf{E} \quad (2.11)$$

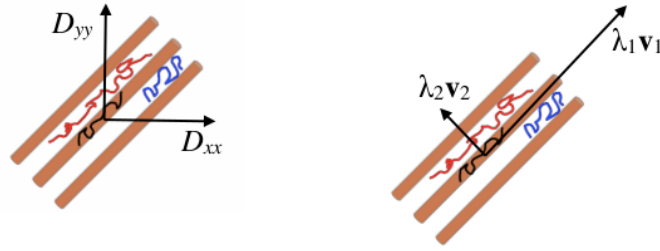


Figure 2.5: Diffusion components in relation to fibers orientation. Figure (a): D_{xx} and D_{yy} are determined by measurements along the x - and y - directions. Figure (b): the values are computed in the reference system which coincides with the direction of the fibers. The figure is taken from [24].

with

$$\mathbf{E} = (\mathbf{e}_1 | \mathbf{e}_2 | \mathbf{e}_3) \quad \text{and} \quad \mathbf{\Lambda} = \begin{pmatrix} \lambda_1 & 0 & 0 \\ 0 & \lambda_2 & 0 \\ 0 & 0 & \lambda_3 \end{pmatrix} \quad (2.12)$$

where $\mathbf{\Lambda}$ is the matrix of the eigenvalues and \mathbf{E} is the orthogonal matrix of the eigenvectors.

The most intuitive way to conceptualize the information provided by the diffusion tensor is to view it geometrically by the *diffusion ellipsoid* [3]. An ellipsoid is a 3D representation of the diffusion distance covered in space by molecules in the diffusion time interval Δ . This ellipsoid, which can be displayed for each voxel of the image, is easily calculated from the eigen-diffusivities. Its equation is

$$\left(\frac{\mathbf{e}_1}{\sqrt{2\lambda_1\Delta}} \right)^2 + \left(\frac{\mathbf{e}_2}{\sqrt{2\lambda_2\Delta}} \right)^2 + \left(\frac{\mathbf{e}_3}{\sqrt{2\lambda_3\Delta}} \right)^2 = 1. \quad (2.13)$$

In particular, the three eigenvectors \mathbf{e}_1 , \mathbf{e}_2 , \mathbf{e}_3 and the three eigenvalues λ_1 , λ_2 , λ_3 describe respectively the directions and lengths of the ellipsoid's axes in descending order of magnitude (see figure 2.7, first row). The largest eigenvector, termed the "primary eigenvector" and its associated eigenvalue λ_1 indicate, respectively, the direction and magnitude of the greatest water diffusion. The primary eigenvec-

tor is important for fiber tractography algorithms because this vector indicates the orientation of axonal fiber bundles. Therefore, λ_1 is also termed longitudinal diffusivity, because it specifies the rate of diffusion along the orientation of the fibers. The second and third eigenvectors are orthogonal to the primary eigenvector, and their associated eigenvalues λ_2 and λ_3 give the magnitude of diffusion in the plane transverse to axonal bundles. Hence, they are also known as radial diffusivities. The figure 2.6 shows a schematic depiction of diffusion properties through the diffusion ellipsoid scheme.

Finally, it is possible to analyze the diffusion tensor data by a number of rotationally invariant diffusion parameters, derived from the 3 eigenvalues, in order to provide information on tissue microstructure and architecture for each voxel. The *mean diffusivity* D_{av} , which characterizes the overall mean-squared displacement of molecules and the overall presence of obstacles to diffusion within a voxel (average ellipsoid size), is evaluated as follows:

$$D_{av} = \frac{Tr(\mathbf{D})}{3} = \frac{D_{xx} + D_{yy} + D_{zz}}{3}. \quad (2.14)$$

Among the various scalar indexes proposed to characterize diffusion anisotropy, the most widely used is the *fractional anisotropy* (FA) which describes how much molecular displacement vary in space (ellipsoid eccentricity) and it is related to the presence of oriented structures. Its formula is:

$$FA = \sqrt{\frac{1}{2} \frac{\sqrt{((\lambda_1 - \lambda_2)^2 + (\lambda_2 - \lambda_3)^2 + (\lambda_3 - \lambda_1)^2)}}{\sqrt{\lambda_1^2 + \lambda_2^2 + \lambda_3^2}}}. \quad (2.15)$$

This is a very convenient index because it is scaled from 0, isotropic medium, to 1, anisotropic medium, indicating perfectly linear diffusion occurring only along the primary eigenvector. The fiber orientation information inherent in the primary eigenvector can be visualized on 2D images by assigning a color to each of 3 mutually orthogonal axes (see figure 2.7, bottom right).

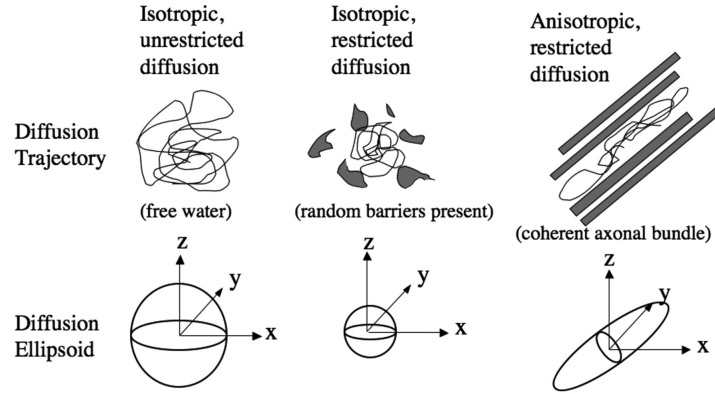


Figure 2.6: Scheme of diffusion properties via ellipsoid visualization for isotropic unrestricted diffusion, isotropic restricted diffusion, and anisotropic restricted diffusion [48].

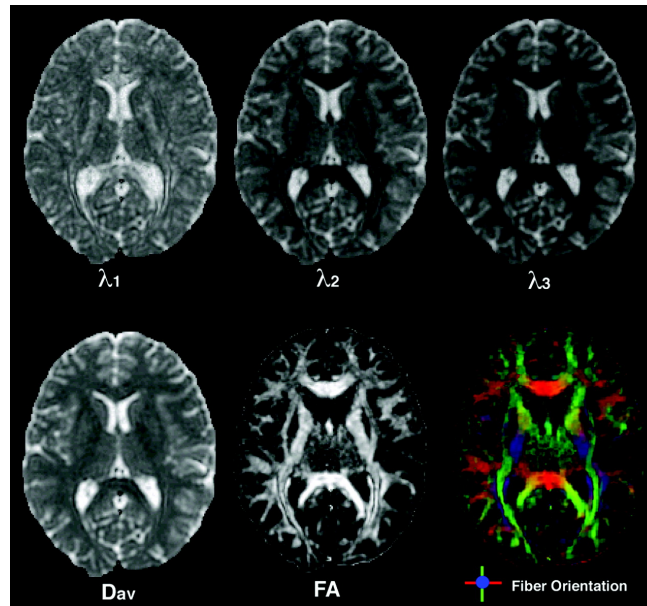


Figure 2.7: Depiction of the eigenvalues, mean diffusivity, FA and a color map of the fiber orientation. In the first row, λ_1 , λ_2 , λ_3 are shown with the same intensity scaling. The eigenvalues are always ordered in descending order of intensity with the first eigenvalue being the greatest. In the second row, the mean diffusivity, the fractional anisotropy and a color map of the orientation of the primary eigenvector are shown. The figure is taken from [48].

Chapter 3

Mathematical Model

In this chapter, we provide the derivation of a mathematical model suitable to describe a tumoral mass growth. The theoretical framework of our approach comes from the continuum theory of mixture, which is briefly introduced in section 3.1. The theory of mixture, which has its roots in the continuum mechanics, is based on balance equations and conservation principles and it has been widely applied to systems which can be studied as a mixture of interacting continua. In the second section, we present a two-species diffuse interface model of tumor growth. It is a general model formulated for a tumor comprising viable tumor cells and water, i.e. interstitial fluid which may contain dead cells and other substances. A single vital nutrient (e.g. oxygen) is taken into account in the model and it is assumed that the density of the extra-cellular matrix (ECM) remains constant in time and space and does not significantly degrade or remodel as the tumor mass grows. In the last part of the chapter, we specifically deal with glioblastoma and we estimate the biological parameter introduced in our mathematical model.

3.1 A continuum theory of mixtures

The starting point of our research is the theory of mixture. The literature on this subject is very rich, dating back to the early work on simple mixtures of Fick

and Darcy during the middle of the XIX century and progressing to the general continuum theories advanced by Truesdell, the pioneer of the modern continuum models of mixture fluids, in the last years of the 50s [51]. The purely mechanical model developed by Truesdell was essentially extended and corrected by Muller (1968), who gave rise to the modern thermodynamical theory of miscible mixtures [82]. Then, the important and comprehensive article of Bowen [6] and the monograph of Rajagopal and Tao [63] provided a wide review of the relevant literature on the subject.

Inspired by the article of Bowen [6], in the following we report some basic notations of the mixture theory and we provide a brief discussion on the mass balance equation under the incompressibility condition.

3.1.1 Kinematics

The fundamental idea underlying the mixture theory is that a material body or a mixture \mathcal{B} can be composed of N constituent species called phases $\mathcal{B}_1, \mathcal{B}_2, \dots, \mathcal{B}_N$ and in any instant of time, each point of the domain is occupied simultaneously by particles of all components. It is convenient to describe \mathcal{B} in the Eulerian reference and represent all fields of the model as functions of the spatial variable $\mathbf{x} \in \mathcal{B}$ and time $t \in \mathcal{T}$. We introduce a fixed reference configuration so that the spatial position occupied by a material point at time t is

$$\mathbf{x} = \chi_\alpha(\mathbf{X}_\alpha, t) \quad (3.1)$$

where χ_α is the deformation function of the α^{th} constituent and \mathbf{X}_α is the position of a particle of the α^{th} constituent in its reference configuration. Then, the velocity of a particle in \mathbf{X}_α at time t is defined by

$$\mathbf{v}_\alpha = \frac{\partial \chi_\alpha(\mathbf{X}_\alpha, t)}{\partial t}. \quad (3.2)$$

Thus, if Ψ is any function of (\mathbf{x}, t) , the material derivative of Ψ following the motion of the α^{th} constituent is

$$\dot{\Psi}_\alpha = \frac{\partial \Psi(\mathbf{x}, t)}{\partial t} + \nabla \Psi(\mathbf{x}, t) \mathbf{v}_\alpha. \quad (3.3)$$

Given V the total volume of \mathcal{B} containing a point (\mathbf{x}, t) and $m_\alpha(\mathbf{x}, t)$ the mass of a single constituent \mathcal{B}_α , we define the *apparent mass density* ρ_α of each constituent α^{th} as

$$\rho_\alpha(\mathbf{x}, t) = \frac{m_\alpha(\mathbf{x}, t)}{V(\mathbf{x}, t)} \quad (3.4)$$

and consequently the *apparent mass density of the mixture* at (\mathbf{x}, t) is

$$\rho(\mathbf{x}, t) = \sum_{\alpha=1}^N \rho_\alpha(\mathbf{x}, t). \quad (3.5)$$

Then, we introduce the *true mass density* γ_α of the α^{th} constituent by the relation

$$\gamma_\alpha(\mathbf{x}, t) = \frac{m_\alpha(\mathbf{x}, t)}{V_\alpha(\mathbf{x}, t)} \quad (3.6)$$

where $V_\alpha(\mathbf{x}, t)$ is the volume occupied by a single \mathcal{B}_α . It is then possible to define a new quantity ϕ_α , as follows:

$$\phi_\alpha(\mathbf{x}, t) = \frac{\rho_\alpha(\mathbf{x}, t)}{\gamma_\alpha(\mathbf{x}, t)} = \frac{V_\alpha(\mathbf{x}, t)}{V(\mathbf{x}, t)}. \quad (3.7)$$

This quantity is called *volume fraction* and it physically represents the volume of the α^{th} constituent per unit volume of the mixture. Consequently, we have the following relation for each α^{th} constituent:

$$\rho_\alpha = \phi_\alpha \gamma_\alpha. \quad (3.8)$$

A mixture is said to be saturated if the constituents satisfy

$$\sum_{\alpha=1}^N \phi_{\alpha}(\mathbf{x}, t) = 1. \quad (3.9)$$

Finally, it is useful to introduce the concept of *incompressibility*. In a theory of mixtures, the α^{th} constituent is incompressible if $\dot{\gamma}_{\alpha}$ is zero which physically means that γ_{α} can only depend on \mathbf{X}_{α} . Consequently, it is usually assumed that, when the α^{th} constituent is incompressible, γ_{α} is constant. In any case, the mixture is incompressible when every constituent in the mixture is incompressible.

3.1.2 The mass balance equation for mixtures

We suppose that the general mixture \mathcal{B} occupies a fixed spatial region Ω in \mathbb{R}^3 with surface $\partial\Omega$ and we introduce a general term modeling the inter-component mass exchange per unit volume $\Gamma_{\alpha}(\mathbf{x}, t)$. Each of the N constituents must satisfy its own mass balance equation, which written in the integral formulation reads

$$\frac{\partial}{\partial t} \int_{\Omega} \rho_{\alpha} dV = - \oint_{\partial\Omega} \rho_{\alpha} \mathbf{v}_{\alpha} \cdot \mathbf{n} dS + \int_{\Omega} \Gamma_{\alpha} dV, \quad (3.10)$$

where \mathbf{n} is the outward vector of the element of surface dS . Requiring that (3.10) holds for every spatial volume, we can localize the mass balance equation for the α^{th} constituent and, by means of the divergence theorem, we can obtain the Eulerian local form of (3.10) which is

$$\frac{\partial \rho_{\alpha}}{\partial t} + \nabla \cdot (\rho_{\alpha} \mathbf{v}_{\alpha}) = \Gamma_{\alpha}. \quad (3.11)$$

Then using equation (3.3) and the vector calculus identity $\nabla \cdot (f\boldsymbol{\psi}) = \boldsymbol{\psi} \cdot \nabla f + f \nabla \cdot \boldsymbol{\psi}$, where f is a scalar function and $\boldsymbol{\psi}$ a vector field, equation (3.11) yields to

$$\dot{\rho}_{\alpha} + \rho_{\alpha} \nabla \cdot \mathbf{v}_{\alpha} = \Gamma_{\alpha}. \quad (3.12)$$

If the α^{th} constituent is incompressible, i.e. $\dot{\gamma}_\alpha = 0$, from (3.8) we have that $\dot{\rho}_\alpha = \dot{\phi}_\alpha \gamma_\alpha$ and it is possible to write (3.12) in term of the volume fraction ϕ_α

$$\dot{\phi}_\alpha + \phi_\alpha \nabla \cdot \mathbf{v}_\alpha = \frac{\Gamma_\alpha}{\gamma_\alpha}, \quad (3.13)$$

or equivalently

$$\frac{\partial \phi_\alpha}{\partial t} + \nabla \cdot (\phi_\alpha \mathbf{v}_\alpha) = \frac{\Gamma_\alpha}{\gamma_\alpha}. \quad (3.14)$$

Finally, we should introduce the mass balance equation for the mixture. We define the mixture density at (\mathbf{x}, t) as

$$\rho = \sum_{\alpha=1}^N \rho_\alpha = \sum_{\alpha=1}^N \gamma_\alpha \phi_\alpha \quad (3.15)$$

and the mixture velocity at (\mathbf{x}, t) as the mass-weighted average of the constituent velocities:

$$\mathbf{v} = \frac{1}{\rho} \sum_{\alpha=1}^N \rho_\alpha \mathbf{v}_\alpha = \frac{1}{\rho} \sum_{\alpha=1}^N \gamma_\alpha \phi_\alpha \mathbf{v}_\alpha. \quad (3.16)$$

For a closed system, i.e. without any external sources, the mixture density is conserved:

$$\partial_t \rho + \nabla \cdot (\rho \mathbf{v}) = 0 \quad (3.17)$$

and consequently if the N equations (3.11) are summed, the mass exchange terms and the component velocities are constrained to satisfy

$$\sum_{\alpha=1}^N \Gamma_\alpha = 0 \quad \text{and} \quad \sum_{\alpha=1}^N \nabla \cdot (\phi_\alpha \mathbf{v}_\alpha) = \sum_{\alpha=1}^N \frac{\Gamma_\alpha}{\gamma_\alpha}. \quad (3.18)$$

Moreover, if the densities are matched, i.e. $\gamma_\alpha = \gamma$, the mixture velocity is incompressible:

$$\nabla \cdot \left(\sum_{\alpha=1}^N \phi_\alpha \mathbf{v}_\alpha \right) = 0. \quad (3.19)$$

3.2 Diffuse interface model for tumor growth

3.2.1 Model formulation

Following [8, 10], we consider a simple binary model of a tumor lesion: a mixture composed by a cellular phase of proliferating cancerous cells with volume fraction ϕ_c and a liquid phase of both host cells and interstitial fluid environment, in which dead cells may be present, with volume fraction ϕ_l . In the present work we consider healthy cells to behave as liquid phase. These two phases fill all the available space and consequently the saturation relation holds:

$$\phi_c + \phi_l = 1. \quad (3.20)$$

We associate a velocity with each phase: \mathbf{v}_c is the average velocity for the cell phase and \mathbf{v}_l for the liquid phase.

As described in subsection 3.1.2, we propose a model whose governing equations are driven from mass balances for both constituents. For both phases, we take into account a volumetric source of mass production/loss, Γ_i , $i = c, l$, and a flux of mass due to chemotactic movements, symbolized by K_c . The mass balances for the cancerous cell phase and the liquid phase are expressed as follows:

$$\gamma \left[\frac{\partial \phi_c}{\partial t} + \nabla \cdot (\phi_c \mathbf{v}_c) \right] = \Gamma_c + \nabla \cdot K_c \quad (3.21)$$

$$\gamma \left[\frac{\partial \phi_l}{\partial t} + \nabla \cdot (\phi_l \mathbf{v}_l) \right] = \Gamma_l - \nabla \cdot K_c \quad (3.22)$$

where, as defined in section 3.1, γ is the true mass density of both constituents. Indeed, we make the biological hypothesis that the interstitial liquid and the tumoral cells have the same density equal to the water density γ , which is a reasonable assumption since being cells are composed mostly of water. It is also assumed that γ is constant, which physically means that both constituents are incompressible. Since we are considering a close mixture, the mass transfer rates between the two

phases are matched, i.e. $\Gamma_c = -\Gamma_l$, which biologically represents a volume conversion rate among them. Effectively, as the liquid phase contains both dead cells and healthy living cells, we have that when a cancerous cell dies, it becomes part of the liquid phase. Viceversa, if a healthy cell turns into a cancerous cell, it belongs to the cellular phase.

As mentioned, we consider a flux of mass driven by an increasing chemotactic gradient of nutrients in the form $K_c = -k_n \rho_c \mathbf{T} \nabla n$, where k_n is a specific chemotactic parameter, \mathbf{T} is a tensor defining the preferential directions of the chemotactic motion along the alignment of fibers and n is the oxygen concentration. This tensor is obtained handling with the diffusion tensor \mathbf{D} , described in Chapter 2. How to compute \mathbf{T} will be explained in Chapter 4 section 2. The introduction of the tensor \mathbf{T} in modeling the flux of mass is particularly important as glioblastoma progression has been demonstrated to preferentially grow along the directions of the white matter fibers [11]. In other words, including the tensor \mathbf{T} , we manage to describe the anisotropic extension of glioblastomas. At the same time, the term K_c is able to describe the tendency of tumor cells to direct their movements up to the gradient of a chemoattractant and down to the gradient of a chemorepellent. The term $\nabla \cdot K_c$ appears both in (3.21) and (3.22) but with opposite signs: biologically, this means that when the cancerous cells move in a region driven by an increasing gradient of nutrients, then the host tissue and the interstitial fluid should move in turn. In fact, in each point of the domain the saturation relation must hold.

Finally, if both constituents are incompressible, the mixture is incompressible, i.e.

$$\nabla \cdot (\phi_c \mathbf{v}_c + \phi_l \mathbf{v}_l) = 0 \quad (3.23)$$

and consequently, (3.21) and (3.22) can be rewrite in the equivalent form:

$$\frac{\partial \phi_c}{\partial t} + \nabla \cdot (\phi_c \mathbf{v}_c) = \frac{\Gamma_c}{\gamma} - \nabla \cdot (k_n \phi_c \mathbf{T} \nabla n) \quad (3.24)$$

$$\nabla \cdot (\phi_c \mathbf{v}_c + (1 - \phi_c) \mathbf{v}_l) = 0. \quad (3.25)$$

At this point, in order to close the system it is necessary to define the convective velocities \mathbf{v}_c and \mathbf{v}_l through the introduction of proper laws. Probably, defining the relative movement of the phases is the most delicate point in dealing with this kind of models. This can be done either on the basis of phenomenological arguments [1], or writing momentum balance equations [12] or by a thermodynamical approach [83]. In the following, using the third method, we introduce the constitutive laws for the velocities.

3.2.2 Constitutive equations

In this section we propose an energy formulation for viscous interactions and mechanical forces which lead to cell-cell and cell-matrix adhesion. The purpose is to define constitutive - thermodynamically consistent - equations for the phase velocities in order to close the model [1]. At biological level, cells are able to adhere to each other or to the extracellular matrix they are in contact with through adhesion molecules called CAMs located at the cellular plasma membrane [45, 59]. Moreover CAMs could play a pivotal role in cancer progression and invasion and contribute to a variety of functions including signal transduction, cell growth and differentiation [56].

These interaction mechanisms can be modeled by the expression of Helmholtz free energy for the cancerous phase [83], which can be written as an integral taken over the entire tumor/host domain:

$$F_c = \int_{\Omega} \left(\psi(\phi_c) + \frac{\epsilon^2}{2} |\nabla \phi_c|^2 \right) d\Omega. \quad (3.26)$$

In the above equation, ψ represents the bulk free energy per unit of volume due to local interactions while the second (gradient energy) term models larger range interactions among the components and penalizes bigger gradients of cellular concentrations. In particular, the thickness of the diffuse interface between the tumor and host tissue depends on the constant ϵ with a width that ranges between 1-100

μm [17]. Specifically, smaller values of ϵ lead to a less diffuse interfacial region is [83].

Then, we hypothesize that the energy dissipation in the system is due only to viscous interactions among cells and thus, mathematically, we have that

$$W = \int_{\Omega} \left(\frac{M\phi_c}{2} (\mathbf{v}_c - \mathbf{v}_l)^2 \right) d\Omega \quad (3.27)$$

where M is the friction parameter, that we will take as a constant.

Following Doi and Onuki [43], we use a variational approach to the previous energy formulation in order to obtain constitutive laws for the velocities \mathbf{v}_c and \mathbf{v}_l . The Rayleigh's principle indicates that the system dynamic can be obtained by minimizing Rayleighian, defined as

$$R = W + \frac{dF_c}{dt}. \quad (3.28)$$

Equation (3.28) guarantees that the expression for phase velocities respects the second law of the thermodynamics.

Generally speaking, this principle is a simply variational statement for general kinetic equation for the thermodynamic quantities x_i ($i = 1, 2$):

$$\frac{dx_i}{dt} = - \sum_j L_{ij}(x) \frac{\partial F(x_i)}{\partial x_j} \quad (3.29)$$

where F is the thermodynamic free energy and L_{ij} are the kinetic coefficients. Calling M_{ij} the inverse matrix of L_{ij} , equation (3.29) becomes:

$$\sum_j M_{ij} \frac{dx_j}{dt} = - \frac{\partial F}{\partial x_i}. \quad (3.30)$$

Equation (3.30) can be stated in a variational principle: solving equation (3.30) is

equivalent to minimize the Rayleighian

$$R = \sum M_{ij} \dot{x}_i \dot{x}_j + \sum \frac{\partial F}{\partial x_i} \dot{x}_i \quad (3.31)$$

with respect to \dot{x}_i . Finally, calling $W = \sum M_{ij} \dot{x}_i \dot{x}_j$ the dissipation function, since it represents the energy dissipation for given \dot{x}_i , and $\dot{F} = \sum \frac{\partial F}{\partial x_i} \dot{x}_i$ the free energy change due to \dot{x}_i , (3.28) is obtained.

We define the Rayleigh coefficient for the tumor model replacing the expression of the adhesion energy (3.26) and the dissipation energy (3.27) in the definition given by Doi and Onuki (3.28) and we impose the incompressibility constraint introducing the Lagrange multiplier p . The functional to be minimized is

$$R = \int_{\Omega} \left[\frac{M\phi_c}{2} (\mathbf{v}_c - \mathbf{v}_l)^2 + \left(\frac{\partial\psi}{\partial\phi_c} - \epsilon^2 \Delta\phi_c \right) (\Gamma_c + \nabla \cdot K_c - \nabla \cdot (\phi_c \mathbf{v}_c)) + \right. \\ \left. - p \nabla \cdot (\phi_c \mathbf{v}_c + \phi_l \mathbf{v}_l) \right] d\Omega. \quad (3.32)$$

Then we compute the functional derivative with respect to \mathbf{v}_c and \mathbf{v}_l and we impose $\frac{\delta R}{\delta \mathbf{v}_i} = 0$ with $i = c, l$. The constitutive equations are:

$$M\phi_c(\mathbf{v}_l - \mathbf{v}_c) + \phi_l \nabla p = 0 \quad (3.33)$$

$$M\phi_c(\mathbf{v}_c - \mathbf{v}_l) + \phi_c \nabla \left(\frac{\partial\psi}{\partial\phi_c} - \epsilon^2 \Delta\phi_c \right) + \phi_c \nabla p = 0. \quad (3.34)$$

Eliminating the pressure p in the equations (3.33) and (3.34), we obtain the relative movement of the two phases

$$\mathbf{v}_c - \mathbf{v}_l = -\frac{1 - \phi_c}{M} \nabla \left(\frac{\partial\psi}{\partial\phi_c} - \epsilon^2 \Delta\phi_c \right). \quad (3.35)$$

If there aren't any external forces and the mixture is characterized by a high viscosity, the center of mass doesn't move, i.e. $\mathbf{v} = \phi_c \mathbf{v}_c + \phi_l \mathbf{v}_l = 0$. In this case, it is

possible to explicate the velocity of the cell phase by a Darcy-like law, as follows:

$$\mathbf{v}_c = -K(\phi_c)\nabla\Sigma \quad (3.36)$$

$$K(\phi_c) = \frac{(1 - \phi_c)^2}{M} \quad (3.37)$$

where K is a motility coefficient possibly depending on the volume fraction and Σ is the excess of pressure exerted by the cells which is defined by

$$\Sigma = \frac{\partial\psi}{\partial\phi_c} - \epsilon^2\Delta\phi_c = f(\phi_c) - \epsilon^2\Delta\phi_c. \quad (3.38)$$

Moreover if equations (3.33) and (3.34) are summed, we have that $\nabla p = -\phi_c\nabla\Sigma$: the interstitial pressure p and the excess of pressure Σ have the same typical value χ and therefore the term $\epsilon/\sqrt{\chi}$ gives a characteristic distance of interaction between cells, typically estimated by the cell size.

Conclusively, it is important to explain the biological meaning of Σ in (3.36). We consider the case of a homogeneous system, i.e. $\nabla\phi_c = 0$, so that Σ is simplified to $f(\phi_c) = \frac{\partial\psi}{\partial\phi_c}$. For physical consistency, cell-cells interactions should be attractive under a certain density of cells and repulsive at higher densities. Mathematically, it exists a threshold value ϕ_e called *state of equilibrium* [1] for which $f(\phi_e) = 0$ and no excess pressure is exerted on neighbors. Thus, for $\phi_c < \phi_e$, $f(\phi_c) < 0$ and cells are attracted to each other, while for $\phi_c > \phi_e$, $f(\phi_c) > 0$ and cells experience a repulsive force. Unlike the Cahn-Hilliard type proposed in [83], we use a phenomenological form of $f(\phi_c)$ [1, 8, 10] that obeys to the physical and biological constraints explained above:

$$f(\phi_c) = E \frac{\phi_c^2 (\phi_c - \phi_e)}{1 - \phi_c} \quad (3.39)$$

where E is the Young Modulus of the brain matter. A schematic scheme of cells behavior in relation to $\Sigma(\phi_c)$ is depicted in figure 3.1 [1, 8, 10].

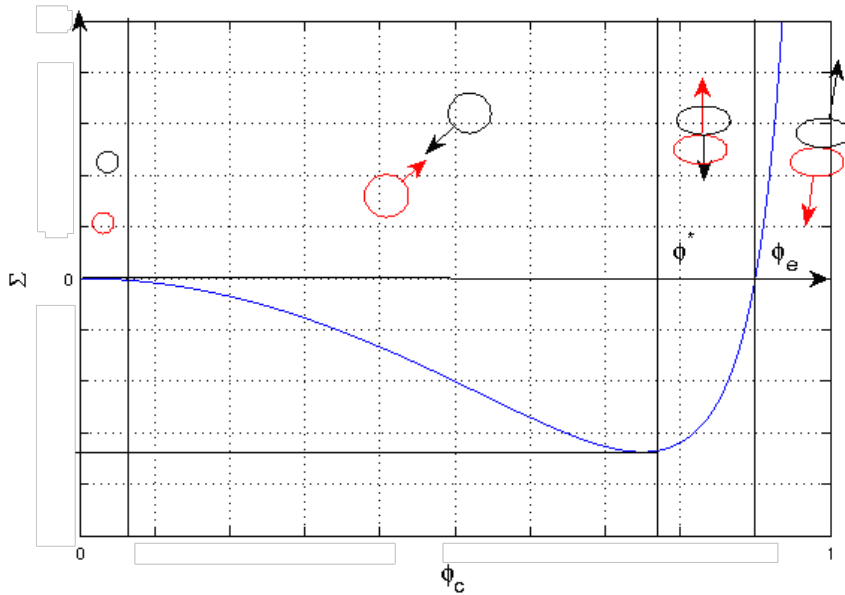


Figure 3.1: Schematic diagram showing the behavior of cells in relation to $\Sigma(\phi_c)$ in the case of a homogeneous tissue. Two cells which are far apart ignore each other, but, if the distance between them falls below a certain value, fact that could be caused by an increase of density, they are attracted to each other. When cells in contact are pulled apart, an adhesive force competes with cell separation and if they are too close, they experience a repulsive force. The repulsive force becomes infinite in the limit as the cells are packed so densely that they fill the whole control volume [8]. In the figure, the black arrows represent the forces experienced by the black cells due to the presence of the red cells (and conversely).

3.2.3 Nutrient diffusion

In this section we investigate the relation between nutrients availability and tumor growth and we propose a governing equation for the nutrient concentration n . In the present work, we consider oxygen as the main nutrient for tumoral cells and we suppose that the vasculature is homogeneous in the whole domain. We do not take into account the angiogenesis, that is the formation of new blood vessels, in the model. In this situation, tumoral cells receive oxygen and growth factors only via diffusion through the host tissue (figure 3.2). As mentioned earlier, the term Γ_c in (3.21) represents the cell proliferation/death rate and it is assumed to be

dependent linearly on the concentration of the diffusing nutrient n :

$$\frac{\Gamma_c}{\gamma} = \nu_c \frac{\rho_c}{\gamma} \left(\frac{n}{n_s} - \delta_c \right) (1 - \phi_c) = \nu_c \phi_c \left(\frac{n}{n_s} - \delta_c \right) (1 - \phi_c) \quad (3.40)$$

where ν_c is the tumoral cell proliferation rate, n_s is a typical nutrient concentration inside the tissue and δ_c is the rate of apoptosis in hypoxia conditions. Splitting (3.40), the term $\nu_c \phi_c (n/n_s)(1 - \phi_c)$ corresponds to the rate of volume growth due to mitosis while $\nu_c \phi_c \delta_c (1 - \phi_c)$ is the rate of volume loss due to apoptosis, which is actually caused by scarceness of nourishment. The volumetric cell proliferation/death term is weighed by $(1 - \phi_c)$ because as ϕ_c gets close to 1, the proliferation/death decreases: as a matter of fact, when ϕ_c is equal to 1 the system is in the saturation state and all the available space is filled by the cancerous volume fraction, which has reached its maximum values.

Then we propose a diffusion reaction equation for the nutrients concentration n . At a first approximation, we model the host tissue at equilibrium, where the net nutrient uptake therein is negligible compared to the uptake by tumor cells. In particular, we assume that whatever oxygen is uptake by the host tissue it is instantaneously replaced by the normal vasculature. This is not the case of the tumor, where the uptake in general exceeds the supply, as discussed before [83]. Therefore the distribution of nutrients is described by the following PDE:

$$\frac{\partial n}{\partial t} = \nabla \cdot (\mathbf{D} \nabla n) + S_n(n_s - n) - \delta_n \phi_c n. \quad (3.41)$$

where \mathbf{D} is the diffusion tensor, δ_n is the rate of consumption of nutrients by tumor cells, S_n is the blood tissue transfer rate of nutrients and n_s is the physiological concentration of oxygen in blood at the capillaries. In particular, each component of tensor \mathbf{D} expresses the diffusion value of water molecules along a specific direction. Since we make the biological assumption that oxygen is carried by water, then the local values of tensor \mathbf{D} describe how nutrients diffuse effectively in a specific point of the brain. As regards the terms with S_n and δ_n , we have that $S_n(n_s - n)$

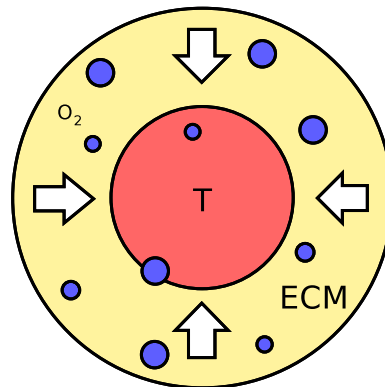


Figure 3.2: We consider oxygen as the main nutrients for cancerous cells and we suppose that they receive the supplies only via diffusion through the host tissue.

describes the source of nutrients from the vasculature and $\delta_n \phi_c n$ models the nutrient uptake by cells.

3.3 Parameter estimation

One of the major limiting factors in the usefulness of mathematical models lies within the ability to parameterize them. In fact, in literature it is possible to find a wide range of parameters and the goal of mathematicians is to find out which parameters best suit the model in order to obtain a realistic outcome. In this section, we discuss the evaluation of the biological values found in literature for the parameters used in the previous equations.

First of all, we need to evaluate the interstitial fluid pressure χ , the cell volume fraction at mechanical equilibrium ϕ_e and the inter-phase friction parameter M . For many years, the research on tumor pathophysiology, that is the study of the functional changes associated with a disease, lagged behind that on cellular events of cancer. Recently, that field of study has gained in importance and, in particular, the alterations of the vasculature and the interstitium have begun to be object of study. In fact they seem to have a specific role in the growth of the tumor and in

its clinical development. For example, brain tumors are characterized by a higher interstitial fluid pressure (IPF) compared to that of the normal brain tissue, which is around 106.64 Pa [5]. In [26], the intratumor pressure has been examined as a function of tumor size. They found out that as the tumor size increases, IPF rises presumably due to the proliferation of tumor cells in a confined area and due to a reduction in tumor blood flow. Measurements in experimental tumors have given an estimation of 1199 ± 333 Pa for the IPF [26]. Other reasons for the increased IPF might be vessels abnormalities, fibrosis, contraction of the interstitial matrix and enlargement of the extracellular space (ECS). In [7], the enlargement of the ECS in different brain tumors has been studied and a value of 61,1% is given for the glioblastoma. Since neoplastic tissues are formed by vascular, interstitial and cellular space, it seems reasonable to estimate ϕ_e with 38,9 %. For what concerns the hydraulic conductivity, it has been studied in [70] that it depends on the tissue interstitial space volume fraction, cell diameter and tissue architecture (tortuosity of the interstitial space) and it is defined as the ratio between the Darcy permeability and the viscosity of the tissue. Thus, from (3.37) we are allowed to estimate M as the inverse of the hydraulic conductivity obtaining values between $1377.9 - 4286.7 \text{ mm}^{-2} \text{ Pa day}$.

Then, we have to evaluate the characteristic distance of cells interactions which can be approximated by the diameter of a cell which ranges between 10 and 20 μm , values that have been observed in experimental data by [75, 77]. The proliferation parameter can be estimated in vitro from typical doubling time of well oxygenated glioma cells and it varies between 24 h and 48 h [17, 27], while an estimate of the threshold for cell death rate due to anoxia is given by the range 0.15 - 0.5 [17, 20]. In order to obtain an evaluation of the oxygen consumption rate δ_n we make use of the relation $l_n = \sqrt{D_n/\delta_n}$, where l_n is the distance covered by a molecule of oxygen before being uptake by a cancerous cell and D_n is the average oxygen diffusion coefficient. In [13, 17, 57], l_n is set to 100 μm while, in [4, 29, 42, 77], D_n is evaluated with $86.4 \text{ mm}^2\text{day}^{-1}$. Then, we have to evaluate S_n and n_s . The first

is the oxygen production rate from the source of nutrient, i.e. blood supply, and its value, which is hard to estimate, is set to 10^4 day^{-1} in [10] while the second is the initial oxygen concentration outside the tumor and it has been evaluated with 0.07 mM in [81] is evaluated to be 0.07 mM.

Unfortunately, data on the chemotactic coefficient of glioma cells in response to oxygen concentration are not present in literature, thus we refer to typical chemotactic coefficient found for bacteria in response to glucose. In particular in [16] it was estimated to be equal to $1296 \text{ mm}^2 \text{ mM}^{-1} \text{ day}^{-1}$. Finally, the Young modulus E is set to 694 Pa in [11].

Of course more biological experiments are highly requested to derive biological parameters which are consistent with the object of the research.

In table 3.1 we report a scheme of the biological parameters previously introduced.

Parameter	Description	Value	References
ϕ_e	Cell volume fraction	0.38	[7]
M	Interphase friction	$1377.9\text{-}4286.7 \text{ mm}^{-2} \text{ Pa day}$	[70]
χ	IPF in healthy brain	106.64 Pa	[5]
χ	IPF in GBM	866-1530 Pa	[26]
$\epsilon/\sqrt{\chi}$	GBM cell size	10 - 20 μm	[81, 75, 77]
ν_c	GBM cell proliferation rate	$0.5\text{-}1 \text{ day}^{-1}$	[17, 27]
δ_c	Threshold of O_2 for anoxia	0.15 -0.5	[17, 20]
D_n	O_2 diffusion coefficient in brain	$86.4 \text{ mm}^2 \text{ day}^{-1}$	[4, 29, 42, 77]
δ_n	O_2 consumption rate of the brain	8640 day^{-1}	[4, 29, 42, 77]
S_n	Blood tissue transfer rate of O_2	10^4 day^{-1}	[10]
n_s	O_2 concentration in brain vessels	0.07 mM	[81]
l_n	O_2 penetration length	0.1 mm	[13, 17, 57]
k_n	Chemotactic coefficient	$1296 \text{ mm}^2 \text{ mM}^{-1} \text{ day}^{-1}$	[16]
E	Young modulus	694 Pa	[11]

Table 3.1: Estimation of the model parameters taken from literature in healthy and diseased brain.

3.4 The complete model formulation

To conclude the chapter, in the following, we sum up the governing equations for the glioblastoma tumor growth.

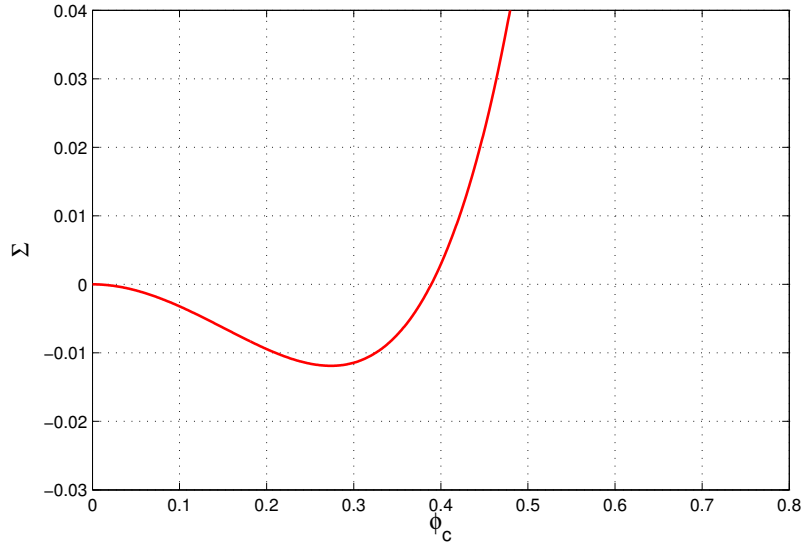


Figure 3.3: Excess stress Σ/E exerted by the cells in a homogeneous tissue ($f/E = \Sigma/E$ as $\nabla\phi = 0$) with real data.

In order to perform numerical simulations, it is useful to adimensionalize (3.24) and (3.41) with respect to nutrient concentration. In particular, given n_s the physiological concentration of oxygen in blood vessels, we have that the adimensional concentration \hat{n} is obtained as

$$\hat{n} = \frac{n}{n_s}, \quad (3.42)$$

where n is the dimensional variable. In this way, both \hat{n} and ϕ_c belong to the interval $[0, 1]$, and it will be easier to understand the numerical results. Regarding space and time variables, we will not consider dimensionless quantities. Indeed, the aim of the present work is to perform numerical simulations on a real geometry, using patient-specific data.

Dropping the hat and the index for the cell phase, the governing equations can be

written as

$$\frac{\partial \phi}{\partial t} = \nabla \cdot \left(\frac{\phi(1-\phi)^2}{M} \nabla (f(\phi) - \epsilon^2 \Delta \phi) \right) + \nu \phi (n - \delta)(1 - \phi) - \nabla \cdot (k_n \mathbf{T} \phi n_s \nabla n) \quad (3.43)$$

$$\frac{\partial n}{\partial t} = \nabla \cdot (\mathbf{D} \nabla n) + S_n(1 - n) - \delta_n \phi n. \quad (3.44)$$

Chapter 4

Numerical Implementation

In the present chapter, we give details on the numerical implementation of the model presented in chapter 3.

In the first section, we illustrate how to obtain a computational mesh from medical images. In particular, numerical simulations of biological phenomena require very complex domains and thus it is essential to create a well refined mesh close to the reality without exceeding in computational costs. We start from a series of MRIs of a patient affected by glioblastoma, which have been gently provided by the *Istituto Neurologico Carlo Besta*. To obtain the labeled map of the brain, we make use of a software called *Slicer3D* [64]. Then, we manage to create the computational mesh using an open-source software named *Vmtk* (Vascular Modeling Tool Kit, [31]) through a Python interface. *Vmtk* has been realized on the basis of other open-source libraries such as *ITK* (Insight segmentation and registration ToolKit [25]), *VTK* (Visualization ToolKit [32]) and *Tetgen* (Quality Tetrahedral Mesh Generator [76]). To visualize and analyze the images we use an open-source software based on the VTK library named *Paraview* [58].

In the second section of this chapter, we describe how we include diffusion tensor medical data in the model. In particular, we illustrate the difference between the diffusion tensor \mathbf{D} and the tensor of preferential directions \mathbf{T} . We also introduce the problem of *medical images registration* and the use of an open source

software named *FSL* [18], which offers two robust registration tools named FNIRT and FLIRT.

In the third section, the continuum and discrete weak statements of the model are introduced. We use linear tetrahedron P_1 elements to discretize the problem and we realize numerical simulations making use of an open-source software called *FEniCS* [60], which is capable of providing efficient solutions of differential equations using the finite elements method.

4.1 Mesh creation

4.1.1 Medical image segmentation

The segmentation of images is the process of identifying and labeling regions of interest within an image. The usual starting point in medical image segmentation is a grey scale MR image, as shown in figure 4.1. As discussed in chapter 2, the grey intensity is correlated to the tissue's diffusion proprieties. To obtain information about tissues and their features it is necessary to identify brain areas and put the labels on the different regions. To achieve this goal, we start from a series of MRIs and we use a software package for visualization and computation of medical images, called *Slicer3D*. The procedure is performed using a *module* implemented in the software called *EMSegmenter*, thanks to which anatomical structures can be automatically segmented. We identify four areas of interest, i.e. gray matter, white matter, cerebrospinal fluid and background, and we specify the labels to associate to each of this region. Then, since the algorithm uses anatomical atlas, we link the probabilistic atlases to the anatomical structures defined above and finally we can run the algorithm and create the labeled map we need. The segmented image obtained is depicted in figure 4.2. Once the brain segmentation is done, we manually segment the glioblastoma tumor region using a *module* named *Editor*, as shown in figure 4.3.

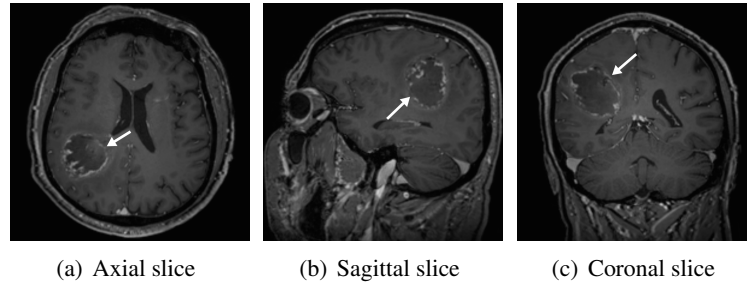


Figure 4.1: In the above figures axial, sagittal and coronal slices of the T1 3D TFE mdc rest SENSE we used for image segmentation are depicted. It is possible to see the tumor region indicated by the white arrow.

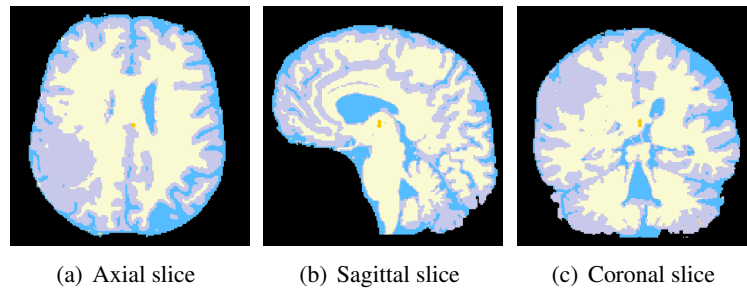


Figure 4.2: Segmented image of the brain. The white region represents the white matter, while the grey areas indicate the grey matter. The cerebrospinal fluid is labeled by the blue color. At this step, the tumor is not segmented yet and due to the grey intensity of tumor's voxels, the cancerous region is seen as grey matter by *EMSegmenter*.



Figure 4.3: After the whole brain segmentation, glioblastoma is manually segmented slice by slice and then overlapped to the labelled map. In the figure, three slices of the brain map in the tumoral interval are illustrated, from the bottom to the top of the head.

4.1.2 Mesh generation

After the creation of the brain labeled map, we need to obtain the computational mesh. To achieve our goal, we use some algorithms belonging to the *vtk* library. Firstly, the brain surface is extracted from the labeled map, re-meshed with triangulation and cleaned and smoothed, as shown in figure 4.4. It is really important to obtain a regular triangulation without holes or intersection of edges. At this step, the mesh is still a 2D surface embedded in \mathbb{R}^3 . Once the surface is smooth and perfectly regular, the next step concerns the creation of the tetrahedral mesh. To perform the 3D computational mesh, we use an automatic mesh generator software called *Tetgen*, [76]. Then, the resulting unstructured grid is refined near the area where the cancer grows: in this way, the computational cost is kept under control as the numerical solution is computed in a more precise way only in the region of interest, as exemplified in figure 4.5. After the mesh refinement, it is necessary to superpose the labelled map to the grid such that the information of the tissues are passed on the geometry, as depicted in figure 4.6.

To perform the mesh creation process we use numerical codes which have been proposed in a previous research [41] developed at the Politecnico di Milano. A special thanks is given to M.Manica and E. Faggiano

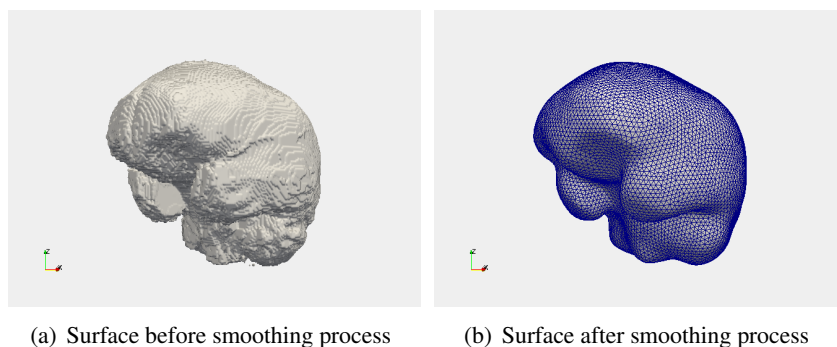


Figure 4.4: Figure (a): the surface is extracted from the labeled map using the *vtkmarchingcubes* algorithm. Figure (b): the rough surface is smoothed and cleaned in order to obtain a regular surface triangulation.

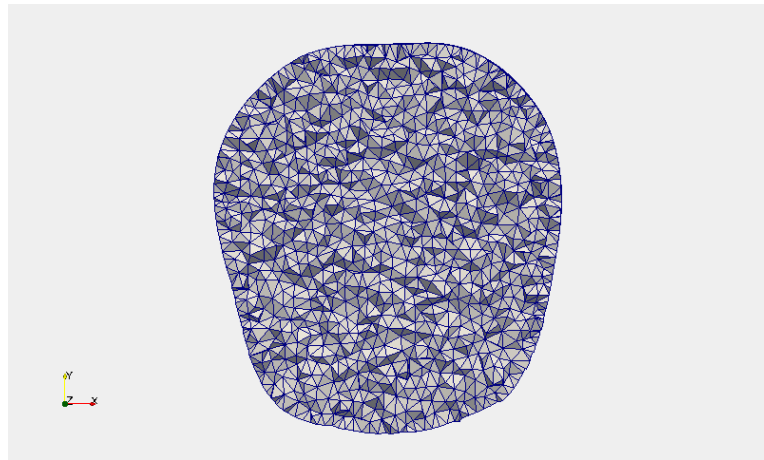
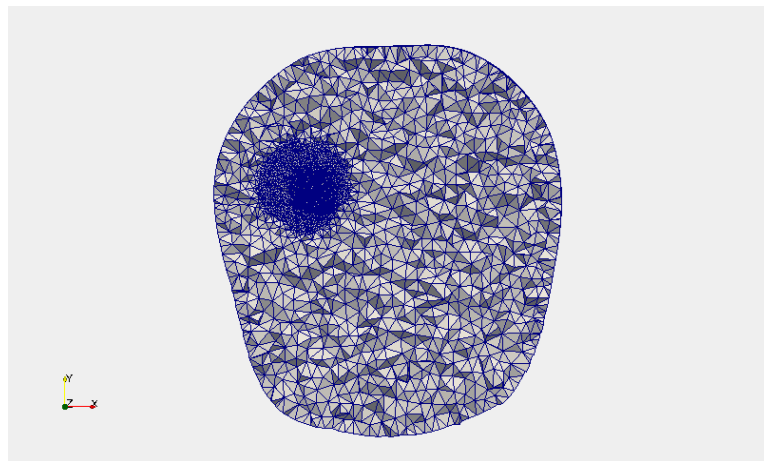
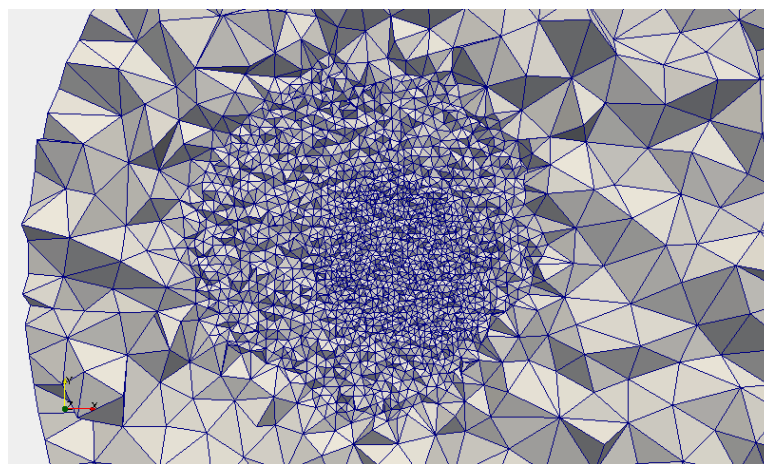
(a) Clipped mesh plane xy - before the refinement(b) Clipped mesh plane xy - after the refinement(c) Clipped mesh plane xy - detail of the refined area

Figure 4.5: Clip of the 3D mesh before (figure (a)) and after (figures (b) and (c)) the refinement of the tumoral area. In this way the computed solution is more accurate in the area of interest and computational costs are kept under control.

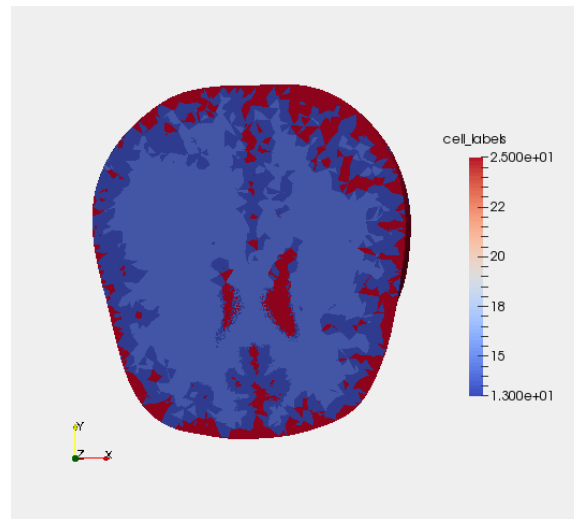
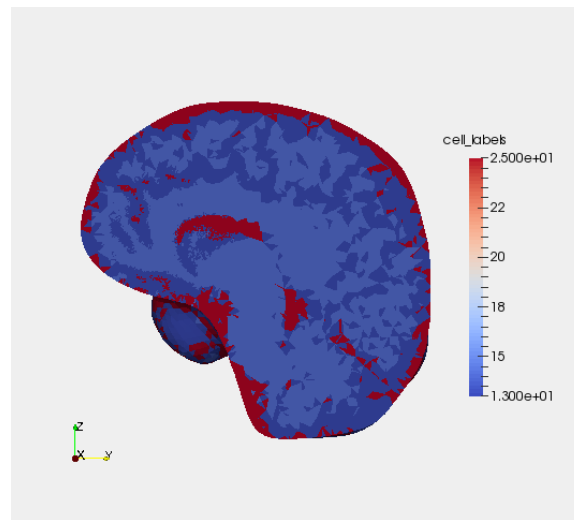
(a) Clipped labeled mesh - view plane xy (b) Clipped labeled mesh - view plane yz

Figure 4.6: Labeled mesh. Thanks to the algorithm proposed by M.Manica [41], the information about biological tissues are passed on the mesh. The red area represents the cerebrospinal fluid, the light blue area represents the white matter while the dark blue area stands for the grey matter. The brain is cut with an oblique plane in order to show the interior area.

4.2 Modeling tensor \mathbf{D} and tensor \mathbf{T}

In this section, we describe how we deal with the diffusion tensor medical data, gently provided by the *Istituto Neurologico Carlo Besta*, and how we manage to include real data in the model. We start from these biological facts:

- cerebral matter is heterogeneous: diffusion in grey matter is isotropic while in white matter it is anisotropic. Indeed water diffusion is relatively unimpeded in the direction parallel to the fiber orientation while it is highly restricted and hindered in the directions perpendicular to the fibers of the white matter;
- glioblastoma presents an infiltrative nature and grows in white matter more than in grey matter, following the alignment of the fibers;
- cells have the capability to migrate and tend to move towards higher concentration of nutrients.

As described in chapter 2, diffusion tensor imaging is based on the computation of water diffusion in biological tissue. Water diffusion is caused primarily by random thermal fluctuations and it is modulated by the interactions with obstacles in the environment such as cellular membranes, organelles and ECM fibers. Thus, diffusion tensor \mathbf{D} is able to reveal the microstructure of the tissues and to describe the degree of anisotropy and the orientation of diffusion. Our work is driven by the idea that knowing the microstructure of the brain and the preferential directions of water diffusion could be helpful in predicting more truthfully the development of glioblastoma since anisotropy influences nutrients diffusion and cells' movements. Therefore, we include the tensor \mathbf{D} in the diffusion term of equation (3.44). As mentioned in subsection 3.2.3, in this way we are allowed to know locally the value of the oxygen diffusion coefficient in each point of the domain and consequently to obtain a patient-specific model. Moreover, we add the tensor \mathbf{T} in the flux of mass of the cellular fraction in (3.43). It expresses the preferential directions of motility

and it is the mathematical object that includes anisotropy in the model.

In the following we describe how to obtain tensor the \mathbf{D} and the tensor \mathbf{T} from diffusion tensor medical images.

The starting point are the six maps of the DTI in greyscale, each of which represents a component of the diffusion tensor, as shown in figure 4.7. We remind that the tensor is symmetric, i.e. $D_{ij} = D_{ji}$, and that the diagonal components D_{xx} , D_{yy} , D_{zz} represent the diffusion variances along the x , y , z axis while the off diagonal terms D_{xy} , D_{xz} , D_{yz} represent the diffusion covariance. A diffusion value is associated to the voxels of each image: for example the voxels within the area occupied by the lateral ventricles, where there is fluid, have a value of $2999 \text{ m}^2\text{s}^{-1}$, while the voxels in a region of white matter have an intensity in the range of $800\text{-}1100 \text{ m}^2\text{s}^{-1}$. Thus, the former are brighter while the latter appear darker.

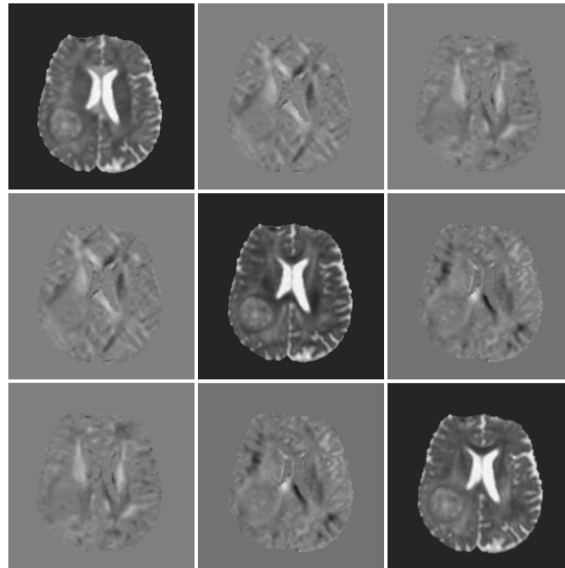


Figure 4.7: The six medical images of the diffusion tensor. Each of them represents a component of the tensor. Along the diagonal there are D_{xx} , D_{yy} , D_{zz} , while the off diagonal images represent the covariance terms D_{xy} , D_{xz} , D_{yz} . The tensor is symmetric, i.e. $D_{ij} = D_{ji}$

In order to obtain tensor \mathbf{D} , we need to specify that DTI medical images must be registered with the T1-MRI image used for creating the computational mesh. As a matter of fact, the six images of the DTI are the result of a phase of post-processing of DWIs acquired during medical examinations and thus they are not necessarily registered with the T1 data. We register D_{ij} images on the T1 used for the mesh creation thanks to an opens source software called *FSL* [18], which offers two fully automated and accurate registration tools named *FLIRT* and *FNIRT*. Once the medical images are aligned, the extrapolation of the data from each of the D_{ij} images can be obtained by an algorithm [41] that associates the diffusion value of a specific voxel in the medical image to the right tetrahedron which occupies the same location (of the voxel) in the computational mesh, as illustrated in figure 4.8. The resulting data are then simply included in the model thanks to specific FEniCS functions, as exemplified in the codes of appendix A.

Now, we focus on how the tensor of the preferential directions is obtained. For each voxel of the medical image, the tensor \mathbf{D} can be written as

$$\mathbf{D} = D_n \hat{\mathbf{D}} \quad (4.1)$$

where D_n is the mean diffusivity which is defined as $1/3Tr(\mathbf{D})$ and indicates the intensity of the diffusion process, whereas $\hat{\mathbf{D}}$ takes into account the anisotropy of the random movements in the different directions. We remind that the trace of a tensor is rotationally invariant and that the mean diffusivity is an inverse measure of the tissue density and it gives an indication of the anisotropy of the tissues and, indeed, it is very similar for both grey matter and white matter and higher for CSF. We illustrate the mean diffusivity on the mesh cut along the plane xy in figure 4.9. Supposing that cells can be chemotactically move along the same path of water diffusion, following the alignment of the fibers, the identification

$$\hat{\mathbf{D}} = \mathbf{T} \quad (4.2)$$

is possible. The tensor

$$\mathbf{T} = \begin{pmatrix} T_{xx} & T_{xy} & T_{xz} \\ T_{xy} & T_{yy} & T_{yz} \\ T_{zx} & T_{zy} & T_{zz} \end{pmatrix}$$

is defined for each tetrahedron of the mesh and expresses the preferential direction of diffusion within the element. Each component of \mathbf{T} is obtained weighting the corresponding component of the tensor \mathbf{D} with the mean diffusivity:

$$T_{ij} = \frac{D_{ij}}{1/3(D_{xx} + D_{yy} + D_{zz})}, \quad \text{with } i, j = x, y, z. \quad (4.3)$$

Moreover, comparing the components it is possible to know if the tissue is isotropic or anisotropic. In fact, in CSF and in grey matter $T_{xx} \approx T_{yy} \approx T_{zz} \approx 1$ and $T_{xy} \approx T_{xz} \approx T_{yz} \approx 0$: in these regions the tensor \mathbf{T} becomes the identity tensor and the diffusion is isotropic. In white matter, instead, T_{ii} with $i = x, y, z$ varies between 0 and 3 and T_{ij} with $i = x, y, z$ between -1 and 1 , excluding the value 0 and consequently the diffusion is anisotropic. For instance, if we consider a region where $T_{xx} \approx 3$, T_{yy} and T_{zz} should be almost zero which means that water will move more easily along x-direction. In figure 4.10 we illustrate the components of tensor \mathbf{T} on a mesh clipped along the xy plane in the middle point of z -axis.

As for the tensor \mathbf{D} , the components T_{ij} are then included in the relative governing equation thanks to specific FEniCS tools, as explained in appendix A. We should mention that we create the components of the tensors as objects defined on each tetrahedron of the mesh. Thanks to these specific FEniCS tools, we are able to transform the components as object defined on the degrees of freedom. In particular, the "changing" is done interpolating linearly the components that result continuous on the whole domain.

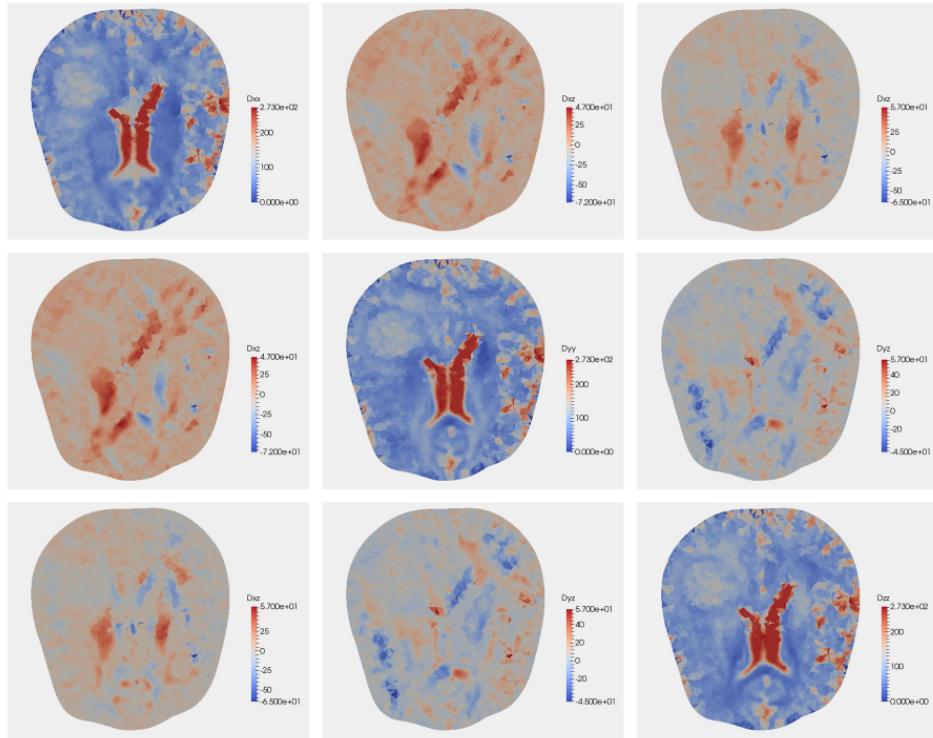


Figure 4.8: Patient-specific components of tensor \mathbf{D} depicted on the computational mesh cut along the plane xy . Comparing the images of the diagonal components of the tensor \mathbf{D} , it can be noticed that the diffusion coefficient is high in CSF (red colored areas), while it is lower and very similar for both GM and GM. As concerns the off diagonal elements, it is possible to observe that the diffusion coefficient can assume negative values. Voxels intensities are expressed in $\text{mm}^2 \text{day}^{-1}$.

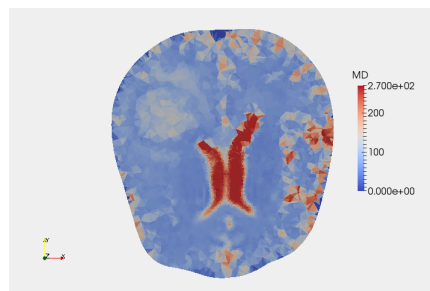


Figure 4.9: Mean diffusivity mapped on the computational mesh cut along the plane xy . We remind that the mean diffusivity is computed as $1/3\text{Tr}(\mathbf{D})$, it is an inverse measure of the tissue density and, thus, it is very similar for both grey matter and white matter and higher for CSF. Voxels intensities are expressed in $\text{mm}^2 \text{day}^{-1}$.

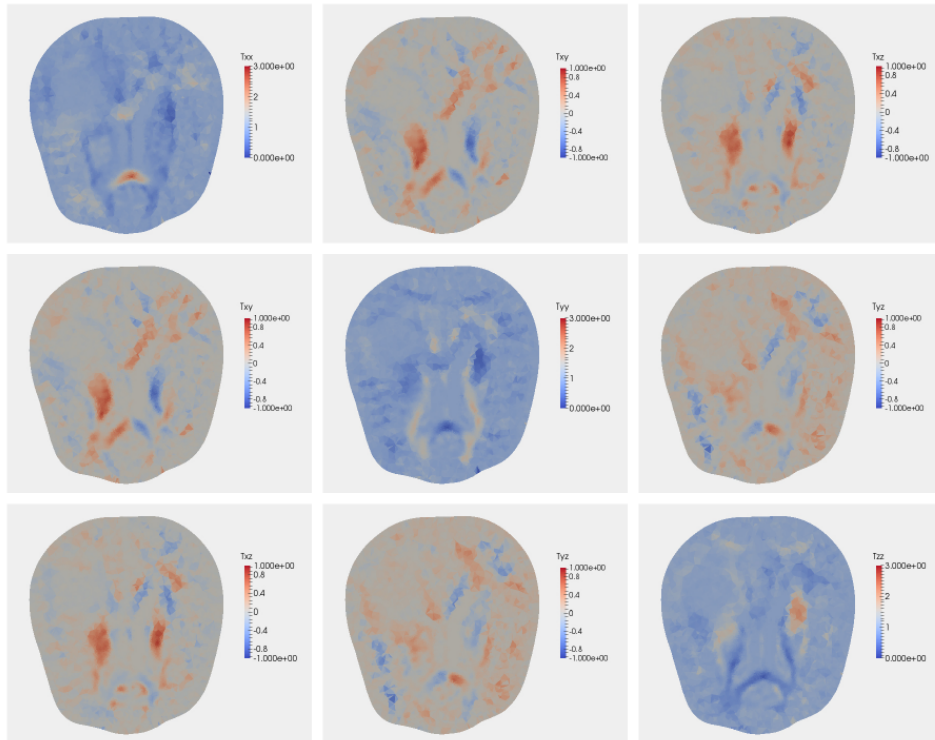


Figure 4.10: Patient-specific components of tensor \mathbf{T} depicted on the computational mesh cut along the plane xy . Comparing the images of the diagonal components of the tensor \mathbf{T} it is possible to observe the anisotropy of the white matter: for instance, x-axis seems to be the preferential direction in corpus callosum, e.g. T_{xx} is almost red in this area, while T_{yy} and T_{zz} are darker blue. In the brain areas occupied by grey matter and CSF, the components are almost similar and equal to one, e.g. the mesh is light blue coloured. Comparing the off diagonal elements of tensor \mathbf{T} , it is possible to notice that T_{ij} varies between -1 and 1 and, in particular, it is almost zero in isotropic areas.

4.3 Model implementation

4.3.1 Continuous weak formulation

We consider a bounded domain $\Omega \in \mathbb{R}^3$, representing the brain, and a time period $[0, T]$, $T < \infty$, representing the time interval in which the tumor is evolving. The aim is to determine the unknown fields $\phi(\mathbf{x}, t)$ and $n(\mathbf{x}, t)$ such that $\forall \mathbf{x} \in \Omega$ and $\forall t \in [0, T]$ the following equations are satisfied:

$$\frac{\partial \phi}{\partial t} - \nabla \cdot (\phi K(\phi) \nabla (f(\phi) - \epsilon^2 \Delta \phi)) - \nu \phi (n - \delta)(1 - \phi) + \nabla \cdot (k_n n_s \phi \mathbf{T} \nabla n) = 0 \quad (4.4)$$

$$\frac{\partial n}{\partial t} - \nabla \cdot (\mathbf{D} \nabla n) - S_n(1 - n) + \delta_n \phi n = 0. \quad (4.5)$$

where $K(\phi)$ and $f(\phi)$ are defined as in (3.37) and (3.39) respectively, the parameters are chosen on the basis of biological values found in literature, which have been reported in Table 3.1, and the tensor \mathbf{D} and the tensor \mathbf{T} have the form discussed in section 4.2.

In order to have a **well-posed** problem, it is necessary to impose initial conditions for ϕ and n , i.e. the cancer cell distribution and the nutrient distribution for $t = 0$. As mentioned, glioblastoma grows infiltratively and differs from many solid tumors because it is characterized by a smooth gradient of tumor cell density instead of presenting a sharp interface at the host/tumor boundary. Thus, it seems reasonable to hypothesize that $\phi(\mathbf{x}, 0) = \phi_0(\mathbf{x})$ follows a normal distribution in space: we suppose that it reaches a maximum value bigger than ϕ_e in the center of the tumor and decreases to zero, as shown in figure 4.11. Furthermore, we make the hypothesis that the brain area with $\phi_0(\mathbf{x}) < \epsilon_+$ represents the healthy tissue, where ϵ_+ is a threshold value that we set equals to 0.02. For numerical simulations described in Chapter 5 and in Chapter 6 section 1, we make the assumption that the initial tumor configuration has a spherical shape, as depicted in figures 4.12 and 4.13.

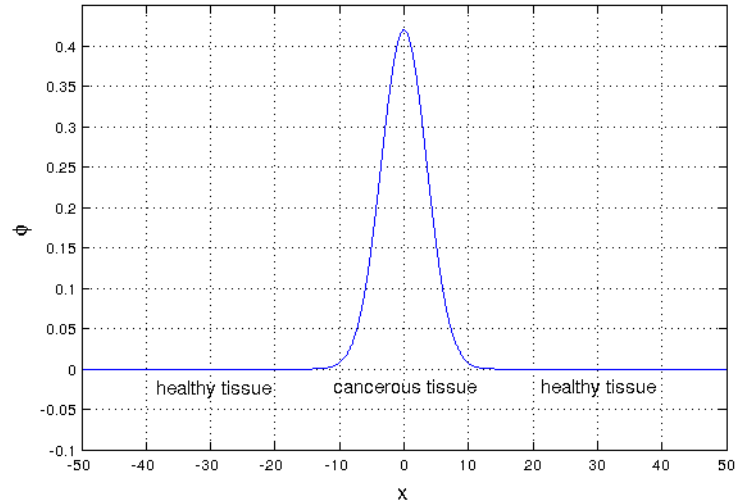
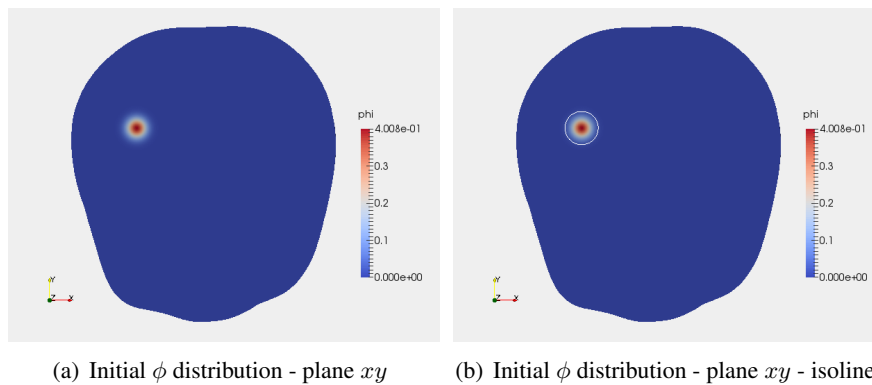


Figure 4.11: The cellular fraction follows a normal profile: it reaches a maximum value bigger than ϕ_e and decreases smoothly to zero. The brain tissue where $\phi_0(\mathbf{x}) < 0.02$ represents healthy tissue. The values of the x -axis are expressed in mm and $x = 0$ represents the center of the tumor.



(a) Initial ϕ distribution - plane xy

(b) Initial ϕ distribution - plane xy - isoline

Figure 4.12: Initial distribution of ϕ in the brain mesh, clipped mesh along the plane xy . Figure (a): as it is possible to notice, ϕ reaches its maximum value in the center of the tumor and decreases smoothly to zero. Figure (b): the threshold value $\epsilon = 0.02$ is specified by the isoline.

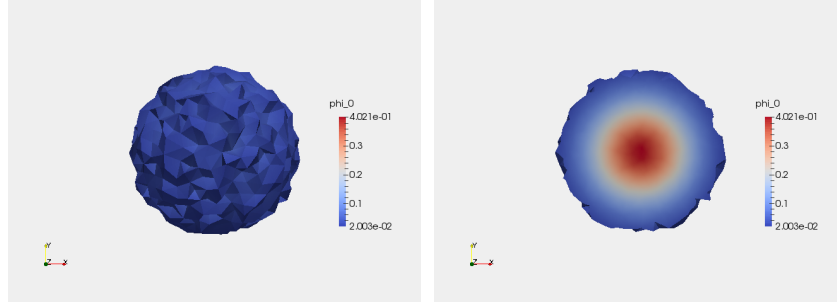
(a) Almost spherical shape of the tumor at $t = 0$ (b) Clipped tumor at $t = 0$

Figure 4.13: In the left figure, it is shown the initial tumor configuration obtained thresholding ϕ at 0.02. It presents almost a spherical shape. In the right figure, it is depicted the clipped tumor: it is possible to notice that the distribution of ϕ has its maximum in the center of the tumor and decreases getting closer to the boundaries.

Regarding the initial oxygen concentration $n(\mathbf{x}, 0) = n_0(\mathbf{x})$, we solve the steady version of the nutrient governing equation, i.e. $\forall \mathbf{x} \in \Omega$ we have to determine the unknown field $n_0(\mathbf{x})$ such that the following equation is satisfied:

$$\nabla \cdot (\mathbf{D}\nabla n_0) + S_n(1 - n_0) - \delta_n \phi_0 n_0 = 0. \quad (4.6)$$

where ϕ_0 is the initial cancerous distribution. As it is illustrated in figure 4.14, the oxygen concentration is equal to 1 outside the tumor area and decreases getting closer to the core of the glioblastoma, in accordance with the increase of ϕ_0 in this area.

In order to solve the problem, it is also mandatory to define boundary conditions for the governing equations. Since part of the boundary of the domain is represented by the cranial skull where the glioblastoma can not expand and for the fact that rarely brain tumors metastasize outside the brain, we impose a null Dirichlet condition and a null Neumann condition for the cell volume fraction at the boundary:

$$\forall t \in [0, T] \quad \phi = 0, \quad \text{on} \quad \partial\Omega, \quad (4.7)$$

$$\forall t \in [0, T] \quad \nabla \phi \cdot \hat{\mathbf{n}} = 0, \quad \text{on} \quad \partial\Omega, \quad (4.8)$$

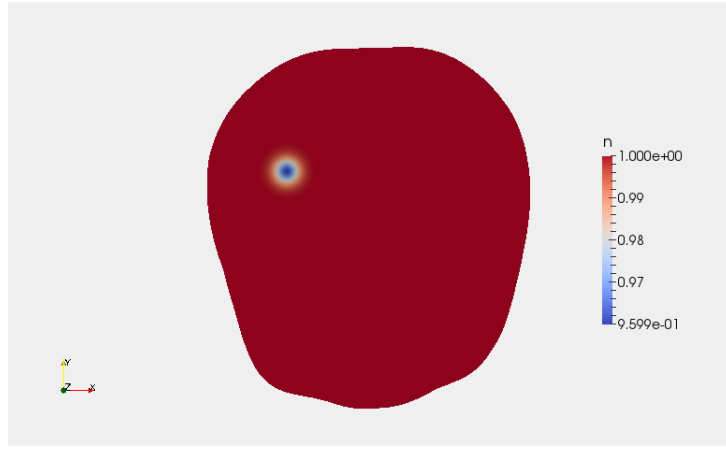


Figure 4.14: Initial distribution of n in the brain in a section along plane xy . As it is expected, the oxygen concentration decreases inside the glioblastoma, reaching the minimum value in the center of the tumor. Outside that area, the oxygen concentration is not affected by the presence of the tumor.

where $\hat{\mathbf{n}}$ is the outward boundary normal.

For the nutrients we choose the Dirichlet condition

$$\forall t \in [0, T] \quad n = 1, \quad \text{on} \quad \partial\Omega, \quad (4.9)$$

since we suppose that the brain boundary is far enough from the tumor location and consequently the oxygen concentration is maintained constant by the vasculature. Finally, as (4.4) is a fourth-order equation, it is useful to rephrase it as two coupled second-order equations, as follows:

$$\frac{\partial \phi}{\partial t} - \nabla \cdot (\phi K(\phi) \nabla \Sigma) - \nu \phi (n - \delta)(1 - \phi) + \nabla \cdot (k_n n_s \phi \mathbf{T} \nabla n) = 0 \quad (4.10)$$

$$\Sigma = f(\phi) - \epsilon^2 \Delta \phi. \quad (4.11)$$

In order to obtain the weak formulation of the model, we multiply each equation by a smooth test function taken from a specific functional space (that will be introduced later) and we integrate over the domain. Then, using the Green identity,

i.e. $\int_{\Omega} v \Delta u \, d\Omega = - \int_{\Omega} \nabla u \cdot \nabla v \, d\Omega + \int_{\partial\Omega} v \nabla u \cdot \hat{\mathbf{n}} \, dS$, we obtain:

$$\begin{aligned} & \int_{\Omega} \frac{\partial \phi}{\partial t} v \, d\Omega - \int_{\partial\Omega} v \phi K(\phi) \nabla \Sigma \cdot \hat{\mathbf{n}} \, dS + \int_{\Omega} \phi K(\phi) \nabla \Sigma \cdot \nabla v \, d\Omega + \\ & - \int_{\Omega} \nu \phi (n - \delta) (1 - \phi) v \, d\Omega + \int_{\partial\Omega} k_n n_s \mathbf{T} \phi \nabla n \cdot \hat{\mathbf{n}} v \, dS - \int_{\Omega} k_n n_s \mathbf{T} \phi \nabla n \cdot \nabla v \, d\Omega = 0, \end{aligned} \quad (4.12)$$

$$\int_{\Omega} \Sigma w \, d\Omega - \int_{\Omega} f(\phi) w \, d\Omega + \epsilon^2 \int_{\partial\Omega} w \nabla \phi \cdot \hat{\mathbf{n}} \, dS - \epsilon^2 \int_{\Omega} \nabla \phi \cdot \nabla w \, d\Omega = 0, \quad (4.13)$$

$$\begin{aligned} & \int_{\Omega} \frac{\partial n}{\partial t} q \, d\Omega - \int_{\partial\Omega} \mathbf{D} \nabla n \cdot \hat{\mathbf{n}} q \, dS + \int_{\Omega} \mathbf{D} \nabla n \cdot \nabla q \, d\Omega - \int_{\Omega} S_n (1 - n) q \, d\Omega + \\ & + \int_{\Omega} \delta_n \phi n q \, d\Omega = 0. \end{aligned} \quad (4.14)$$

For the functional spaces, we will choose v, w and q in $V = [H_0^1(\Omega)]^3$, where

$$H_0^1(\Omega) = \{v \in L^2(\Omega) \text{ with } \nabla v \in L^2(\Omega) : v = 0 \text{ on } \partial\Omega\} \quad (4.15)$$

We need to point out that for the equation (4.14) we are making an asymmetric choice for the functional spaces. In fact, for the nutrient concentration we impose a non homogenous Dirichlet condition and consequently we look for a solution $n(\mathbf{x}, \cdot)$ in $Q = [H^1(\Omega)]^3$, where

$$H^1(\Omega) = \{v \in L^2(\Omega) \text{ with } \nabla v \in L^2(\Omega)\}, \quad (4.16)$$

while the function test is taken in $[H_0^1(\Omega)]^3$. For a *good* weak formulation, we should substitute a new variable $\hat{n} = n - 1$ to n . In this way, the new variable satisfies a homogeneous Dirichlet condition and it can be taken in $[H_0^1(\Omega)]^3$, as the test function. Actually, as it will be explained in appendix A, the software we use to implement the governing equations naturally imposes Dirichlet conditions and the above issue doesn't have to be taken in consideration.

Therefore, with the choices (4.15), the weak statement of equations (4.4) and (4.5) reads:

find $\phi \in L^2([0, T]; [H^1(\Omega)]^3)$ and $n \in L^2([0, T]; [H^1(\Omega)]^3)$ with boundary and

initial conditions as discussed above, such that:

$$\begin{aligned} \int_{\Omega} \frac{\partial \phi}{\partial t} v \, d\Omega + \int_{\Omega} \phi K(\phi) \nabla \Sigma \cdot \nabla v \, d\Omega - \int_{\Omega} \nu \phi (n - \delta) (1 - \phi) v \, d\Omega \\ - \int_{\Omega} k_n n_s \mathbf{T} \phi \nabla n \cdot \nabla v \, d\Omega = 0, \quad \forall v \in V \end{aligned} \quad (4.17)$$

$$\int_{\Omega} \Sigma w \, d\Omega - \int_{\Omega} f(\phi) w \, d\Omega - \epsilon^2 \int_{\Omega} \nabla \phi \cdot \nabla w \, d\Omega = 0, \quad \forall w \in V \quad (4.18)$$

$$\begin{aligned} \int_{\Omega} \frac{\partial n}{\partial t} q \, d\Omega + \int_{\Omega} \mathbf{D} \nabla n \cdot \nabla q \, d\Omega - \int_{\Omega} S_n (1 - n) q \, d\Omega \\ + \int_{\Omega} \delta_n \phi n q \, d\Omega = 0, \quad \forall q \in V. \end{aligned} \quad (4.19)$$

4.3.2 Numerical model

To solve the model numerically, we need to transform the continuous variational problem (4.17), (4.18), (4.19) into a discrete variational problem. First of all, we proceed performing a spatial discretization with finite element. We use linear tetrahedron (P_1) elements to discretize the problem. Consequently, the semidiscrete variational problem is :

$\forall t \in [0, T]$, find $\phi_h = \phi_h(t) \in V_h \subset V$ and $n_h = n_h(t) \in Q_h \subset Q$ such that:

$$\begin{aligned} \int_{\Omega} \frac{\partial \phi_h}{\partial t} v_h \, d\Omega + \int_{\Omega} \phi_h K(\phi_h) \nabla \Sigma_h \cdot \nabla v_h \, d\Omega - \int_{\Omega} \nu \phi_h (n_h - \delta) (1 - \phi_h) v_h \, d\Omega \\ - \int_{\Omega} k_n n_s \mathbf{T} \phi_h \nabla n_h \cdot \nabla v_h \, d\Omega = 0, \quad \forall v_h \in V_h \end{aligned} \quad (4.20)$$

$$\int_{\Omega} \Sigma_h w_h \, d\Omega - \int_{\Omega} f(\phi_h) w_h \, d\Omega - \epsilon^2 \int_{\Omega} \nabla \phi_h \cdot \nabla w_h \, d\Omega = 0, \quad \forall w_h \in V_h \quad (4.21)$$

$$\begin{aligned} \int_{\Omega} \frac{\partial n_h}{\partial t} q_h \, d\Omega + \int_{\Omega} \mathbf{D} \nabla n_h \cdot \nabla q_h \, d\Omega - \int_{\Omega} S_n (1 - n_h) q_h \, d\Omega \\ + \int_{\Omega} \delta_n \phi_h n_h q \, d\Omega = 0, \quad \forall q_h \in V_h. \end{aligned} \quad (4.22)$$

with ϕ_h^0 and n_h^0 the discrete initial conditions.

For the time discretization, we use the second-order accurate Crank-Nicholson algorithm. Given N time steps, we set a time interval $\Delta t = \frac{T}{N}$ such that $\forall t \in [0, T]$ it exists $u^n = u|_{t=n\Delta t}$ with $n = 0, \dots, N$ and $u = \phi, \Sigma, n$. If we call

$$u^* = u^{n+\frac{1}{2}} = \frac{1}{2} u^{n+1} + \frac{1}{2} u^n \quad \text{with} \quad u = \phi, \Sigma, n \quad (4.23)$$

the discrete variational problem can be written as:

given ϕ_h^n and n_h^n , find $\phi_h^{n+1} \in V_h$ and $n_h^{n+1} \in Q_h \forall n = 0..N$ such that:

$$\begin{aligned} & \int_{\Omega} \phi_h^{n+1} v_h \, d\Omega - \int_{\Omega} \phi_h^n v_h \, d\Omega + \Delta t \int_{\Omega} \phi_h^* K(\phi_h^*) \nabla \Sigma_h^* \cdot \nabla v_h \, d\Omega \\ & - \Delta t \int_{\Omega} \nu \phi_h^* (n_h^* - \delta)(1 - \phi_h^*) v_h \, d\Omega - \Delta t \int_{\Omega} k_n n_s \mathbf{T} \phi_h^* \nabla n_h^* \cdot \nabla v_h \, d\Omega = 0, \quad \forall v_h \in V_h \end{aligned} \quad (4.24)$$

$$\int_{\Omega} \Sigma_h^{n+1} w_h \, d\Omega - \int_{\Omega} f(\phi_h^{n+1}) w_h \, d\Omega - \epsilon^2 \int_{\Omega} \nabla \phi_h^{n+1} \cdot \nabla w_h \, d\Omega = 0, \quad \forall w_h \in V_h \quad (4.25)$$

$$\begin{aligned} & \int_{\Omega} n_h^{n+1} q_h \, d\Omega - \int_{\Omega} n_h^n q_h \, d\Omega + \Delta t \int_{\Omega} \mathbf{D} \nabla n_h^* \cdot \nabla q_h \, d\Omega - \Delta t \int_{\Omega} S_n (1 - n_h^*) q_h \, d\Omega \\ & + \Delta t \int_{\Omega} \delta_n \phi_h^* n_h^* q_h \, d\Omega = 0, \quad \forall q_h \in V_h. \end{aligned} \quad (4.26)$$

Once the discrete weak statement is obtained, we are able to perform numerical simulation on the brain mesh. We make use of an open source software called the *FEniCS project* which finds in Python its natural programming language. In relation to our aims, one of the main advantage of using *FEniCS* as computational resource is that it offers an automatic approach to nonlinear variational problem. So, we can use the built-in classes and solve the nonlinear problem in few lines of code. In appendix A.2 we illustrate more deeply the *FEniCS* project and we include the Python codes we have implemented to solve the problem with some comments.

Chapter 5

Sensitivity Analysis

In the present chapter we investigate how biological parameters influence tumor and nutrients behavior. In particular, the analysis is driven by the necessity of understanding which among them play a fundamental role in the anisotropic diffusion of nutrients and the anisotropic growth of the tumor. Thus, in the first section we perform the adimensionalization of the homogenous (in term of diffusion) and anisotropic (in term of preferential directions) mathematical model introduced in Chapter 3 in order to recognize which are the parameters that should be considered in the analysis. We identify two pairs of parameters on which we perform the tests, described in sections 5.2.1 and 5.2.2. In those sections, the relative outputs are given. Finally we make some considerations in order to figure out what is the behavior of the tumor in relation to the values of the parameters.

5.1 Preparing the test cases

In this section, we provide the dimensionless form of equations of the mathematical model described in Chapter 3 and we analyze the role of biological parameters in the governing equations. We choose to perform the sensitivity analysis on the parameters using a model that does not take into account the inhomogeneity of diffusion in the tissue. In this way, it will be easier to understand and study the

effects due to the introduction of an anisotropic tensor \mathbf{T} . Thus, we use the relation $\mathbf{D} = D_n \mathbf{T}$, where D_n is the typical oxygen diffusion coefficient introduced in section 3.3, and the model to adimensionalize results in:

$$\frac{\partial \phi}{\partial t} = \nabla \cdot \left(\frac{\phi(1-\phi)^2}{M} \nabla (f(\phi) - \epsilon^2 \Delta \phi) \right) + \nu \phi (n - \delta)(1 - \phi) - \nabla \cdot (k_n \mathbf{T} \phi n_s \nabla n) \quad (5.1)$$

$$\frac{\partial n}{\partial t} = D_n \mathbf{T} \Delta n + S_n(1 - n) - \delta_n \phi n. \quad (5.2)$$

We define

$$\hat{x} = \frac{x}{l_n} \quad \text{and} \quad \hat{t} = t\nu \quad (5.3)$$

the adimensional space and time variables, where l_n is the characteristic length of oxygen diffusion and ν is the characteristic cell proliferation rate, as discussed in section 3.3, and the adimensional quantities

$$\hat{f} = \frac{f}{\chi} \quad \text{and} \quad \hat{\epsilon}^2 = \frac{\epsilon^2}{\chi l_n^2}. \quad (5.4)$$

Substituting (5.3) and (5.4) in (5.1) and (5.2) and rearranging the terms, we have that the model reads

$$\frac{\partial \phi}{\partial \hat{t}} = \frac{\chi}{\nu l_n^2 M} \hat{\nabla} \cdot \left(\phi(1-\phi)^2 \hat{\nabla} \hat{\Sigma} \right) + \phi(n - \delta)(1 - \phi) - \frac{k_n n_s}{l_n^2 \nu} \hat{\nabla} \cdot \left(\phi \mathbf{T} \hat{\nabla} n \right) \quad (5.5)$$

$$\hat{\Sigma} = \hat{f} - \hat{\epsilon}^2 \hat{\Delta} \phi \quad (5.6)$$

$$\frac{\partial n}{\partial \hat{t}} = \frac{D_n}{l_n^2 \nu} \cdot \left(\mathbf{T} \hat{\Delta} n \right) + \frac{S_n}{\nu} (1 - n) - \frac{\delta_n}{\nu} \phi n. \quad (5.7)$$

In equation (5.5), we call

$$D = \frac{\chi}{l_n^2 M \nu} \quad \text{and} \quad K = \frac{k_n n_s}{l_n^2 \nu}.$$

Then dropping the hat and reminding that the relation $l_n = \sqrt{D_n/\delta_n}$ holds, we obtain the following dimensionless form of the model:

$$\frac{\partial \phi}{\partial t} = D \nabla \cdot (\phi(1-\phi)^2 \nabla \Sigma) + \phi(n-\delta)(1-\phi) - K \nabla \cdot (\phi \mathbf{T} \nabla n) \quad (5.8)$$

$$\Sigma = f(\phi) - \epsilon^2 \Delta \phi \quad (5.9)$$

$$\frac{\partial n}{\partial t} = \frac{\delta_n}{\nu} (\mathbf{T} \Delta n) + \frac{S_n}{\nu} (1-n) - \frac{\delta_n}{\nu} \phi n. \quad (5.10)$$

As we see, the first coefficient D is responsible of the *isotropic diffusion* and depends on χ and M , while K is the coefficient responsible of the *anisotropic diffusion* and relies mostly on the chemotactic coefficient k_n . Consequently, to study the behavior of the cellular fraction in term of anisotropic growth it is sufficient to simulate test cases in which M and k_n assume different values. This is done in subsection 5.2.1. In equation (5.7), the characteristic parameters are S_n and δ_n , which govern nutrients production and uptake respectively. In particular, their relationship is responsible of oxygen availability in tissues and consequently it determines tumor development, since chemotactic flux depends on nutrients gradient. In subsection 5.2.2 we provide test cases in which we analyze glioblastoma growth with respect to S_n and δ_n .

Once we have identified the biological parameters to consider, we perform the numerical tests.

The model we use, though, is only time dimensionless. In fact, we deal with a real geometry (a patient's brain) and space adimensionalization would be meaningless, whereas time adimensionalization is required, because in this way we are able to provide the analysis without being influenced by cell proliferation rate ν . Substituting the non dimensional quantity \hat{t} , governing equations are:

$$\frac{\partial \phi}{\partial \hat{t}} = \nabla \cdot \left(\phi \frac{(1-\phi)^2}{M\nu} \nabla \Sigma \right) + \phi(n-\delta)(1-\phi) - \nabla \cdot \frac{k_n}{\nu} (\phi \mathbf{T} \nabla n) \quad (5.11)$$

$$\Sigma = f(\phi) - \epsilon^2 \Delta \phi \quad (5.12)$$

$$\frac{\partial n}{\partial \hat{t}} = \frac{D_n}{\nu} \mathbf{T} \Delta n + \frac{S_n}{\nu} (1-n) - \frac{\delta_n}{\nu} \phi n. \quad (5.13)$$

For sake of simplicity, we choose $\nu = 1 \text{ day}^{-1}$.

About the tests, we use numerical codes described in appendix A.2. We perform very simple simulations, without introducing real DTI data as discussed in section 4.2, but only assuming as a test case the tensor

$$\mathbf{T} = \begin{pmatrix} 3 & 0 & 0 \\ 0 & 0 & 0 \\ 0 & 0 & 0 \end{pmatrix}$$

which imposes as preferential direction for oxygen diffusion and cell chemotaxis the x axis. Moreover, we hypothesize that the tumor is located in the center of the brain and it is initially spherical at the time of diagnosis, that in the model corresponds to $t = 0$. Thus, the initial configuration of ϕ for is represented by a normally distributed cellular fraction concentration, as depicted in figures 5.1 and 5.2. We will compare each of the test cases paying attention to:

- profile and maximum value reached by ϕ at the end of the test;
- anisotropy of the tumor shape, as exemplified in figure 5.3;
- tumor volume at the end of simulation;
- nutrients profile at $t = 0$ and at the end of the simulation.

In order to facilitate the comparison, only for these sensitivity tests, we set a threshold for the tumoral area at $\epsilon_+ = 0.1$. The isoline is depicted in figure 5.2.

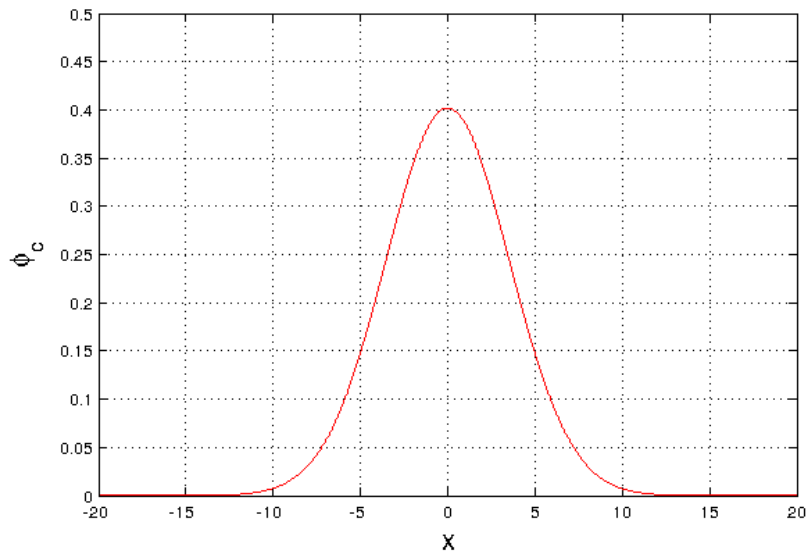


Figure 5.1: Initial profile of the cancerous volume fraction in function of the distance from the center of the tumor. We hypothesize that it follows a normal distribution with its maximum in $\phi > \phi_e$.

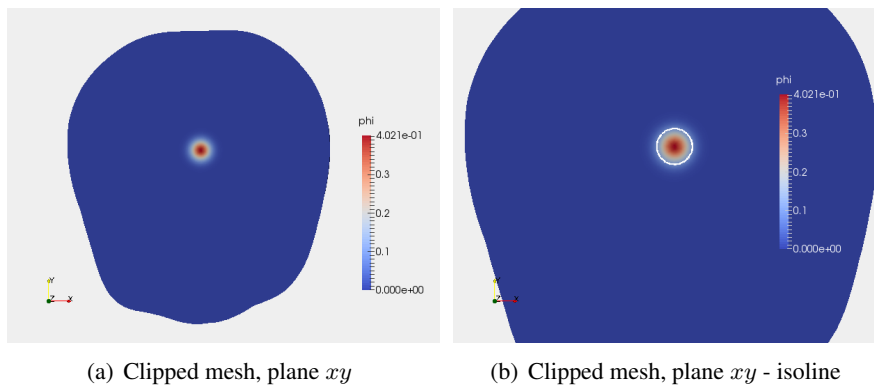


Figure 5.2: Initial concentration of ϕ in the brain at the time of diagnosis on the clipped mesh cut along the plane xy . Figure (b): detail of the isoline $\phi = 0.1$, value at which we compare tumor dimension.

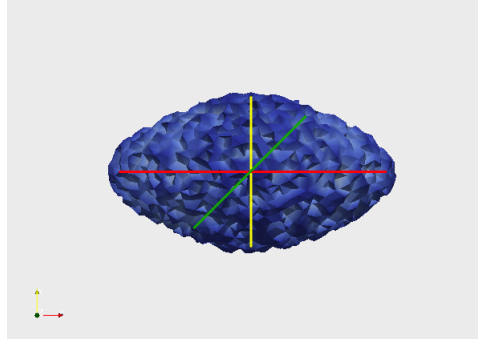


Figure 5.3: To understand how much some biological parameters weight on ϕ and n , we pay attention to tumor shape: the red line represents the tumor dimension along x-axis which we call in the following Δx , the yellow line represents Δy and the green line Δz .

5.2 Sensitivity analysis

5.2.1 Cellular evolution: parameters M and k_n

In this part of the chapter, we investigate the effects of the interphase friction parameter and the chemotactic parameter on the tumor development. We have performed 16 simulations, considering the combined effects of four different values of M and four different values of k_n . Since in literature M is estimated to be between $1377.9 \text{ mm}^{-2}\text{Pa}$ and $4286.7 \text{ mm}^{-2} \text{ Pa}$, we have chosen four values with different orders of magnitude as test values, considering also limit situations in which the parameters are out the range reported in literature: $M= 100 \text{ mm}^{-2}\text{Pa}$, $M= 1000 \text{ mm}^{-2}\text{Pa}$, $M = 5000 \text{ mm}^{-2}\text{Pa}$ and $M = 10000 \text{ mm}^{-2}\text{Pa}$. On the other hand, the chemotactic parameter is estimated to be equal to $1296 \text{ mm}^2 \text{ mM}^{-1} \text{ day}^{-1}$, value that have been discovered studying bacteria's behavior in an environment rich of glucose. Thus, because literature is poor about chemotaxis of glioma cells, we suppose that the chemotactic response of glial cells to nutrients is lower than that of the bacteria. Also in this case, we have chosen values with different orders of magnitude: $k_n = 1 \text{ mm}^2 \text{ mM}^{-1} \text{ day}^{-1}$, $k_n = 100 \text{ mm}^2 \text{ mM}^{-1} \text{ day}^{-1}$, $k_n = 500 \text{ mm}^2 \text{ mM}^{-1} \text{ day}^{-1}$ and $k_n = 1000 \text{ mm}^2 \text{ mM}^{-1} \text{ day}^{-1}$.

The other biological parameters set in the simulations are reported in table 5.1.

$\chi = 900 \text{ Pa}$	$E = 694 \text{ Pa}$	$\delta_n = 1000 \text{ day}^{-1}$
$c_e = 0.389$	$\delta = 0.3$	$S_n = 10^4 \text{ day}^{-1}$
$D_n = 86.4 \text{ mm}^2\text{day}^{-1}$	$n_s = 0.07 \text{ mM}$	

Table 5.1: Biological parameters - analysis I

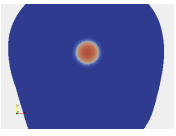
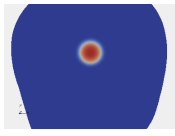
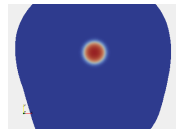
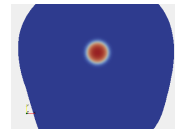
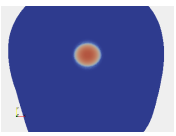
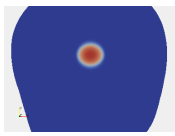
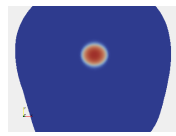
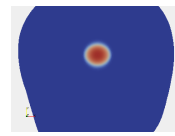
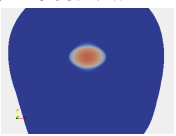
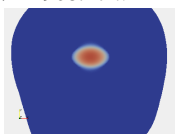
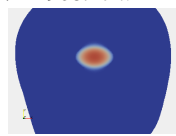
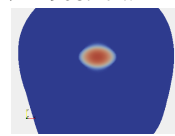
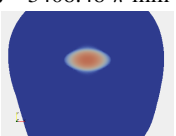
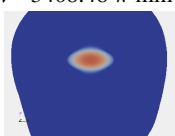
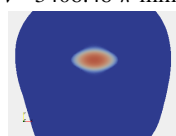
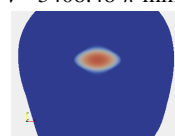
As earlier explained, we have performed simply simulations, starting from a spherical tumor located in the center of the brain and setting the x -axis as the preferential direction of nutrient diffusion and cell chemotaxis. We analyze the numerical result at the 60th iteration, that means 6 days after the diagnosis. In table 5.3, we record ϕ_{max} , tumor dimension Δx , Δy , Δz , tumor volume and the image of the clipped mesh along the plane xy . The results are then discussed in section 5.3.

5.2.2 Nutrient evolution: parameters δ_n and S_n

In this section, we compare the tissue transfer rate of nutrients S_n and the oxygen consumption rate of tumor cells δ_n in order to figure out how nutrients availability weights on tumor development. In literature S_n is estimated to be equal to 10^4 day^{-1} and consequently we choose three values with different orders of magnitude as test cases: $S_n = 10^3 \text{ day}^{-1}$, $S_n = 10^4 \text{ day}^{-1}$, $S_n = 10^5 \text{ day}^{-1}$. For δ_n , we have found a value of 8640 day^{-1} in literature. Thus, we use as test values $\delta_n = 1000 \text{ day}^{-1}$, $\delta_n = 4000 \text{ day}^{-1}$, $\delta_n = 8000 \text{ day}^{-1}$. Regarding the other biological parameters, we use the values reported in table 5.2, while for the numerical framework, we follow the the guidelines described previously. In table 5.4, we report the results of the test cases, at iteration 90, i.e. 9 days after the diagnosis. The results are then discussed in section 5.3.

$\chi = 900 \text{ Pa}$	$E = 694 \text{ Pa}$	$k_n = 100\text{mm}^2 \text{ mM}^{-1} \text{ day}^{-1}$
$c_e = 0.389$	$\delta = 0.3$	$M = 5000 \text{ mm}^{-2}\text{Pa}$
$D_n = 86.4 \text{ mm}^2\text{day}^{-1}$	$n_s = 0.07 \text{ mM}$	

Table 5.2: Biological parameters - Sensitivity analysis II

	M = 100	M = 1000	M = 5000	M = 10000
$k_n = 1$	$\phi_{max} = 0.862$ $\Delta x = 22.7$ mm $\Delta y = 23.1$ mm $\Delta z = 23$ mm $V = 2010.08 \pi$ mm ³ 	$\phi_{max} = 0.949$ $\Delta x = 23.1$ mm $\Delta y = 23.1$ mm $\Delta z = 23$ mm $V = 2036.65 \pi$ mm ³ 	$\phi_{max} = 0.962$ $\Delta x = 23.1$ mm $\Delta y = 23.1$ mm $\Delta z = 23$ mm $V = 2036.65 \pi$ mm ³ 	$\phi_{max} = 0.964$ $\Delta x = 23.1$ mm $\Delta y = 23.1$ mm $\Delta z = 23$ mm $V = 2036.65 \pi$ mm ³ 
$k_n = 100$	$\phi_{max} = 0.847$ $\Delta x = 24.4$ mm $\Delta y = 23.3$ mm $\Delta z = 22.9$ mm $V = 2169.72 \pi$ mm ³ 	$\phi_{max} = 0.925$ $\Delta x = 24.4$ mm $\Delta y = 23.1$ mm $\Delta z = 23$ mm $V = 2160.62 \pi$ mm ³ 	$\phi_{max} = 0.936$ $\Delta x = 24.4$ mm $\Delta y = 23.1$ mm $\Delta z = 23$ mm $V = 2160.62 \pi$ mm ³ 	$\phi_{max} = 0.938$ $\Delta x = 24.4$ mm $\Delta y = 23.1$ mm $\Delta z = 23$ mm $V = 2160.62 \pi$ mm ³ 
$k_n = 500$	$\phi_{max} = 0.808$ $\Delta x = 32.7$ mm $\Delta y = 23.1$ mm $\Delta z = 22.9$ mm $V = 2908.17 \pi$ mm ³ 	$\phi_{max} = 0.869$ $\Delta x = 32.7$ mm $\Delta y = 23.1$ mm $\Delta z = 22.9$ mm $V = 2908.17 \pi$ mm ³ 	$\phi_{max} = 0.877$ $\Delta x = 32.7$ mm $\Delta y = 23.1$ mm $\Delta z = 22.9$ mm $V = 2908.17 \pi$ mm ³ 	$\phi_{max} = 0.878$ $\Delta x = 32.7$ mm $\Delta y = 23.1$ mm $\Delta z = 22.9$ mm $V = 2908.17 \pi$ mm ³ 
$k_n = 1000$	$\phi_{max} = 0.779$ $\Delta x = 40.4$ mm $\Delta y = 22.3$ mm $\Delta z = 22.7$ mm $V = 3408.48 \pi$ mm ³ 	$\phi_{max} = 0.832$ $\Delta x = 40.4$ mm $\Delta y = 22.9$ mm $\Delta z = 22.9$ mm $V = 3408.48 \pi$ mm ³ 	$\phi_{max} = 0.839$ $\Delta x = 40.4$ mm $\Delta y = 22.9$ mm $\Delta z = 22.9$ mm $V = 3408.48 \pi$ mm ³ 	$\phi_{max} = 0.840$ $\Delta x = 40.4$ mm $\Delta y = 22.9$ mm $\Delta z = 22.9$ mm $V = 3408.48 \pi$ mm ³ 

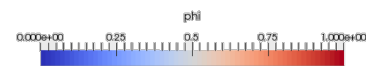


Table 5.3: Numerical results at the iteration 60. In the table, values of M are expressed in mm⁻²Pa, while values of k_n are given in mm² mM⁻¹ day⁻¹. In order to compare the test cases, we record ϕ_{max} , tumor dimension, that is Δx , Δy , Δz and the tumor volume.

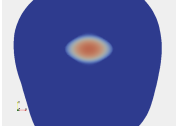

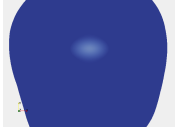
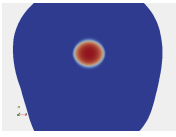
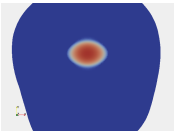
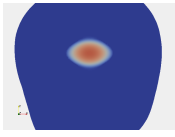
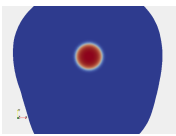
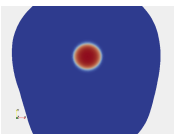
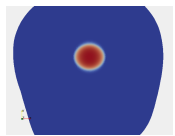
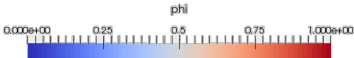
	$\delta_n = 1000$	$\delta_n = 4000$	$\delta_n = 8000$
$S_n = 10^3$	$\phi_{max} = 0.790$ $\Delta x = 43.2$ mm $\Delta y = 26.9$ mm $\Delta z = 26.7$ mm $V = 5171.25 \pi \text{mm}^3$ 	ϕ decreases iteration 70 	ϕ decreases iteration 30 
$S_n = 10^4$	$\phi_{max} = 0.983$ $\Delta x = 29.8$ mm $\Delta y = 27.5$ mm $\Delta z = 27.3$ mm $V = 3728.72 \pi \text{mm}^3$ 	$\phi_{max} = 0.920$ $\Delta x = 37.1$ mm $\Delta y = 27.1$ mm $\Delta z = 27.2$ mm $V = 4557.85 \pi \text{mm}^3$ 	$\phi_{max} = 0.835$ $\Delta x = 42.3$ mm $\Delta y = 26.9$ mm $\Delta z = 26.8$ mm $V = 5082.48 \pi \text{mm}^3$ 
$S_n = 10^5$	$\phi_{max} = 0.995$ $\Delta x = 27.6$ mm $\Delta y = 27.5$ mm $\Delta z = 27.3$ mm $V = 3453.45 \pi \text{mm}^3$ 	$\phi_{max} = 0.992$ $\Delta x = 27.7$ mm $\Delta y = 27.5$ mm $\Delta z = 27.3$ mm $V = 3465.96 \pi \text{mm}^3$ 	$\phi_{max} = 0.987$ $\Delta x = 29$ mm $\Delta y = 27.5$ mm $\Delta z = 27.3$ mm $V = 3628.62 \pi \text{mm}^3$ 
			

Table 5.4: Numerical results at iteration 90. In the table, values of δ_n and S_n are expressed in day^{-1} . In order to compare the test cases, we record ϕ_{max} , tumor dimension, that is Δx , Δy , Δz and the tumor volume. An image of the tumor region on the clipped mesh along plane xy is provided for each test case. As we see, for test cases with $S_n = 10^3$ and $\delta_n = 4000$ and $\delta_n = 8000$, the cellular fraction decreases. This means that nutrients production is not enough to supply cells nourishment and consequently the cells scatter and the tumor disappears. Of course, this situation is biologically impossible. For these tests, we provide an image of the tumor region 7 days after the diagnosis for the former and 3 days after the diagnosis for the latter.

5.3 Observations and conclusions

We start commenting on the results of section 5.2.1. Observing tumor data recorded in table 5.3, we can say that if M increases, the maximum volume fraction ϕ_{max} recorded at the given time step increases too. In fact with bigger values of M , the isotropic diffusion decreases and thus, cancerous cells tend to accumulate. Moreover, looking at one of the four rows of the table, it is possible to notice that tumor dimension does not change in relation to the increasing of M . Consequently, the value given to M does not influence the tumor extension at the given time step. We now pay attention to tumor/host interface: observing table 5.5 we assert that for increasing values of M , the interface host/tumor gets sharper. This fact is claimed in literature too. In [83], it is claimed that the value of ϵ determines the sharpness of the interface host/tumor, e.g. for smaller ϵ , the interface becomes smoother. Regarding our model, the term in ϵ is multiplied by the reciprocal of M and thus, for bigger M , the ϵ term decreases.

We concentrate now on the role of k_n in the development of the tumor. Examining the results of table 5.3, it is possible to notice that, for k_n equal to one, the tumor is almost spherical, while, for bigger values of the chemotactic parameter, it assumes an ellipsoidal configuration. This fact happens because the tensor \mathbf{T} is weighted by the term k_n and then, an enlargement of k_n has the effect of intensify the movement of the cells along that preferential direction (the x-axis is these cases). Then, it also happens that, for increasing value of k_n , the maximum value ϕ_{max} reached at the given time step decreases due to the scattering of the tumoral cells forced by higher chemotaxis, while the total volume occupied by the tumor increases. For concluding, the interface tumor/host gets smoother for increasing value of k_n as the cells have more freedom to move, as illustrated in table 5.5.

Concerning the results collected in table 5.4, first of all, we observe that if the value of the nutrient supply S_n is not as high as cells need for sustaining proliferation, the cellular fraction ϕ decreases and the tumor tends to disappear. In fact, S_n is the parameter that regulates nutrients supply from blood vessels to tumor cells and, if

its value is not high enough to fulfill nutrients consumption, the tumor is not able to expand as the proliferation is limited by nutrients availability. Furthermore, of course, if the values of S_n grow, then the maximum value ϕ_{max} reached by ϕ at the given time step increases while the volume occupied by the tumor decreases. On the other hand, for the same the value of S_n but for increasing values of δ_n , ϕ_{max} decreases but the volume increases. To explain the behavior of the volume, we have to pay attention to the anisotropic configuration assumed by the tumor. It happens that for a high value of S_n the tumor is almost isotropic and some slight anisotropy is recorded only for increasing δ_n . It seems that the relation between S_n and δ_n influences not only the availability of nutrients in the environment and, in consequence, cell proliferation, but it affects also the term ∇n and thus the chemotactic motion of cells. As a matter of fact, that relationship determines the value of $n_{0,min}$, the minimum value reached by nutrient concentration at $t = 0$, and then the gradient of n : for the same value of δ_n , it happens that $n_{0,min}$ increases with the increases of S_n and thus ∇n decreases. On the other hand, for the same value of S_n , $n_{0,min}$ decreases with the increase of δ_n and consequently ∇n increases. It follows that the anisotropic growth along the x-axis is bigger for lower values of S_n and higher values of δ_n . Regarding the test cases in which ϕ decreases, it could also happen that, besides the low cells proliferation, ∇n is so big that chemotaxis avoids cells to accumulate. The profiles of n_0 for each of the test cases are summarized in table 5.6. Finally, in table 5.7, the profiles of ϕ and n at the 90th iteration are depicted. Profiles are obtained as described in picture 5.4.

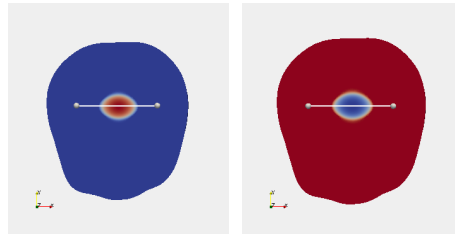


Figure 5.4: In the figure it is explained how ϕ and n profiles are obtained in tables 5.5 and 5.7. We plot the variables over the white line depicted, which is aligned with the x axis and crosses the tumor in the midline of the z axis.

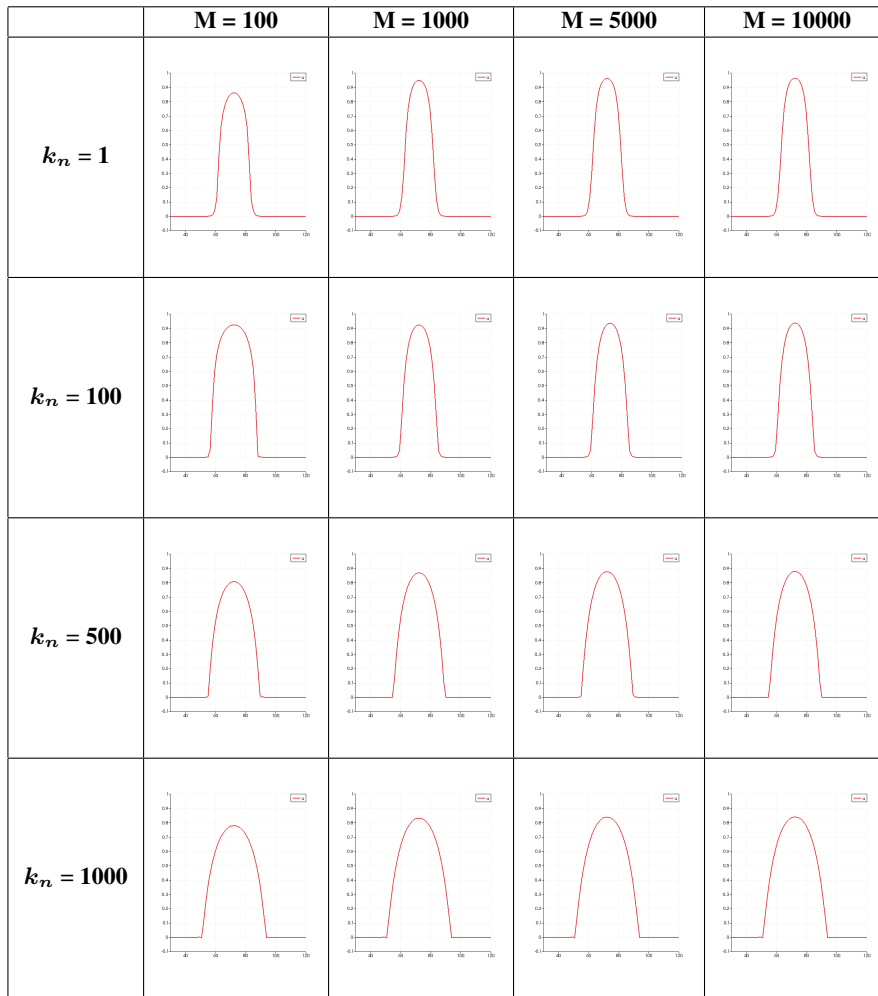


Table 5.5: Profile of the cellular fraction ϕ at iteration 60. Values of M increase horizontally and are expressed in mm^{-2}Pa , while values of k_n grows vertically and are given in $\text{mm}^2 \text{mM}^{-1} \text{day}^{-1}$. Examining the profiles, we claim that for increasing values of M and for decreasing values of k_n the interface host/tumor gets sharper. Profiles are obtained as described in picture 5.4.

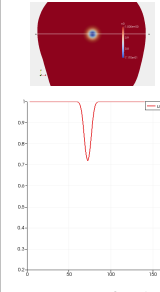
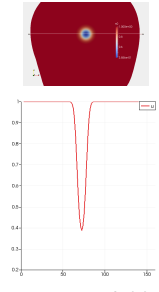
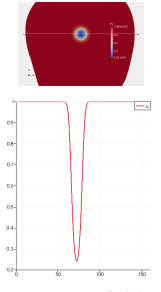
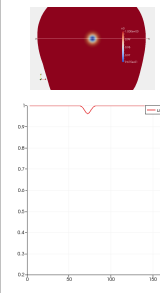
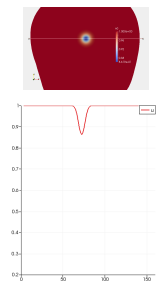
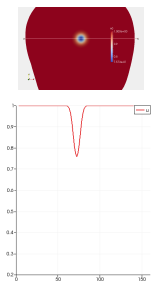
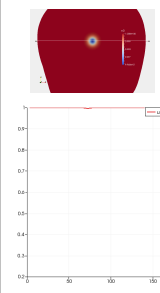
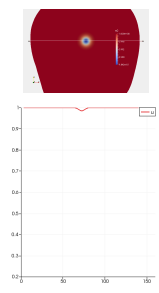
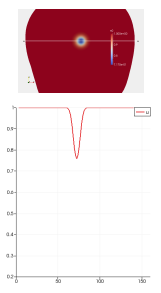
	$\delta_n = 1000$	$\delta_n = 4000$	$\delta_n = 8000$
$S_n = 10^3$	 $n_{0,min} = 0.717$	 $n_{0,min} = 0.38$	 $n_{0,min} = 0.23$
$S_n = 10^4$	 $n_{0,min} = 0.961$	 $n_{0,min} = 0.861$	 $n_{0,min} = 0.756$
$S_n = 10^5$	 $n_{0,min} = 0.995$	 $n_{0,min} = 0.984$	 $n_{0,min} = 0.984$

Table 5.6: In the table, we are comparing the profile of n at $t = 0$ for each of the test cases. The values of S_n increases vertically, while the values of δ_n grows horizontally. Both are expressed in day^{-1} . For increasing values of δ_n , $n_{0,min}$ decreases and consequently the gradient of n becomes higher, while for growing values of S_n , $n_{0,min}$ gets closer to 1 and the gradient of n decreases.

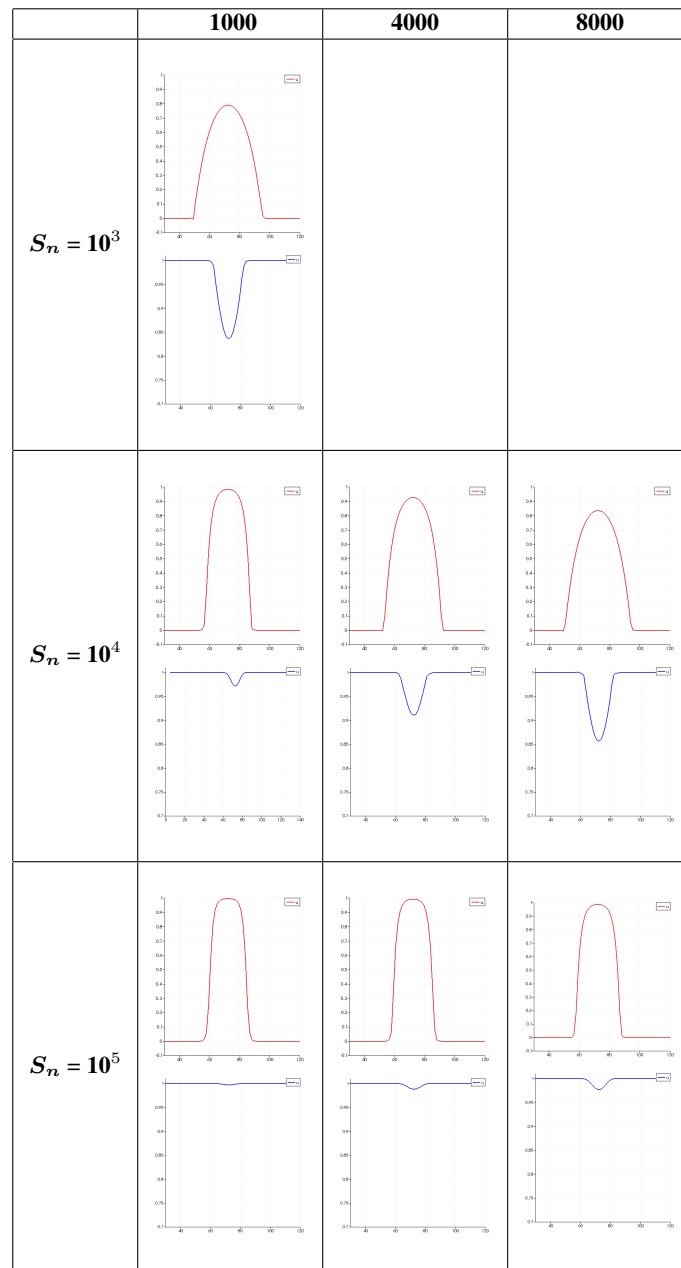


Table 5.7: Profile of the cellular fraction ϕ (above plot, red line) and of the oxygen concentration n (below plot, blue line) at iteration 90. Values of δ_n increase horizontally, while values of S_n grows vertically. Both are expressed in day^{-1} . Profiles are obtained as described in picture 5.4.

Chapter 6

Numerical Tests

In this chapter, we present and discuss two medical-relevant tests performed with the model proposed in Chapter 3.

In the first test, introduced in section 6.1, we investigate the development of a butterfly glioblastoma, a type of GBM that arises in the corpus callosum (CC) and spreads symmetrically in the hemispheres imitating butterfly wings. As it will be discussed, the CC is a bundle of white matter fibers which connects the two sides of the brain and it is an area characterized by high anisotropy. For these reasons, beyond of the medical interest, this simulation is important for its mathematical implications too. In fact, it is a good way to evaluate the anisotropic heterogeneous model, studying the tumor shape and the preferential direction of oxygen diffusion and cell motion due to the presence of patient-specific tensors \mathbf{T} and \mathbf{D} . In the second section, we describe and simulate the common medical situation in which a partial surgical resection is performed and some cancerous cells are left behind. We investigate the development and the diffusion of the survival cells. This test has a huge medical interest, since treating gliomas a complete resection is not practicable: these tumors, indeed, penetrate too deeply into white matter fibers and, in many situations, removing all the diseased cells is impossible.

6.1 Simulating butterfly glioma

Butterfly glioma is the name given to a glioblastoma which crosses the corpus callosum and grows symmetrically in the two hemispheres, simulating butterfly wings. Corpus callosum is the largest collection of white matter within the brain, formed by over 200 million axons, which is approximately 10 cm in length, C-shaped and located above the thalamus, under the cortex and in the middle of the two hemispheres (figure 6.1). It has the function of connecting the two sides of the brain and to facilitates communication thanks to its high myelin content. Not uncommonly glioblastoma arises in this area, more frequently in the frontal lobes, crossing via the genu of the corpus callosum, as depicted in figure 6.2(a); less frequently, posterior butterflies are also encountered, figure 6.2(b).

As mentioned, the corpus callosum is a region characterized by high anisotropy: in figure 6.3, it is depicted the plot of the fractional anisotropy over the brain. This index, introduced in Chapter 2, describes the degree of anisotropy of a diffusion process. A value of zero means that diffusion is isotropic, i.e. it is unrestricted (or equally restricted) in all directions, while a value of one means that diffusion occurs only along one axis and is fully restricted along all other directions. In corpus callosum, the fractional anisotropy reaches values close to one, which means that the motion is forced along only one direction. In the following, we will investigate how cells move in this region of the brain.

6.1.1 Numerical implementation of the clinical case

To simulate the development of a butterfly glioma, we locate the initial tumor in the genu of the corpus callosum, as depicted in figure 6.4. Furthermore, we suppose that ϕ_0 follows a normal distribution reaching a maximum value slightly greater than ϕ_e , and that the oxygen concentration is obtained solving the stationary problem, as illustrated in section 4.3. The initial configurations of ϕ and n over

the computational mesh are sketched in figure 6.5.

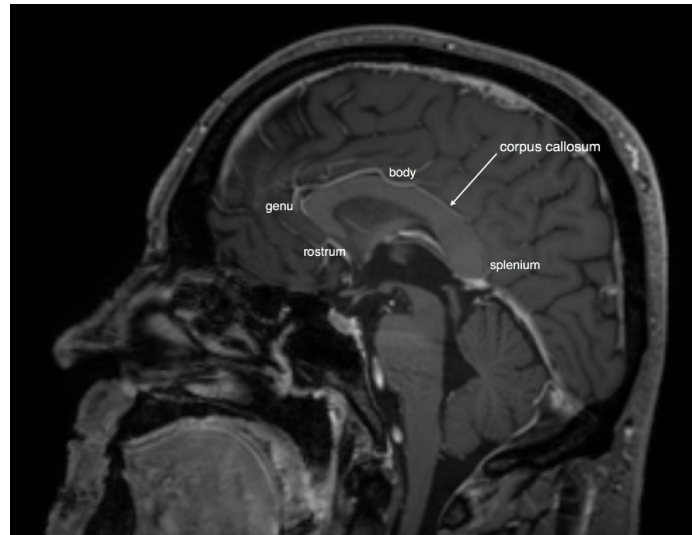


Figure 6.1: The anatomy of the corpus callosum, T1-mdc image gently provided by *Istituto Neurologico Carlo Besta*. It is located above the thalamus and under the cerebrum. Four different areas are identified: the rostrum, the genu, the body and the splenium.

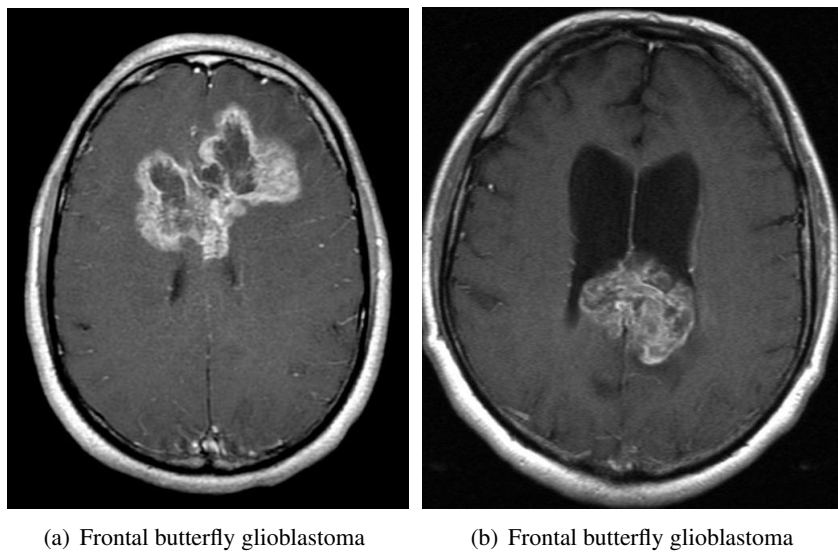


Figure 6.2: Frontal (left) and occipital (right) butterfly glioblastoma, figures from [62].

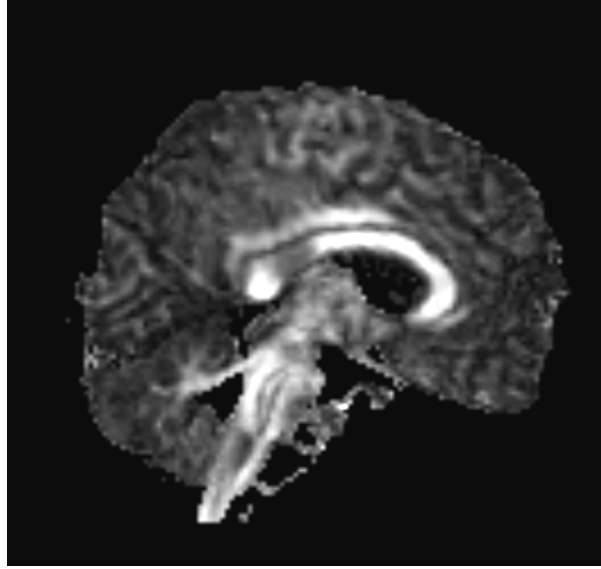


Figure 6.3: Visualization of the fractional anisotropy index on the brain of the patient. In anisotropic regions, FA is close to one and thus the voxels are brighter. The image has been gently provided by *Istituto Neurologico Carlo Besta*.

The most important and interesting term to analyze is the tensor \mathbf{T} . In table 6.1 we illustrate the tensor components T_{ii} , with $i = x, y, z$ over a mesh clipped along each plane. In the figures appearing in table 6.1, the tumor location is indicated by the white cross. Observing the collected figures, we assert that T_{xx} is the highest component in the region of interest: in fact it reaches values between two and three, while T_{yy} and T_{zz} are close to zero in that region. Consequently, cancerous cells will be forced to move along the x-direction and we expect that the tumor will grow anisotropically, losing its initial spherical shape.

Concerning the numerical model, as biological parameters we choose $M = 5000 \text{ mm}^{-2} \text{ Pa}$, $S_n = 10^4 \text{ day}^{-1}$, $\delta_n = 1000 \text{ day}^{-1}$, $\nu = 0.25 \text{ day}^{-1}$, $k_n = 20 \text{ mm}^2 \text{ mM}^{-1} \text{ day}^{-1}$ in CSF and $k_n = 100 \text{ mm}^2 \text{ mM}^{-1} \text{ day}^{-1}$ in GM and WM (more details are given in figure 6.6) and we use the codes illustrated in appendix A. As mentioned, the components of tensor \mathbf{T} and \mathbf{D} are then included in the numerical model by linear interpolation.

In the next section, the numerical results are illustrated.

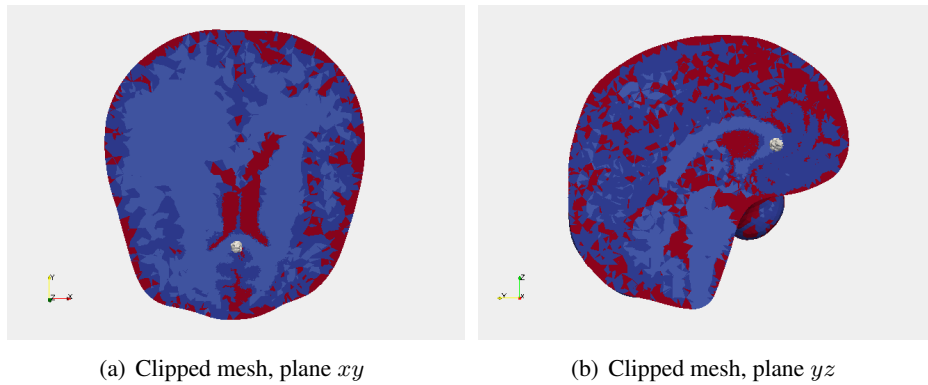


Figure 6.4: Initial location of the glioblastoma tumor (light gray sphere) overlapped to the labeled computational mesh. We remind that the red area, the dark blu area and the light blu area represent, respectively, the CSF, the grey matter and the white matter. We have located the tumor in the genu of the CC.

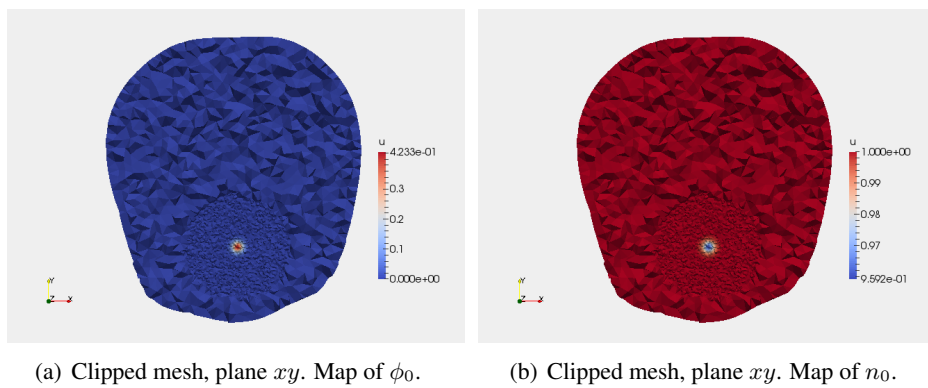


Figure 6.5: The initial configuration of ϕ and n plotted on the mesh, which has been cut along the plane xy . We refine the mesh in tumor area in order to have a well-refined solution keeping under control computational costs.

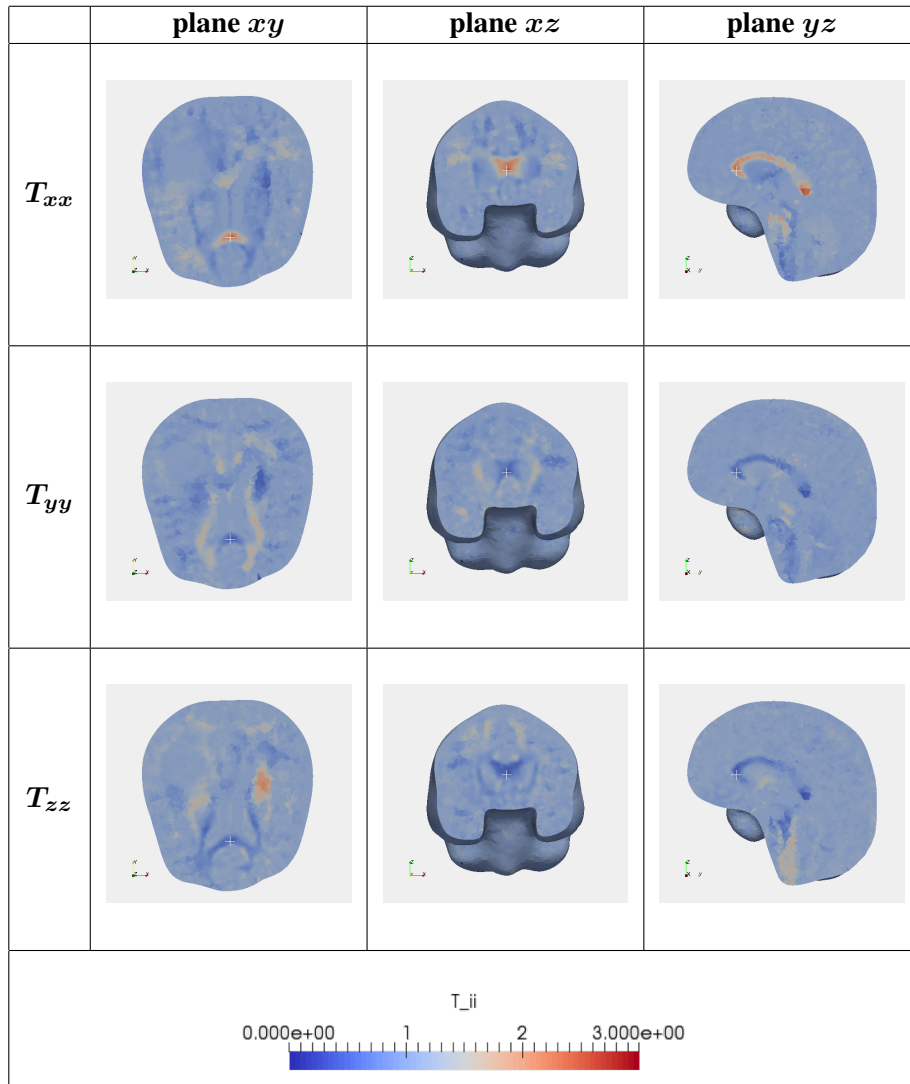


Table 6.1: Diagonal components of \mathbf{T} over the brain mesh cut along each plane. Comparing the three components on each plane, we observe that T_{xx} is the component that has the higher value in the region of interest assuming a value between two and three whereas T_{yy} and T_{zz} are almost zero. As a matter of fact, it has been demonstrated [28] that corpus callosum fibers go from an hemisphere to the other. In consequence, the x -axis is the preferential direction of cells motion and nutrients diffusion in the corpus callosum. In the figures, the tumor location is indicated by the white cross.

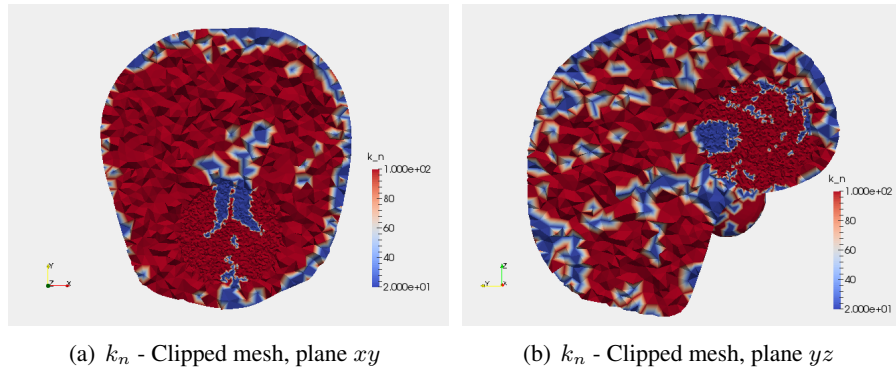


Figure 6.6: Plot of k_n over a clipped mesh along xy and yz planes. The chemotactic parameter acquires different values in relation to the tissue it deals with. In particular we assume that the chemotactic motion is reduced in the fluid since there are no fibers and thus we set k_n equal to $20 \text{ mm}^2 \text{ mM}^{-1} \text{ day}^{-1}$ here and equal to $100 \text{ mm}^2 \text{ mM}^{-1} \text{ day}^{-1}$ in the tissues. The present hypothesis is reasonable because brain tumors do not grow inside ventricles.

6.1.2 Numerical results

As mentioned earlier, we are interested in examining how the tumor follows the brain structures. Thus, to study the relation between tumor shape and diagonal components of the tensor \mathbf{T} , we perform a further simulation with homogenous diffusion and isotropic motion in the whole domain. In other words, we simulate a new model that has been obtained substituting to the tensor \mathbf{D} the relation $\mathbf{D} = D_n \mathbf{T}$, where D_n is defined as in table 3.1, and to the tensor \mathbf{T} the identity matrix. In the following, we will call *butterfly simulation* the test with real data, and *isotropic simulation* the new test defined ad hoc.

We have performed both simulations till iteration 250, i.e. 25 days after the first diagnosis of the tumor. In table 6.2, we compare ϕ and n concentration over the computational mesh cut along the xy plane in both test cases at time steps $t=5$ days, $t=10$ days, $t=15$ days, $t=20$ days, $t=25$ days. We observe that, in the butterfly simulation, the glioblastoma loses the initial spherical shape and assumes a configuration that reflects the structure of the tensor \mathbf{T} ; whereas, in the isotropic simulation, the glioblastoma maintains the spherical configuration. The maximum values reached by the cellular concentration in both tests are comparable, with a

ϕ_{max} that is slightly higher for the butterfly simulation.

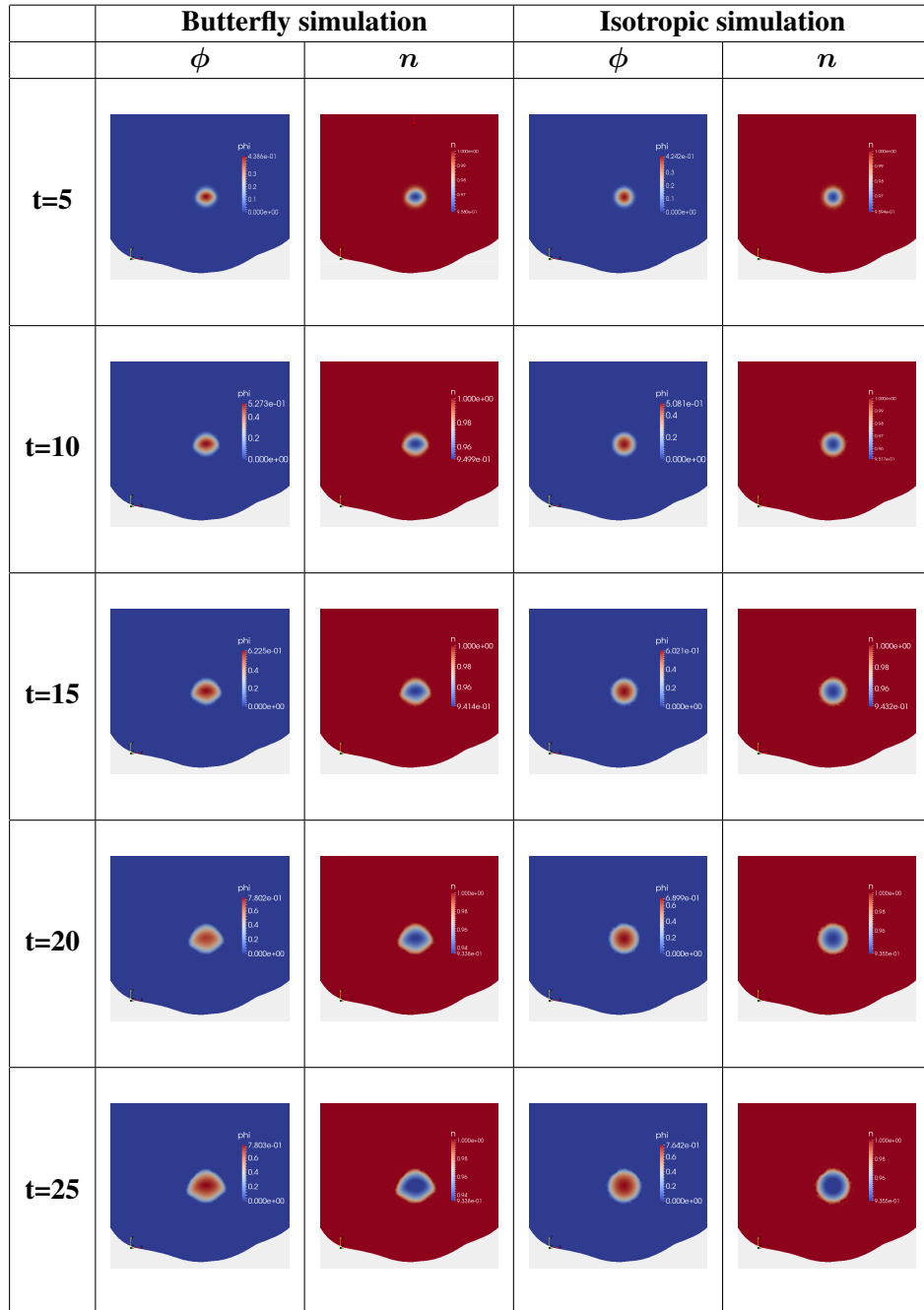


Table 6.2: Plot of ϕ and n concentration over the computational mesh cut along the xy plane for both butterfly and isotropic simulations.

As concerns the dimension of the glioblastoma at $t=25$ days, we have that $\Delta x = 21$ mm, $\Delta y = 18$ mm, $\Delta z = 17.3$ mm for the butterfly simulation; and $\Delta x = 17.6$ mm, $\Delta y = 18.2$ mm, $\Delta z = 18.5$ mm for the isotropic case. As expected, due to the structure of the tensor \mathbf{T} , Δx is bigger in the first case. Thus, more interesting is the qualitative aspect that the tumor acquired in the case of the butterfly simulation. In figures 6.7 we overlap the thresholded ϕ at $t=5$, 15 and 25 days to the T_{xx} mesh cut along the plane xy . Observing the figures, we assert that tumor shape follows the x -axis in the region in which T_{xx} is higher (red region) assuming a triangular configuration. Concerning the other components, we have shown in table 6.1 that T_{yy} and T_{zz} assume lower values in the CC and thus the chemotactic motion of cells along those directions is avoided. We confirm this hypothesis observing the tumor volume at the time step $t=25$ days overlapped to the maps of T_{ii} on the mesh cut along each plane, which we report in table 6.3. The tumor presents an elongated shape along the x direction with a flat top part. It is interesting that it appears almost isotropic in the yz plane. Hence, in the region out of the corpus callosum, the values assumed by the three components are comparable and thus the glioblastoma grows isotropically. The clipped ϕ concentration in plane yz is shown in figure 6.8.

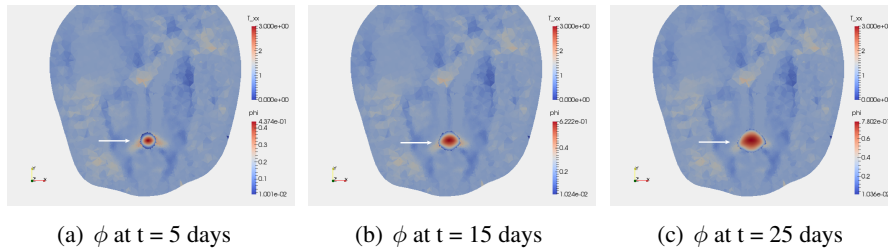


Figure 6.7: Thresholded volume fraction ϕ (indicated by the white arrow) plotted over the T_{xx} component (in transparency), at times $t=5$ days, $t=15$ days and $t=20$ days. It is possible to notice that the concentration of the cellular fraction is anisotropic and follows the preferential direction determined by the T_{xx} component.

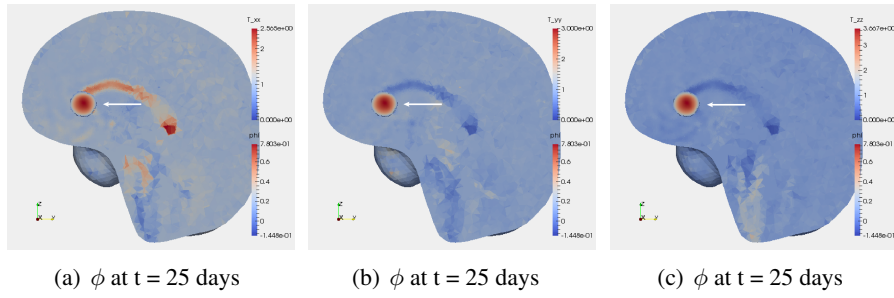


Figure 6.8: Thresholded volume fraction ϕ (indicated by the white arrow) in relation to the values assumed by the components T_{ii} in the corpus callosum shown at time steps $t=25$ days along the plane yz . It is possible to notice that the tumor assumes a isotropic shape along this plane since the values assumed by T_{ii} are similar in the region outside the CC.

	plane xy	plane xz	plane yz
T_{xx}			
T_{yy}			
T_{zz}			

Table 6.3: Tumor volume at time step $t=25$ days overlapped to the maps of T_{ii} over the brain mesh cut along each plane. Comparing the resulting volume, we assert that the glioblastoma assumes an elongated shape along the x direction, as it is possible to see in plane xy with a flat superior part, as shown in plane xz , and an isotropic shape in plane yz .

Finally, tumor growth has to be examined on the basis of the heterogeneous chemotactic coefficient defined. As shown in figure 6.6, we have made the hypothesis that the chemotactic coefficient assumes a lower value in the ventricles because of the absence of fibers that facilitate cellular motion. Indeed, the lateral ventricles are located below the corpus callosum, separated by a thin layer of white and grey matter called septum pellicidum, where butterfly glioblastoma is not allowed to spread into. In figure 6.9 we illustrate the thresholded ϕ concentration over the heterogeneous chemotactic parameter mapped on the computational mesh at time steps $t=5$ days, $t=15$ days and $t=25$ days. For the particular choice of parameters, the effect of the lower chemotactic coefficient is not sufficiently appreciable. Indeed, we remark that cancer cells motion depends also on the term $(\nabla\Sigma)/M$, which is homogeneous in the whole domain. For completeness, in figure 6.10 we show the thresholded ϕ concentration at $t = 25$ days in relation to the heterogeneous chemotactic coefficient also for the isotropic simulation. In this case too, the presence of a different chemotactic value for the tissue and the fluid is not sufficiently clear for the same reason described previously. More tests are needed in order to figure out which should be the better choice of the biological parameters.

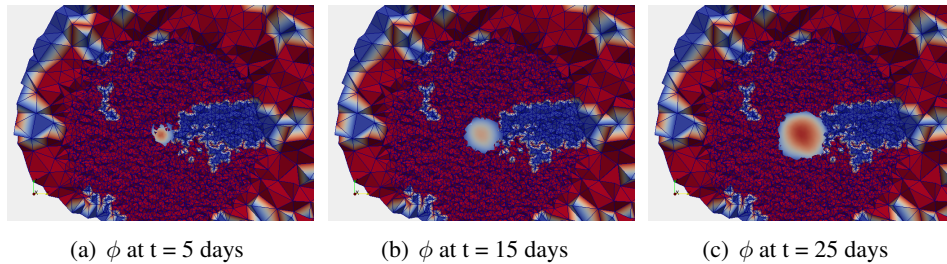


Figure 6.9: ϕ concentration in relation to the chemotactic coefficient in the ROI at time steps $t=5$ days, $t=15$ days and $t=25$ days.

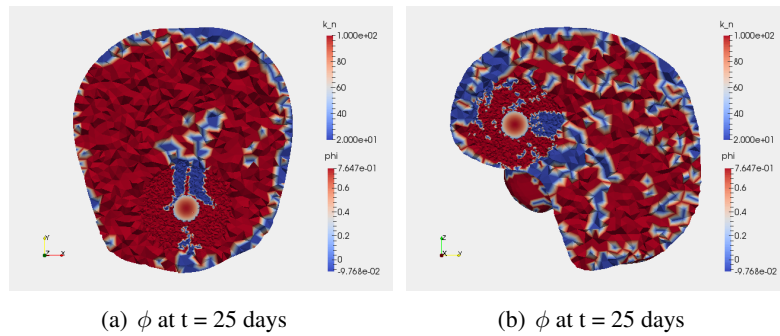


Figure 6.10: ϕ concentration in relation to the chemotactic coefficient in the case of the isotropic simulation. The effect of a reduced chemotactic motion into the lateral ventricles is not sufficiently appreciable also in the present test.

6.2 Simulating glioblastoma regrowth after resection

In this section, we describe and numerically simulate the medical situation in which glioblastoma cannot be completely removed during the surgical operation and some cancerous cells are left behind. Indeed, in some clinical cases the complete resection of the cancer is impossible: often the tumor is located near a sensitive area of the brain with vital functions or it happens that the cancerous cells are too infiltrate into fibers and thus difficult to be reached during the medical intervention. Indeed, it is important to remember that gliomas are highly infiltrating tumors and complete removal is impossible in almost every case. Anyway, the partial removal of the tumor mass helps to relieve patient's symptoms by reducing pressure on the brain and in a second time surviving cells are treated by radiation therapy and chemotherapy.

In the following the description of the simulation and the relative numerical results is reported. We are interested in discovering how glioblastoma surviving cells develop and regrow in time, without any supplementary treatment (we suppose, indeed, that the patient is not treated by chemo or radiotherapy after intervention).

6.2.1 Numerical implementation of the clinical case

We start from a T1 MRI gently provided by *Istituto Neurologico Carlo Besta*, which is the same medical image used for creating the computational mesh described in chapter 4. Then, we manually segment the real tumor, making use of *Slicer3D* [64] and of its module named *Editor*. We associate two labels to the tumor region as depicted in figure 6.11. The pink area represents the mass of the tumor that has been removed during medical resection, while the green region indicates the cancerous cells that remain after the intervention.

Using the process described in Chapter 4, we build the mesh and we pass the regions' information to the geometry. In this way, we are able to distinguish three different regions on the mesh: the healthy tissue, the mass of the resected tumor and the mass of surviving cells, as depicted in figure 6.12. In figure 6.13, a 3D sketch of the clinical case is depicted.

Before starting the simulation, we need to make different assumptions on the model's behavior in relation to the region on which the governing equations are implemented. In particular, we have to specify how the model deals with the cavity, i.e. the region occupied by glioblastoma before surgery.

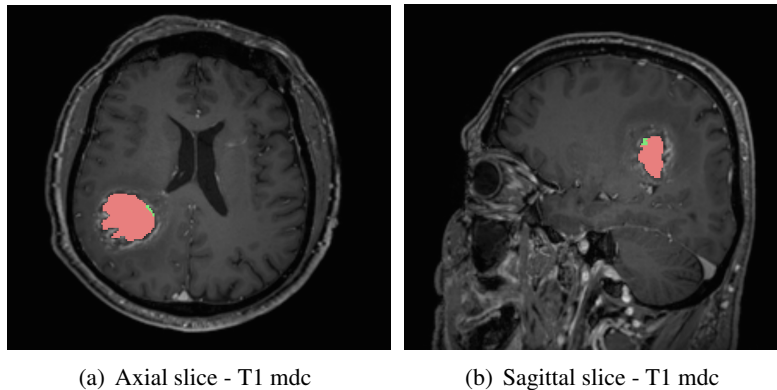


Figure 6.11: Manually segmentation of the different regions of interest. We suppose that the region labeled by the pink color is the mass of the glioblastoma that has been removed by surgery, while the area indicated by the green color represents the mass of surviving cells.

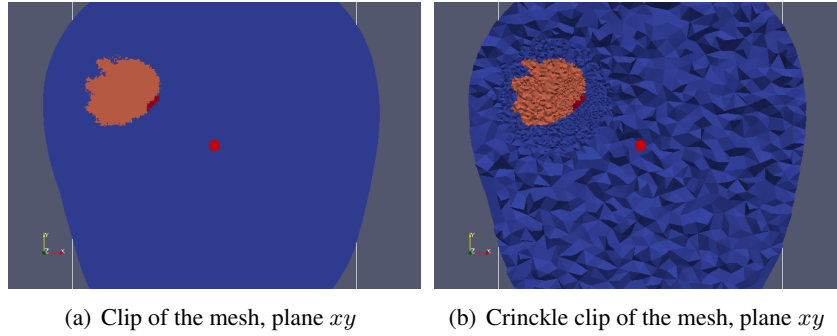


Figure 6.12: (a) Three regions are identified on the mesh: the blue region is the healthy tissue, the orange region identifies the tumor mass removed, the red region represents the surviving cells. (b) The mesh is refined in the area of interest.

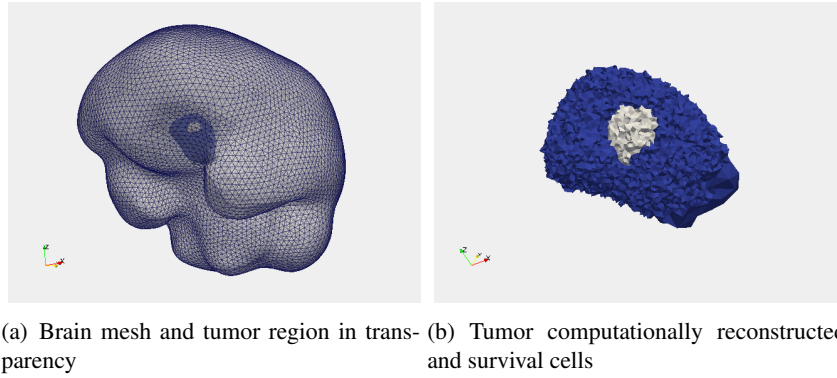


Figure 6.13: 3D sketched of the tumor mass resected and surviving cells. The blue region represents the glioblastoma computationally reconstructed while the white region identifies the area occupied by cancerous cell which are left behind.

In the region of resection, the following hypotheses hold:

- there is only the liquid phase, i.e. $\phi_l = 1$ and $\phi_c = 0$;
- the diffusion of nutrients is isotropic, i.e.

$$\mathbf{D} = D_n \begin{pmatrix} 1 & 0 & 0 \\ 0 & 1 & 0 \\ 0 & 0 & 1 \end{pmatrix}$$

where D_n is the typical oxygen diffusion coefficient in CSF that we have estimated to be between 180 and $250 \text{ mm}^2 \text{ day}^{-1}$ from the real data;

- the chemotactic motion of cells is isotropic because there are no fibers and no directions are preferential and consequently the tensor \mathbf{T} is

$$\mathbf{T} = \begin{pmatrix} 1 & 0 & 0 \\ 0 & 1 & 0 \\ 0 & 0 & 1 \end{pmatrix}$$

- the chemotactic coefficient k_n , because of the absence of fibers, assumes a lower value, as depicted in figure 6.14;
- the production rate parameter S_n is zero in the center of the cavity and tends to the normal healthy value of 10^4 day^{-1} following a normal profile, as depicted in figure 6.15, since in the resected area no tissue and no vasculature is present.

Concerning the other biological parameters, we choose $M = 5000 \text{ mm}^{-2} \text{ Pa}$, $\delta_n = 1000 \text{ day}^{-1}$ and $\nu = 0.25 \text{ day}^{-1}$.

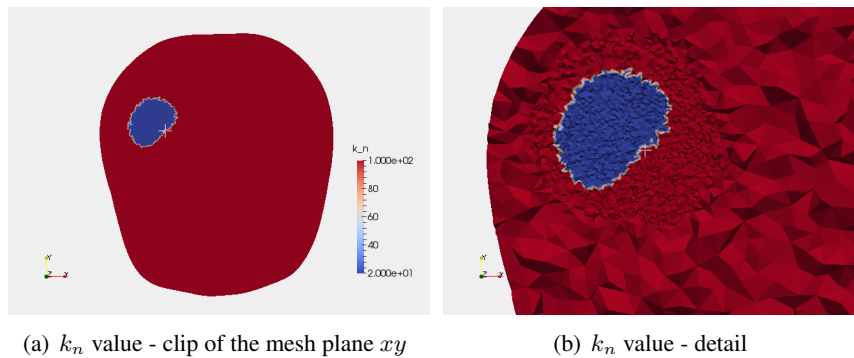


Figure 6.14: Value of the chemotactic coefficient k_n depicted on the mesh cut along plane xy . We make the hypothesis that the chemotactic parameter assumes a lower value in the cavity because of the absence of fibers. The location of the tumor is indicated by the white cross.

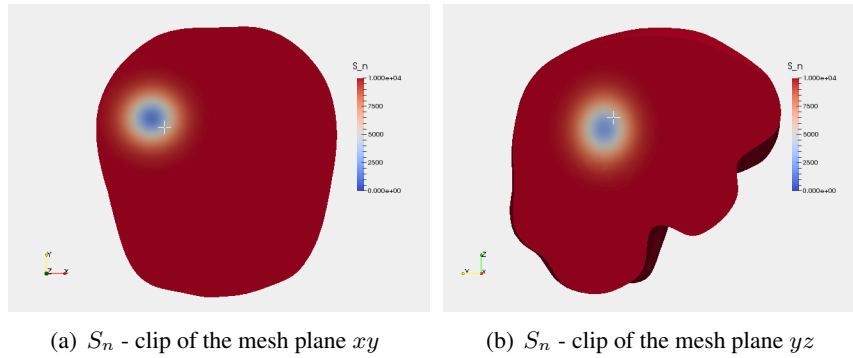


Figure 6.15: S_n concentration depicted on the mesh cut along (a) xy the plane and (b) the yz plane. We suppose that the production rate is almost null in the center of the cavity and reaches its normal value in the healthy tissue. The location of the tumor is indicated by the white cross.

Finally, for sake of completeness, in figures 6.16 and 6.17 respectively we illustrate the diagonal components T_{ii} and D_{ii} , with $i = x, y, z$ on the computational mesh cut along the plane xy . As we notice, no preferential directions are highlighted by the tensor \mathbf{T} in the region where survived cells are located, specified by the white cross in the image. As concern the tensor \mathbf{D} , we have assumed that oxygen diffusion coefficient is higher in the area of resection.

As mentioned, the tensors' components are then included automatically and continuously in the model through linear interpolation. To simulate the model we use the codes illustrated in appendix A.

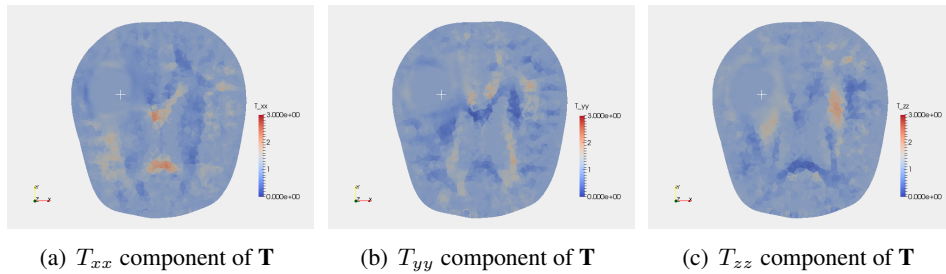


Figure 6.16: Diagonal elements of tensor \mathbf{T} on the mesh clipped along the xy plane. In the area of the removed tumor, T_{ii} are equal to one. The tumor location is specified by the white cross.

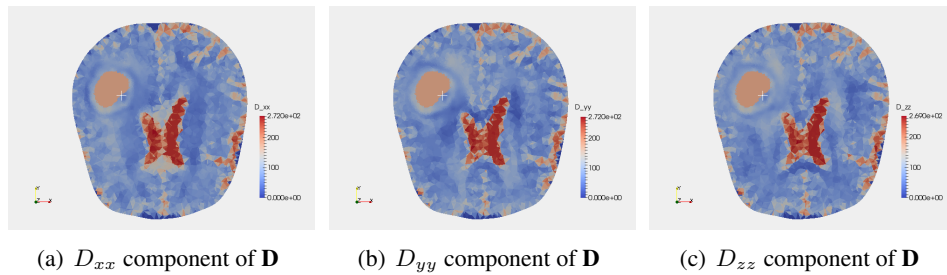


Figure 6.17: Diagonal elements of tensor \mathbf{D} on the mesh clipped along the xy plane. In the area of the removed tumor, \mathbf{D} is an isotropic tensor, whose elements are equal to a certain value D_n .

6.2.2 Numerical results

The present test simulates the development of a secondary tumour mass starting from some cells of the primary tumour that have not been removed. Thereby, the mesh has to be highly refined, as shown in figure 6.18, in order to keep under control computation errors that arise from a slightly smooth interface host/tumor with the consequence of long times of computation. The following observations on the development of the cellular fraction and the consumption and diffusion of nutrients are made paying attention to the hypothesis assumed on the model's behavior in the region of resection.

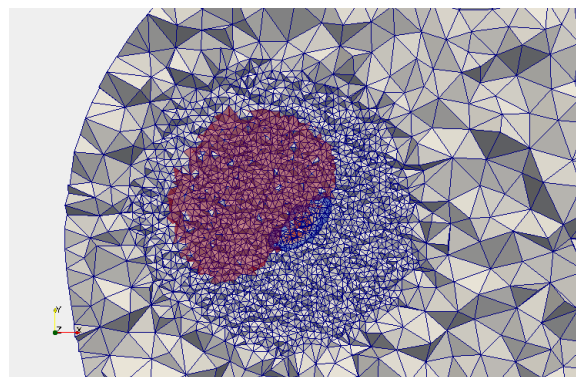


Figure 6.18: Detail of the refined mesh in the region of interest. In transparency, the red area represents the portion of the glioblastoma that has been removed, whereas the blue area represents the surviving cells, that have been left behind.

In table 6.4, we examine the concentration of ϕ and n over the computational mesh cut along the xy plane 5 days, 10 days, 15 days and 20 days after the virtual resection, which corresponds to the initial numerical time step. The collected figures show that the cellular volume fraction ϕ increases, whereas the oxygen concentration n decreases. The tumor expands also in the surrounding tissue and its volume raises. In figures 6.19 and 6.20, we report the configuration of ϕ and n over the computational mesh clipped along the planes xz and yz at the time steps $t = 0$ days, $t = 10$ days and $t = 20$ days.

We now pay attention to how the concentration of ϕ and n is distributed in the neoplastic region. The detailed image is sketched in figure 6.21. We observe that the region of the minimum concentration of oxygen does not correspond to the region of the maximum concentration of ϕ , as we expect. The reasons have to be found in how we have defined the diffusion coefficient, the chemotactic coefficient and the production rate coefficient in the region of interest. As concerns the distribution of the oxygen, n reaches its minimum value in the resection area. Indeed, the oxygen diffusion coefficient is higher in the cavity and consequently substrates diffuse easily and, moreover, S_n is lower in this region and thus, the nutrients consumed are less replaced. The maximum value of ϕ , instead, is reached in the area where the initial tumoral mass is located. This behavior could be caused by the fact that in the region of resection the motion of the cancerous cells is prevented because of a lower value of k_n . The figures 6.22 and 6.23 explain exhaustively this fact.

Finally, in figure 6.24, we observe the evolution of the tumor volume at time steps $t = 0$ days, $t = 10$ days and $t = 20$ days. At the beginning, it is slightly C-shaped with a small spherical satellite mass of diseased cells on its left, which is made visible for the first time thanks to a 3D visualization. At the final time step, it presents a more rotund aspect with a bigger satellite mass. To understand how the tumor has grown, we overlap the initial configuration to the final one. We notice that the tumor has grown more in the region surrounding the cavity than inside it. This fact is probably due to the heterogeneity of the chemotactic coefficient,

which is higher outside the region and lower inside it such that cells are facilitated to move into the healthy fibers, and to the nutrient production rate coefficient S_n , which is almost null in the center of the tumor and assumes its physiological values in the healthy tissue.

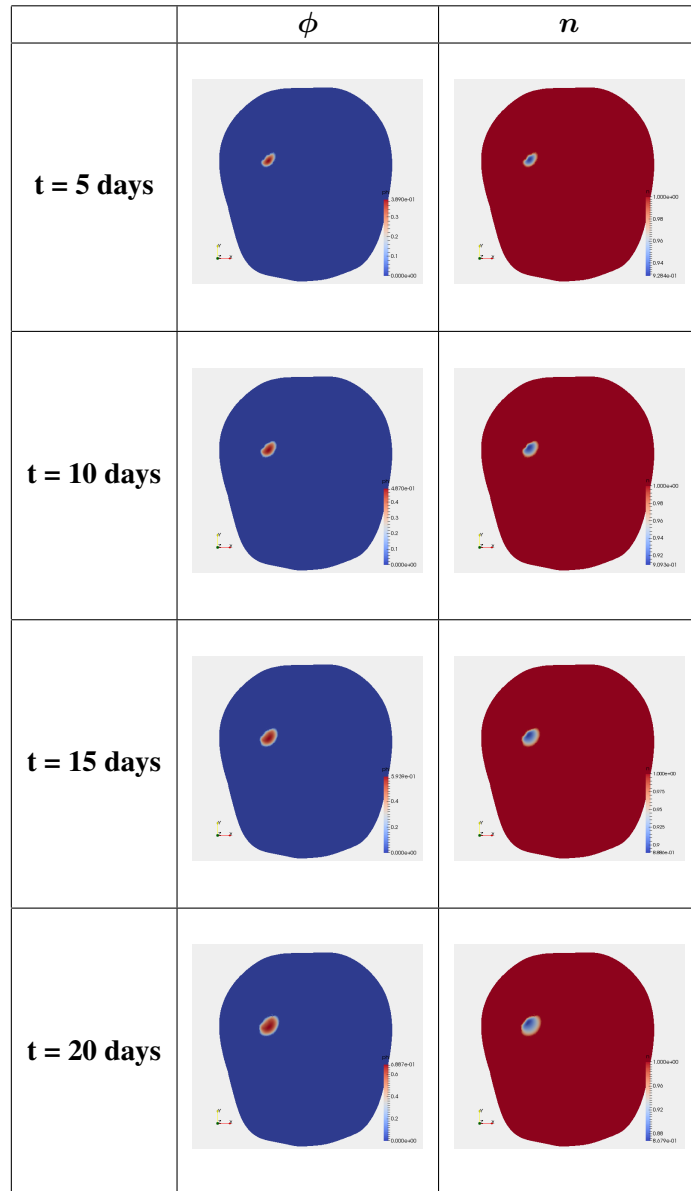


Table 6.4: The concentration of ϕ and n at the given time steps depicted over the computational mesh cut along the xy plane.

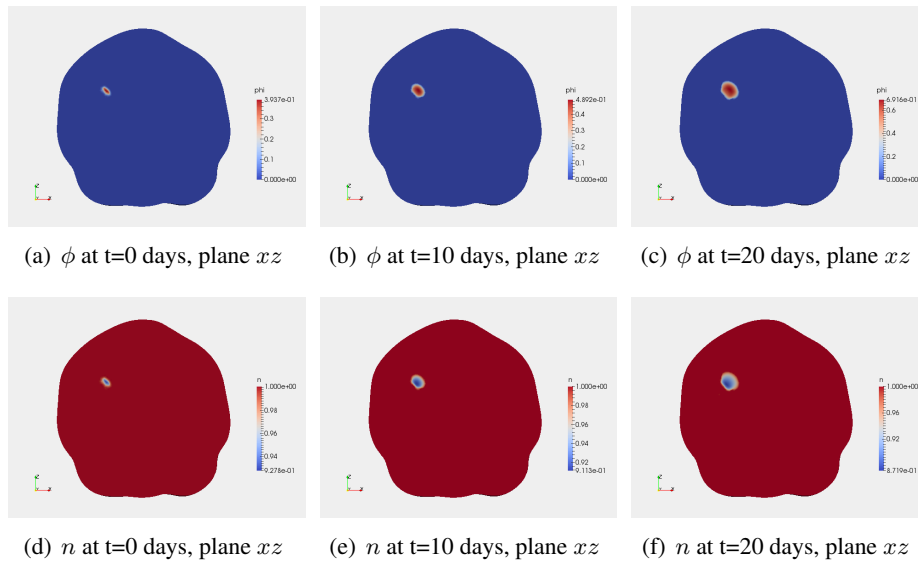


Figure 6.19: Concentration of ϕ and n over the computational mesh clipped along the plane xz in the midline of the tumor at the time steps $t = 0$ days, $t = 10$ days, $t = 20$ days.

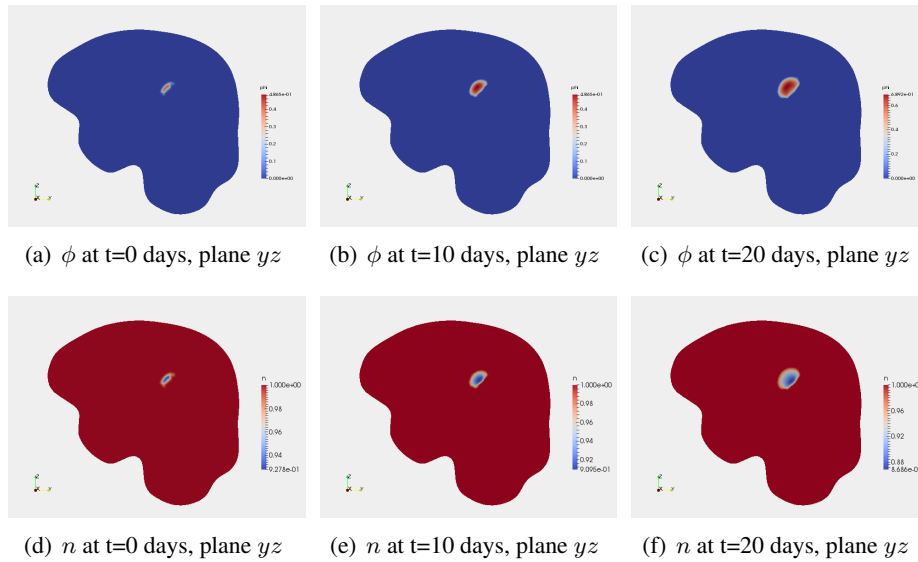


Figure 6.20: Concentration of ϕ and n over the computational mesh clipped along the plane yz in the midline of the tumor at the time steps $t = 0$ days, $t = 10$ days, $t = 20$ days.

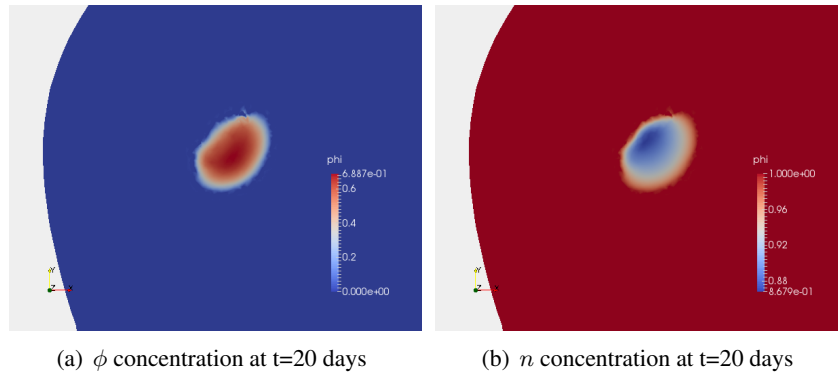


Figure 6.21: Detail of ϕ and n concentration on the clipped mesh over the plane xy . Particularly interesting is the distribution of the variables' concentration in the diseased region.

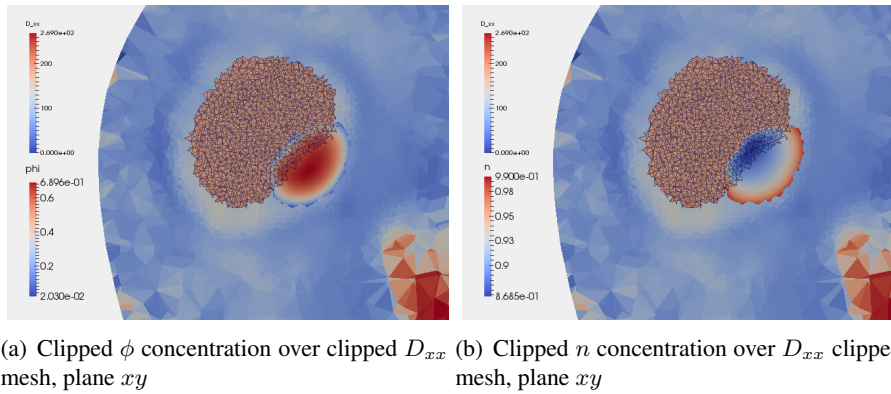
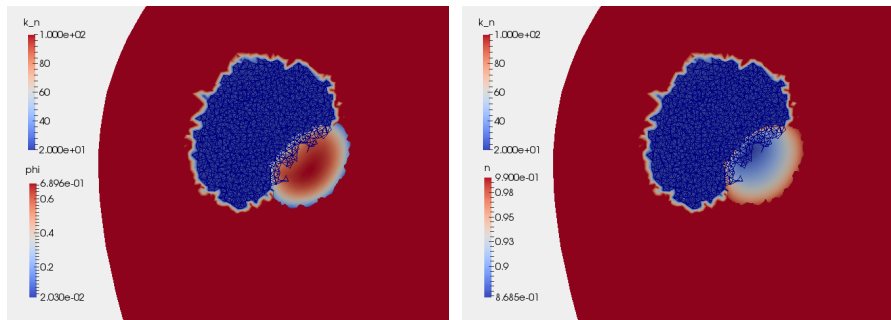
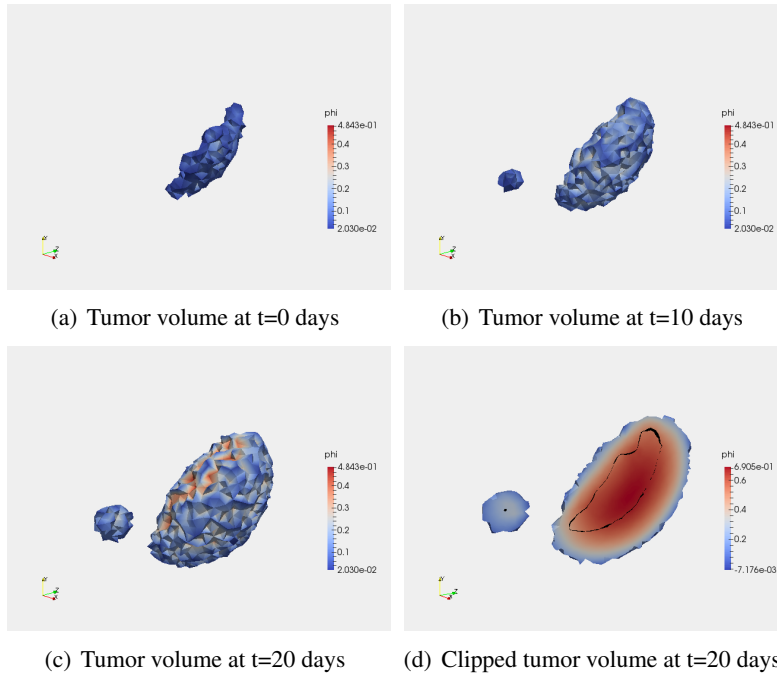


Figure 6.22: Clipped thresholded ϕ and n concentration over clipped D_{xx} mesh cut along plane xy at time step $t = 20$ days. The thresholded tumor has been obtained setting $\epsilon_+ = 0.02$, whereas the oxygen concentration has been thresholded at 0.99 . The resected region is illustrated meshed in order to highlight its borders.



(a) Thresholded ϕ concentration over k_n concentration clipped mesh (b) Thresholded n concentration over k_n concentration clipped mesh

Figure 6.23: Clipped thresholded ϕ and n concentration in relation to the heterogeneous chemotactic coefficient depicted over the clipped mesh cut along plane yz at time step $t = 20$ days. The thresholded concentration has been obtained as in figure 6.22.



(a) Tumor volume at $t=0$ days (b) Tumor volume at $t=10$ days
(c) Tumor volume at $t=20$ days (d) Clipped tumor volume at $t=20$ days

Figure 6.24: Volumetric growth of glioblastoma tumor at time steps $t = 0$ days, $t = 10$ days and $t = 20$ days, obtained thresholding ϕ at $\epsilon_+ = 0.02$ as defined in Chapter 4. In figure (d) the initial configuration of the tumor (which occupies the region sketched by the black line) is overlapped to the clipped tumor volume at $t=20$ days.

Conclusions and Future works

In this project we have developed a mathematical model in order to predict the invasion and the growth of a glioblastoma, a highly malignant brain tumor characterized by an infiltrative nature. Starting from the mixture models found in literature, we have proposed a new model that takes into account the **heterogeneity** and the **anisotropy** of the brain tissues thanks to the introduction of a chemotactic flux of mass and the patient-specific diffusion tensor imaging data, gently provided by the Istituto Neurologico Carlo Besta. The research has been inspired by the consideration that including real data in the mathematical model would have led to a more truthful prediction of the tumor evolution. Thus, we have created a computational mesh starting from a MR image of a patient affected by glioblastoma and we have extracted geometric information from the diffusion tensor. Thanks to imaging technique and numerical codes, we have succeeded in creating a local diffusion tensor and including anisotropy and heterogeneity in the model. Moreover, we have defined a new local tensor, which we have called tensor of the preferential directions, comparing each component of the diffusion tensor to the mean diffusivity in each point of the domain. This mathematical object encapsulates the information on the real geometry of the brain and thus it allows to describe the anisotropic motion of the tumor cells. The new tensor, indeed, weights the chemotactic term presented in the governing equation of the cellular fraction and thus forces the cells to move along specific directions.

In a second time, to simulate the mathematical model, we have discretize the problem using the finite elements method and we have developed numerical codes mak-

ing use of an open-source software called FEniCS.

In particular, we have performed a sensitivity analysis of the biological parameters present in the model in order to figure out which ones among them has more influence on the anisotropic tumor behavior. We have done two analysis: the first has considered the combined effects of the interphase friction parameter and the chemotactic friction parameter on the cellular evolution, while the second has considered the combined effects of the production of nutrients and the consumption of nutrients. We have discovered that the chemotactic coefficient has a huge influence on the anisotropic behavior of the tumor and that the relationship between the production and the consumption of nutrients determines not only the availability of nutrients in the environment and, in consequence, cell proliferation, but it also affects the chemotactic motion of cells.

Finally, to test the model, we have simulated two common clinical situations of medical interest. The first has concerned the development of a butterfly glioblastoma, a type of glioma that arises in the corpus callosum which is a bundle of white matter fibers located between the two hemispheres and characterized by high anisotropy. The characteristic feature of this tumor is that it spreads into both hemispheres symmetrically, simulating butterfly wings. Hence, we have located a virtual glioblastoma of small size in the genu of the corpus callosum and we have examined its development at given time steps. The resulting data show a tumor shape that actually follows the architecture of the brain region in which it is located. Unfortunately, we haven't succeeded in simulating the butterfly wings. The heterogeneity of the brain tissue and the reproduction of the real geometry of the cancer is a hard challenge for biomathematical modeling. In our case, more simulations are needed in order to test different parameters and to include more patient-specific data.

Then, we have simulated the medical situation in which the brain tumor has not been completely removed and some diseased cells have been left behind. Indeed, almost always, gliomas cannot be completely removed due to their high infiltrative

nature. Although after the medical intervention patients are treated with radiotherapy or chemotherapy, we have not considered any treatment in the model. The numerical results have suggested a tumor that tends to expand in the healthy tissue instead of accumulating in the region of resection.

As concerning the future works, first of all, more biological researches on the parameters present in the model are needed. Indeed, it is hard to find truthful parameters relative to glioblastoma tumors. Furthermore, since the novelty of the present research lies in the introduction of patient-specific data and real geometry, it would be interesting observing how the numerical results change in relation to different patients. At the same time, it would be also useful to follow the tumor evolution of a single patient. As a matter of fact, the structure of the brain fibers changes as the tumor grows and thus, it would be necessary to have more medical data at given time steps in order to compare the numerical results with the real development of the tumor. Finally, some possible improvements that concern the formation of new vessels (angiogenesis) or the medical treatments given to a patient could be introduced in the mathematical model.

Appendix A

Code Documentation

In this appendix we present the codes we have implemented for the solution of the tumor growth problem defined in the previous part of this work. Firstly, however, we describe briefly how we have obtained a smooth and regular brain tetrahedral mesh. Thus, in the first section we explain step by step the process we employed, illustrating summarily the algorithms and the pieces of code written by M. Manica [41] and modified for our aims. Then, in the second section, we focus on the codes developed for the main problem. We use an open-source software called the FEniCS project, through a Python interface. The entire codes are reported with a brief explanation.

A.1 Mesh Construction - Numerical background

In order to create a mesh, we make use of a library named *Vmtk*. It is "a collection of libraries and tools for 3D reconstruction, geometric analysis, mesh generation and surface data analysis for image-based modeling of blood vessels" [31]. Even though it has been developed for blood vessels, thanks to its powerful tools, it is possible to adapt *vmtk*-algorithms to succeed in our purpose.

First of all, we create a labeled map of the brain (e.g. **BLM.mhd**) starting from

a series of T1-MRIs, as described in chapter 4.1. In this map a label is assigned to each region: label 2 is given to the background, label 13 to the grey matter, label 14 to white matter and 25 to cerebrospinal fluid. The quickest and most simple way of creating a surface model is to contour the image using the Marching Cubes algorithm. This algorithm is able to extract a surface that we call **surf.vtp** from the labeled map at a certain level (e.g. level 3). In this way, we manage to extract the brain surface from the background.

```
vmtkmarchingcubes -ifile BLM.mhd -l 3 -ofile surf.vtp
```

At this point, the rough surface has to be cleaned and smoothed in order to do not have intersections of edges or topological problems, and then re-meshed.

```
vmtksurfaceconnectivity -ifile surf.vtp --pipe  
vmtksurfacesmoothing -passband 0.001 -iterations 100 --pipe  
vmtksurfacedecimation -reduction 0.95 --pipe  
vmtksurfaceviewer --pipe vmtksurfaceremeshing  
-elementsizemode area -area 10 -minarea 4 --pipe  
vmtksurfaceviewer -ofile surf_re.vtp
```

Once the surface is perfectly smoothed, the tetrahedral mesh is performed calling *TetGen* in **meshing.py** and refined in the tumoral area by the algorithm named **refinement.py**. The final step consists in overlapping the brain label map to the tetrahedral mesh using **label.py**, so that the biological features of the tissues are passed to the computational object. The final mesh is now ready for the numerical simulations. In the following we report portions of the codes used; for the integral versions see [41].

```
# --- meshing.py --- #  
...  
reader=vtk.vtkXMLPolyDataReader()  
reader.SetFileName("/home/cristina/TESE/Mesh_Creat/surf_re.vtp")  
...  
sizingFunctionArray.SetName("SizingFunction")  
...  
# Call tetgen  
tetgen=vmtkscripts.vtkTetGen()
```

```

tetgen.Mesh= stm.Mesh
tetgen.GenerateCaps = 0
tetgen.UseSizingFunction = 1
tetgen.Refine=0
tetgen.SizingFunctionArrayName = "SizingFunction"
tetgen.Order = 1
tetgen.Quality = 1
tetgen.PLC = 1
tetgen.NoBoundarySplit = 1
tetgen.RemoveSliver = 0
tetgen.OutputSurfaceElements = 0
tetgen.OutputVolumeElements = 1
tetgen.Execute()
...

# --- refinement.py --- #
...
for i in range(mesh.GetNumberOfPoints()):
    pb=mesh.GetPoint(i)
    dist=sqrt(pow((pb[0]-205),2) + pow((pb[1]-290),2) + pow((pb
        [2]-27),2))
    if dist <= 30:
        sizingFunctionArray.SetTuple1(i,1.2)
    else:
        sizingFunctionArray.SetTuple1(i,3)
...

# --- label.py --- #
...
# Mesh reader
reader = vtk.vtkUnstructuredGridReader()
reader.SetFileName("Mesh_re.vtk")
reader.Update()
mesh=reader.GetOutput()
...
# Metaimage reader
ireader = vmtkscripts.vmtkImageReader()
ireader.InputFileName = "BLM.mhd"
ireader.Execute()
img = ireader.Image
...
# Label assignment
for ig in range(ncells):
    mesh.GetCellPoints(ig,ptlst)
    mesh.GetPoints().GetPoints(ptlst,pt)
    barycenter(pt,pb)
    pt.Reset()
    im=ploc.FindClosestPoint(pb)
    print iml.GetComponent(im,0)
    if iml.GetComponent(im,0)==2.0:
        cell_label.SetTuple1(ig,25)
    else:

```

```

cell_label.SetTuple1(ig, iml.GetComponent(im, 0))
writer = vtk.vtkUnstructuredGridWriter()
writer.SetFileName("Mesh_lab.vtk")

```

At this point, we deal with the components D_{ij} , with $i, j = x, y, z$ of the diffusion tensor \mathbf{D} . As mentioned, it is possible that the six images representing D_{ij} have to be registered on the T1 used for the mesh creation. We use an open source software named *FSL*: it offers two robust and easy-to-use tools for medical image registration called *FNIRT* and *FLIRT*. Firstly, we register the image of the D_{xx} component and then we use the transformation matrix to register the other components. The commands utilized are:

```

Flirt -in Dxx.nii -ref GBM_T1_3D_TFE_rest_SENSE_10_1.nii -omat
outputmatrix.nii -dof 6 -out Dxx_reg.nii

```

```

Flirt -in Dij.nii -ref GBM_T1_3D_TFE_rest_SENSE_10_1.nii -applyxfm
-init outputmatrix.nii -dof 6 -out Dij_reg.nii

```

Once the components are registered to the reference image, their format is switched from the *nifti* file format to the *mhd* file format and therefore ready for the labeling process. We create six computational meshes on which to each cell the projected value is associated.

A.2 Code implementation - The FEniCS project

To perform numerical simulation we rely on a open source software named the FEniCS project through a Python interface. It is a software specialized in automated solution of differential equation by finite element and it is actually a collection of *inter-operable components*, including the problem-solving environment DOLFIN, the form compiler FCC, the finite element tabulator FIAT, the just-in-time compiler Instant, the code generation interface UFC and the form language UFL [38], as depicted in figure A.1.

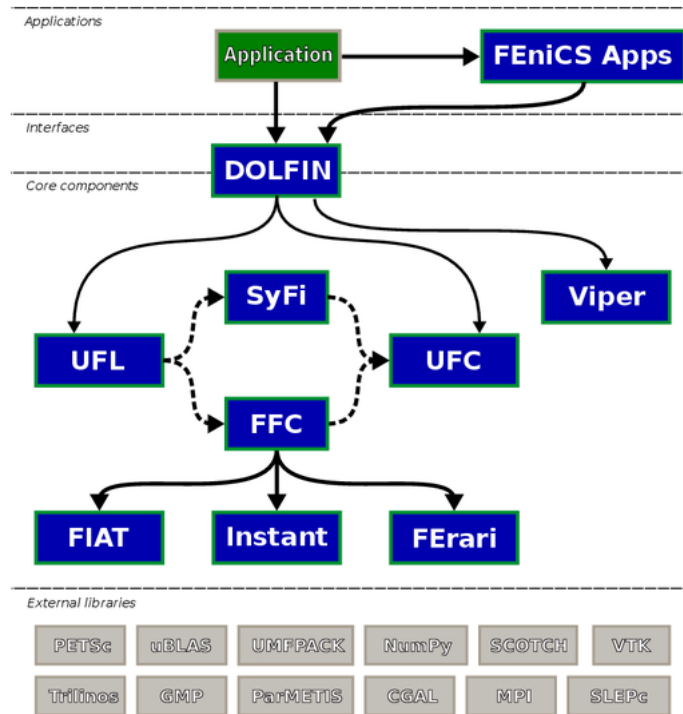


Figure A.1: DOLFIN functions as the main user interface of FEniCS and handles the communication between the various components of FEniCS and external software. Solid lines indicate dependencies and dashed lines indicate data flow [38].

First of all, we have to convert the seven meshes (the brain mesh and the six components of the diffusion tensor) from the *.vtk* format to the *.xml* format, the one supported by FEniCS, making sure that the cells information (tissue labels and diffusion values) are given to the new XML meshes, that we call **brain.xml** and **Dij.xml**.

```
vmtkmeshreader -ifile Mesh_lab.vtk -entityidsarray "cell_labels"
--pipe vmtkmeshwriter -entityidsarray "cell_labels"
-writeregionmarkers 1 -ofile brain.xml -f "dolfin"
```

```
vmtkmeshreader -ifile Mesh_Dij.vtk -entityidsarray "Dij_labels"
--pipe vmtkmeshwriter -entityidsarray "Dij_labels"
-writeregionmarkers 1 -ofile Dij.xml -f "dolfin"
```

In order to be able to use diffusion tensor information collected into the XML

meshes, we have implemented a code which reads the diffusion values and stores them as *mesh function*. In the same code, we compute T_{ij} , the six components of \mathbf{T} , the tensor of preferential directions and we stock them as *mesh function* too. Then these data will be read in the main code in a second time.

```
# DefineT.py

from dolfin import *

#Read of the XML meshes
mesh = Mesh("brain.xml")

mvc_Dxx = MeshValueCollection("size_t", mesh, "Dxx.xml")
meshf_Dxx = MeshFunction("size_t", mesh, mvc_Dxx)
values_Dxx = meshf_Dxx.array()

mvc_Dyy = MeshValueCollection("size_t", mesh, "Dyy.xml")
meshf_Dyy = MeshFunction("size_t", mesh, mvc_Dyy)
values_Dyy = meshf_Dyy.array()

mvc_Dzz = MeshValueCollection("size_t", mesh, "Dzz.xml")
meshf_Dzz = MeshFunction("size_t", mesh, mvc_Dzz)
values_Dzz = meshf_Dzz.array()

mvc_Dxy = MeshValueCollection("int", mesh, "Dxy.xml")
meshf_Dxy = MeshFunction("int", mesh, mvc_Dxy)
values_Dxy = meshf_Dxy.array()

mvc_Dxz = MeshValueCollection("int", mesh, "Dxz.xml")
meshf_Dxz = MeshFunction("int", mesh, mvc_Dxz)
values_Dxz = meshf_Dxz.array()

mvc_Dyz = MeshValueCollection("int", mesh, "Dyz.xml")
meshf_Dyz = MeshFunction("int", mesh, mvc_Dyz)
values_Dyz = meshf_Dyz.array()

# Components of D
o11=MeshFunction("double",mesh,3)
o22=MeshFunction("double",mesh,3)
o33=MeshFunction("double",mesh,3)
o12=MeshFunction("double",mesh,3)
o13=MeshFunction("double",mesh,3)
o23=MeshFunction("double",mesh,3)

# Components of T
t11=MeshFunction("double",mesh,3)
t22=MeshFunction("double",mesh,3)
t33=MeshFunction("double",mesh,3)
t12=MeshFunction("double",mesh,3)
t13=MeshFunction("double",mesh,3)
```

```

t23=MeshFunction("double",mesh,3)

trace = MeshFunction("size_t",mesh,3)

n=len(values_Dzz)
i=0

while (i<n):
    trace[i] = (values_Dxx[i] + values_Dyy[i] + values_Dzz[i])
    if (trace[i]!=0):
        o11[i] = float(values_Dxx[i])
        o22[i] = float(values_Dyy[i])
        o33[i] = float(values_Dzz[i])
        o12[i] = float(values_Dxy[i])
        o13[i] = float(values_Dxz[i])
        o23[i] = float(values_Dyz[i])
        t11[i] = 3*values_Dxx[i]/trace[i]
        t22[i] = 3*values_Dyy[i]/trace[i]
        t33[i] = 3*values_Dzz[i]/trace[i]
        t12[i] = float(3*values_Dxy[i])/trace[i]
        t13[i] = float(3*values_Dxz[i])/trace[i]
        t23[i] = float(3*values_Dyz[i])/trace[i]
    if (trace[i] ==0):
        o11[i] = 86.4
        o22[i] = 86.4
        o33[i] = 86.4
        o12[i] = 0.0
        o13[i] = 0.0
        o23[i] = 0.0
        t11[i] = 1.0
        t22[i] = 1.0
        t33[i] = 1.0
        t12[i] = 0
        t13[i] = 0
        t23[i] = 0
    i=i+1

# Saving D components and T components
o11_file = File("o11.xml.gz")
o22_file = File("o22.xml.gz")
o33_file = File("o33.xml.gz")
o12_file = File("o12.xml.gz")
o13_file = File("o13.xml.gz")
o23_file = File("o23.xml.gz")
o11_file<< o11
o22_file<< o22
o33_file<< o33
o12_file<< o12
o13_file<< o13
o23_file<< o23

t11_file = File("t11.xml.gz")
t22_file = File("t22.xml.gz")
t33_file = File("t33.xml.gz")

```

```

t12_file = File("t12.xml.gz")
t13_file = File("t13.xml.gz")
t23_file = File("t23.xml.gz")
t11_file << t11
t22_file << t22
t33_file << t33
t12_file << t12
t13_file << t13
t23_file << t23

```

In the following, the main code is reported. The problem consists of a second order non-linear equation coupled with a Poisson-like equation and with reaction-diffusion equation. We create a mixed function space using linear continuous Lagrange basis such that each tetrahedron has four degrees of freedom. Since we deal with a nonlinear problem, we have to make use of the *NewtonSolver()* built in class. We choose MUMPS (MULTifrontal Massively Parallel Sparse direct Solver) as linear solver and the incremental criterion as convergence criterion. In the main code, there are few C++ lines in which the external files containing the components of the tensors **D** and **T** are read and stored in objects that FEniCS can introduce in the equations. In particular, thanks to the *Expression* tool, the components are linearly interpolated on the *dof* of the variables.

```

# Model.py

from dolfin import *
import numpy

# ---- Create Mesh and function space ---- #

mesh = Mesh("brain.xml")
V     = FunctionSpace(mesh, "Lagrange", 1)
ME    = MixedFunctionSpace([V, V, V])

mvc_lab = MeshValueCollection("size_t", mesh, "brain_labels.xml")
meshf_lab = MeshFunction("size_t", mesh, mvc_lab)
values_label = meshf_lab.array()

#Resection simulation only
#mvc = MeshValueCollection("size_t", mesh, "tumor.xml")
#meshf = MeshFunction("size_t", mesh, mvc)
#values = meshf.array()

class InitialConditions(Expression):

```

```

def eval(self, values, x):
    values[0]=0.45*exp( -( (x[0]-242)**2 + ( x[1]-229)**2+ (x
    [2]- 27)**2 )/9)
    #Resection simulation only
    values[0]= 0.39*((x[0]-205)**2+(x[1]-290)**2+(x[2]-28)
    **2<=115)+0.0*((x[0]-205)**2+(x[1]-295.5)**2+(x[2]-27)
    **2>=115)
    values[1]=0.0
    values[2]=1.0
def value_shape(self):
    return(3,)

class MyTumor(NonlinearProblem):
def __init__(self, L, a, bc):
    NonlinearProblem.__init__(self)
    self.L = L
    self.a = a
    self.bc = bc
def F(self, b, x):
    assemble(self.L, tensor=b)
    self.bc.apply(b, x)
def J(self, A, x):
    assemble(self.a, tensor=A)
    self.bc.apply(A)

class DirichletBoundary(SubDomain):
def inside(self, x, on_boundary):
    return on_boundary

# ---- Problem ---- #

#Define trial Function and test function
du = TrialFunction(ME)
v,w,q = TestFunctions(ME)

#Define functions
u = Function(ME)
u0 = Function(ME)

#Split mixed function
dc,dmu,dn = split(du)
c,mu,n = split(u)
c0,mu0,n0 = split(u0)

#Create initial conditions and interpolate
u_init = InitialConditions()
u.interpolate(u_init)
u0.interpolate(u_init)

# Resection simulation only
#dm = V.dofmap()
#tt = Function(V)
#for cell in cells(mesh):
    #if (values[cell.index()]==1):

```

```

    #tt.vector()[dm.cell_dofs(cell.index())[:]]=0.0
    #if (values[cell.index()]==0):
        #tt.vector()[dm.cell_dofs(cell.index())[:]]=1.0

#dofs_V0=ME.sub(0).dofmap().dofs()
#lun=len(dofs_V0)
#for ind in range(0, lun ):
    #u.vector()[dofs_V0[ind]]=u.vector()[dofs_V0[ind]]*tt.vector
    #() [ind]
    #u0.vector()[dofs_V0[ind]]=u0.vector()[dofs_V0[ind]]*tt.
    #vector() [ind]

# --- Diffusion steps (Resection only) --- #

#s_1= Function(V)
#assign(s_1, u.sub(0))
#dt = 0.1      # time step
#s = TrialFunction(V)
#r = TestFunction(V)
#a = s*r*dx + dt*inner(nabla_grad(s), nabla_grad(r))*dx
#L = s_1*r*dx
#A = assemble(a) # assemble only once, before the time stepping
#s = Function(V) # the unknown at a new time level
#T = 0.3        # total simulation time
#t = dt
#print "Ok+++"
#while t <= T:
    #b = assemble(L)
    #solve(A, s.vector(), b)
    #t += dt
    #s_1.assign(s)

#file_ss = File("out_ss.pvd", "compressed")
#file_ss << s
#print "Ok"
# Assignment
#assign(u.sub(0), s)
#assign(u0.sub(0),s)

# ---- Parameter estimation ---- #

#Oxygen phase
#class defineS(Expression):
    #def eval(self,values,x):
        #values[0]= -1e4*exp ( - ((x[0]-205)**2+(x[1]-290)**2+(x
        # [2]-28)**2 ) /115      ) +1e4
        #values[1]=0.0
        #values[2]=0.0
    #def value_shape(self):
        #return(3,)

#Define functions
#S_n_exp = Function(ME)

```

```

#S_init = defineS()

#S_n_exp.interpolate(S_init)
#S_n= Function(V)
#assign(S_n, S_n_exp.sub(0))

#dm = V.dofmap()
#k = Function(V)
#for cell in cells(mesh):
    #if (values[cell.index()]==1):
        #k.vector()[dm.cell_dofs(cell.index())[:]]=20
    #if (values[cell.index()]==0):
        #k.vector()[dm.cell_dofs(cell.index())[:]]=100

dm = V.dofmap()
k = Function(V)
for cell in cells(mesh):
    if (values_label[cell.index()] == 25 ):
        k.vector()[dm.cell_dofs(cell.index())[:]]=20
    if (values_label[cell.index()] == 13):
        k.vector()[dm.cell_dofs(cell.index())[:]]=100
    if (values_label[cell.index()] == 14):
        k.vector()[dm.cell_dofs(cell.index())[:]]=100

delta_n = 1000    #day^-1
S_n      = 1e4    #day^-1
gamma    = 0.25   #day^-1
# Cellular Phase
c_e      = 0.389
M        = 5000   #mm^-2 Pa day - range [1377.9 ; 4286.7]
n_s      = 0.07   #mM micromolarity
X1       = 106.64 #Pa
X2       = 900    #Pa - range [866 ; 1530]
E        = 694    #Pa
delta_c  = 0.3

theta    = 0.5
dt       = 1e-1

# ----- #
# Code for C++ evaluation of D
defineMatrix_code_0 = """

class Components_DT_0 : public Expression
{
public:

    // Create expression with 6 components
    Components_DT_0() : Expression(6) {}

    // Function for evaluating expression on each cell
    void eval(Array<double>& values, const Array<double>& x, const
        ufc::cell& cell) const
    {

```

```

const uint D = cell.topological_dimension;
const uint cell_index = cell.index;
values[0] = (*o11)[cell_index];
values[1] = (*o12)[cell_index];
values[2] = (*o13)[cell_index];
values[3] = (*o22)[cell_index];
values[4] = (*o23)[cell_index];
values[5] = (*o33)[cell_index];
}

// The data stored in mesh functions
std::shared_ptr<MeshFunction<double> > o11;
std::shared_ptr<MeshFunction<double> > o12;
std::shared_ptr<MeshFunction<double> > o13;
std::shared_ptr<MeshFunction<double> > o22;
std::shared_ptr<MeshFunction<double> > o23;
std::shared_ptr<MeshFunction<double> > o33;

};
"""

# Define DT components expression and matrix

o11=MeshFunction("double",mesh,"o11.xml.gz")
o22=MeshFunction("double",mesh,"o22.xml.gz")
o33=MeshFunction("double",mesh,"o33.xml.gz")
o12=MeshFunction("double",mesh,"o12.xml.gz")
o13=MeshFunction("double",mesh,"o13.xml.gz")
o23=MeshFunction("double",mesh,"o23.xml.gz")

o = Expression(cppcode=defineMatrix_code_O)
o.o11 = o11
o.o12 = o12
o.o13 = o13
o.o22 = o22
o.o23 = o23
o.o33 = o33
mat_O = as_matrix([[o[0], o[1], o[2]], [o[1], o[3], o[4]], [o[2], o
    [4], o[5]] ])

# ----- #

# Code for C++ evaluation of T
defineMatrix_code_T = """

class Components_DT_T : public Expression
{
public:

    // Create expression with 6 components
    Components_DT_T() : Expression(6) {}

    // Function for evaluating expression on each cell

```

```

void eval(Array<double>& values, const Array<double>& x, const
        ufc::cell& cell) const
{
    const uint D = cell.topological_dimension;
    const uint cell_index = cell.index;
    values[0] = (*t11)[cell_index];
    values[1] = (*t12)[cell_index];
    values[2] = (*t13)[cell_index];
    values[3] = (*t22)[cell_index];
    values[4] = (*t23)[cell_index];
    values[5] = (*t33)[cell_index];
}

// The data stored in mesh functions
std::shared_ptr<MeshFunction<double> > t11;
std::shared_ptr<MeshFunction<double> > t12;
std::shared_ptr<MeshFunction<double> > t13;
std::shared_ptr<MeshFunction<double> > t22;
std::shared_ptr<MeshFunction<double> > t23;
std::shared_ptr<MeshFunction<double> > t33;

};
"""

# Define T components expression and matrix

t11=MeshFunction("double",mesh,"t11.xml.gz")
t22=MeshFunction("double",mesh,"t22.xml.gz")
t33=MeshFunction("double",mesh,"t33.xml.gz")
t12=MeshFunction("double",mesh,"t12.xml.gz")
t13=MeshFunction("double",mesh,"t13.xml.gz")
t23=MeshFunction("double",mesh,"t23.xml.gz")

t = Expression(cppcode=defineMatrix_code_T)
t.t11 = t11
t.t12 = t12
t.t13 = t13
t.t22 = t22
t.t23 = t23
t.t33 = t33
mat_T = as_matrix([[t[0], t[1], t[2]], [t[1], t[3], t[4]], [t[2], t
    [4], t[5]]  ])

# ----- #

# Form compiler options
parameters["form_compiler"]["optimize"] = True
parameters["form_compiler"]["cpp_optimize"] = True
parameters["form_compiler"]["representation"] = "quadrature"

# ---- Define nutrient initial condition ---- #

# Define Dirichlet boundary condition

```



```

def Boundary(x, on_boundary):
    return on_boundary

bc = DirichletBC(V, Constant("1.0"), Boundary)

# Define variational problem
m = TrialFunction(V)
t = TestFunction(V)

a = inner(mat_O*grad(m), grad(t))*dx + delta_n*c0*m*t*dx + S_n*m*t
  *dx
L = S_n*t*dx

# Compute solution
m = Function(V)
problem = LinearVariationalProblem(a, L, m, bc)
solver_m = LinearVariationalSolver(problem)

prm_m=solver_m.parameters
prm_m['linear_solver'] = 'mumps'
solver_m.solve()

# Assignment
assign(u.sub(2), m)
assign(u0.sub(2),m)

# ---- NonLinearProblem ---- #

# Dirichlet boundary condition
g1 = Constant(0.0)
bc2 = DirichletBC(ME.sub(0), g1, DirichletBoundary())

g2 = Constant(1.0)
bc2 = DirichletBC(ME.sub(2), g2, DirichletBoundary())

bc=[bc1, bc2]

#Crank -Nicholson method
n_mid = (1.0-theta)*n0 + theta*n
mu_mid = (1.0-theta)*mu0 + theta*mu
c_mid = (1.0-theta)*c0 + theta*c

c = variable(c)
K_c = c*(1-c)**2/M
f = E*(c**2)*((c-c_e)/(1-c))

X = Function(V)
dofs_V0=ME.sub(0).dofmap().dofs()
nn=len(dofs_V0)
for ii in range(0,nn):
    if (u.vector()[dofs_V0[ii]]>1e-9):
        X.vector()[ii]=X2
    if (u.vector()[dofs_V0[ii]]<=1e-9):
        X.vector()[ii]=X1

```

```

lmba = Function(V)
for jj in range(0, nn):
    lmba.vector()[jj]=1e-4*(X.vector()[jj])

L0 = c*v*dx -c0*v*dx + dt*inner(K_c*grad(mu_mid), grad(v))*dx - dt
    *gamma*c_mid*(1-c_mid)*(n_mid-delta_c)*v*dx - dt*k*n_s*c_mid*
    inner(mat_T*grad(n_mid), grad(v))*dx
L1 = mu*w*dx - f*w*dx - lmba*inner(grad(c), grad(w))*dx
L2 = n*q*dx -n0*q*dx + dt*inner(mat_O*grad(n_mid),grad(q))*dx - dt
    *S_n*q*dx + dt*S_n*n_mid*q*dx + dt*delta_n*c_mid*n_mid*q*dx
L = L0+L1+L2

J = derivative(L,u,du)

# Create nonlinear problem and Newton solver
problem = MyTumor(L,J,bc)
solver = NewtonSolver()
prm=solver.parameters
prm['linear_solver'] = 'mumps'
solver.parameters["relative_tolerance"] = 1e-6
solver.parameters["convergence_criterion"] = "incremental"
solver.parameters['maximum_iterations'] = 50

# Saving output files
file_c = File("/u/dati/laureandi/colombo/Farfalla/out_c.pvd", "
    compressed")
file_n = File("/u/dati/laureandi/colombo/Farfalla/out_n.pvd", "
    compressed")

#Step in time
t=0.0
file_c << (u.split()[0], t)
file_n << (u.split()[2], t)
T=1000*dt
i=1

while (t<T):
    print i
    t+=dt
    u0.vector()[:]=u.vector()
    X = Function(V)
    dofs_V0=ME.sub(0).dofmap().dofs()
    nn=len(dofs_V0)
    for ii in range(0,nn):
        if (u.vector()[dofs_V0[ii]]>1e-9):
            X.vector()[ii]=X2
        if (u.vector()[dofs_V0[ii]]<=1e-9):
            X.vector()[ii]=X1
    lmba = Function(V)
    for jj in range(0, nn):
        lmba.vector()[jj]=1e-4*(X.vector()[jj])
    solver.solve(problem, u.vector())
    if (i%10 ==0):
        file_c << (u.split()[0], t)

```

```
file_n << (u.split()[2], t)
i=i+1
```

Bibliography

- [1] D. Ambrosi and L. Preziosi. On the closure of mass balance models for tumor growth. *Mathematical models and methods in applied sciences*, 12(5):737–754, 2002.
- [2] P. Bailey and H. Cushing. Tumors of the glioma group. j.b. lippincott. *British journal of surgery*, 14(55):554–555, 1927.
- [3] P. J. Basser and D. K. Jones. Diffusion-tensor MRI: theory, experimental design and data analysis - a technical review. *N.m.r. biomed.*, 15(7-8):456–467, 2002.
- [4] E. L. Bearer, J. S. Lowengrub, H. B. Frieboes, Y. L. Chuang, F. Jin, S. M. Wise, M. Ferrari, D. B. Agus, and V. Cristini. Multiparameter computational modeling of tumor invasion. *Cancer res.*, 69(10):4493–4501, 2009.
- [5] Y. Boucher, H. Salehi, B. Witwer, G. R. Harsh, and R. K. Jain. Interstitial fluid pressure in intracranial tumours in patients and in rodents. *Br. j. cancer*, 75(6):829–836, 1997.
- [6] R. M. Bowen. Theory of mixtures. *Continuum physics*, 3, 1976.
- [7] M. Bruehlmeier, U. Roelcke, P. Blauenstein, J. Missimer, P. A. Schubiger, J. T. Locher, R. Pellikka, and S. M. Ametamey. Measurement of the extracellular space in brain tumors using ^{76}Br -bromide and PET. *J. nucl. med.*, 44(8):1210–1218, 2003.
- [8] H. Byrne and L. Preziosi. Modelling solid tumour growth using the theory of mixtures. *Math. med. biol.*, 20(4):341–366, 2003.
- [9] L. Cervoni, P. Celli, and M. Salvati. Long-term survival in a patient with supratentorial glioblastoma: clinical considerations. *Ital. j. neurol. sci.*, 19(4):221–224, 1998.
- [10] C. Chatelain, T. Balois, P. Ciarletta, and M. Ben Amar. Emergence of microstructural patterns in skin cancer: a phase separation analysis in a binary mixture. *New journal of physics*, 13(11):115013, 2011.
- [11] O. Clatz, M. Sermesant, P. Y. Bondiau, H. Delingette, S. K. Warfield, G. Malandain, and N. Ayache. Realistic simulation of the 3-D growth of brain tumors in MR images coupling diffusion with biomechanical deformation. *I.e.e.e. trans. med. imaging.*, 24(10):1334–1346, 2005.

- [12] V. Cristini, X. Li, J. S. Lowengrub, and S. M. Wise. Nonlinear simulations of solid tumor growth using a mixture model: invasion and branching. *J. math. biol.*, 58(4-5):723–763, 2009.
- [13] V. Cristini, J. Lowengrub, and Q. Nie. Nonlinear simulation of tumor growth. *J. math. biol.*, 46(3):191–224, 2003.
- [14] E. Crocetti, A. Trama, and C. Stiller. Epidemiology of glial and non-glial brain tumours in Europe. *European journal of cancer*, 48(10):1532–1542, 2012.
- [15] L. Davis. Spongioblastoma multiforme of the brain. *Annals of surgery*, 87(1), 1928.
- [16] R. M. Ford and D. A. Lauffenburger. Analysis of chemotactic bacterial distributions in population migration assays using a mathematical model applicable to steep or shallow attractant gradients. *Bulletin of mathematical biology*, 53(5):721–749, 1991.
- [17] H. B. Frieboes, J. S. Lowengrub, S. Wise, X. Zheng, P. Macklin, E. L. Bearer, and V. Cristini. Computer simulation of glioma growth and morphology. *Neuroimage*, 37:59–70, 2007.
- [18] FSL. 2014. URL: <http://fsl.fmrib.ox.ac.uk/fsl/fslwiki/>.
- [19] F. B. Furnari, T. Fenton, R. M. Bachoo, A. Mukasa, J. M. Stommel, A. Stegh, W. C. Hahn, K. L. Ligon, D. N. Louis, C. Brennan, L. Chin, R. A. DePinho, and W. K. Cavenee. Malignant astrocytic glioma: genetics, biology, and paths to treatment. *Genes dev.*, 21(21):2683–2710, 2007.
- [20] P. Gerlee and A. R. Anderson. An evolutionary hybrid cellular automaton model of solid tumour growth. *J. theor. biol.*, 246(4):583–603, 2007.
- [21] M. L. Goodenberger and R. B. Jenkins. Genetics of adult glioma. *Cancer genet.*, 205(12):613–621, 2012.
- [22] H. L. Harpold, E. C. Alvord, and K. R. Swanson. The evolution of mathematical modeling of glioma proliferation and invasion. *J. neuropathol. exp. neurol.*, 66(1):1–9, 2007.
- [23] H. Hatzikirou, A. Deutsch, C. Schaller, M. Simon, and K. Swanson. Mathematical modelling of glioblastoma tumour development: a review. *Mathematical models and methods in applied sciences*, 15(11):1779–1794, 2005.
- [24] Diffusion Imaging. 2009-2014. URL: <http://www.diffusion-imaging.com>.
- [25] ITK. 2014. URL: www.itk.org.
- [26] R. K. Jain. Transport of molecules in the tumor interstitium: a review. *Cancer res.*, 47(12):3039–3051, 1987.
- [27] K. Jellinger. Glioblastoma multiforme: morphology and biology. *Acta neurochirurgica*, 42:5–32, 1975.

- [28] B. J. Jellison, A. S. Field, J. Medow, M. Lazar, M.S. Salamat, and A. L. Alexander. Diffusion tensor imaging of cerebral white matter: a pictorial review of physics, fiber tract anatomy, and tumor imaging patterns. *American journal of neuroradiology*, 25(3):356–369, 2004.
- [29] Y. Jiang, J. Pjesivac-Grbovic, C. Cantrell, and J. P. Freyer. A multiscale model for avascular tumor growth. *Biophys. j.*, 89(6):3884–3894, 2005.
- [30] D. K. Jones and A. Leemans. Diffusion tensor imaging. *Methods mol. biol.*, 711:127–144, 2011.
- [31] Vascular Modelling Tool Kit. 2014. URL: <http://www.vmtk.org/>.
- [32] Visualization Tool Kit. 2014. URL: <http://www.vtk.org/>.
- [33] D. Krex, B. Klink, C. Hartmann, A. von Deimling, T. Pietsch, M. Simon, M. Sabel, J. P. Steinbach, O. Heese, G. Reifenberger, M. Weller, and G. Schackert. Long-term survival with glioblastoma multiforme. *Brain*, 130(Pt 10):2596–2606, 2007.
- [34] H. C. Lawson, P. Sampath, E. Bohan, M. C. Park, N. Hussain, A. Olivi, J. Weingart, L. Kleinberg, and H. Brem. Interstitial chemotherapy for malignant gliomas: the Johns Hopkins experience. *J. neurooncol.*, 83(1):61–70, 2007.
- [35] D. Le Bihan. Looking into the functional architecture of the brain with diffusion MRI. *Nat. rev. neurosci.*, 4(6):469–480, 2003.
- [36] D. Le Bihan, E. Breton, D. Lallemand, P. Grenier, E. Cabanis, and M. Laval-Jeantet. MR imaging of intravoxel incoherent motions: application to diffusion and perfusion in neurologic disorders. *Radiology*, 161(2):401–407, 1986.
- [37] D. Le Bihan, J. F. Mangin, C. Poupon, C. A. Clark, S. Pappata, N. Molko, and H. Chabriat. Diffusion tensor imaging: concepts and applications. *J. magn. reson. imaging*, 13(4):534–546, 2001.
- [38] A. Logg, K.-A. Mardal, and G. N. Wells, editors. *Automated solution of differential equations by the finite element method*. Volume 84 of *Lecture Notes in Computational Science and Engineering*. Springer, 2012.
- [39] D. N. Louis, H. Ohgaki, O.D. Wiestler, W. K. Cavenee, P. C. Burger, A. Jouvett, B. W. Scheithauer, and P. Kleihues. The 2007 WHO classification of tumours of the central nervous system. *Acta neuropathologica*, 114(2):97–109, 2007.
- [40] J. S. Lowengrub, H. B. Frieboes, F. Jin, Y. L. Chuang, X. Li, P. Macklin, S. M. Wise, and V. Cristini. Nonlinear modelling of cancer: bridging the gap between cells and tumours. *Nonlinearity*, 23(1):R1–R9, 2010.
- [41] M. Manica. Brain Tumors: mathematical modeling and numerical simulations for cancer growth and invasion. Master’s thesis. Politecnico di Milano, 2009.

- [42] A. Martinez-Gonzalez, G. F. Calvo, L. A. Perez Romasanta, and V. M. Perez-Garcia. Hypoxic cell waves around necrotic cores in glioblastoma: a biomathematical model and its therapeutic implications. *Bull. math. biol.*, 74(12):2875–2896, 2012.
- [43] D. Masao and A. Onuki. Dynamic coupling between stress and composition in polymer solutions and blends. *J. phys.*, 2(8):1631–1656, 1992.
- [44] Y. Masutani, S. Aoki, O. Abe, N. Hayashi, and K. Otomo. MR diffusion tensor imaging: recent advance and new techniques for diffusion tensor visualization. *Eur. j. radiol.*, 46(1):53–66, 2003.
- [45] D. A. McClain and G. M. Edelman. A neural cell adhesion molecule from human brain. *Proc. natl. acad. sci. u.s.a.*, 79(20):6380–6384, 1982.
- [46] S. R. McDougall, A. R. Anderson, and M. A. Chaplain. Mathematical modelling of dynamic adaptive tumour-induced angiogenesis: clinical implications and therapeutic targeting strategies. *J. theor. biol.*, 241(3):564–589, 2006.
- [47] S. Mori and J. Zhang. Principles of diffusion tensor imaging and its applications to basic neuroscience research. *Neuron.*, 51(5):527–539, 2006.
- [48] P. Mukherjee, J. I. Berman, S. W. Chung, C. P. Hess, and R. G. Henry. Diffusion tensor MR imaging and fiber tractography: theoretic underpinnings. *A.j.n.r. am. j. neuroradiol.*, 29(4):632–641, 2008.
- [49] American Association of Neurological Surgeons. 2014. URL: <http://www.aans.org/>.
- [50] Cancer Council NSW. 2011. URL: www.cancercouncil.com.au.
- [51] J.T. Oden, A. Hawkins, and S. Prudhomme. General diffuse-interface theories and an approach to predictive tumor growth modeling. *Mathematical models and methods in applied sciences*, 20(3):477–517, 2010.
- [52] H. Ohgaki and P. Kleihues. Epidemiology and etiology of gliomas. *Acta neuropathol.*, 109(1):93–108, 2005.
- [53] H. Ohgaki and P. Kleihues. Genetic alterations and signaling pathways in the evolution of gliomas. *Cancer sci.*, 100(12):2235–2241, 2009.
- [54] H. Ohgaki and P. Kleihues. Population-based studies on incidence, survival rates, and genetic alterations in astrocytic and oligodendroglial gliomas. *J. neuropathol. exp. neurol.*, 64(6):479–489, 2005.
- [55] H. Ohgaki and P. Kleihues. The definition of primary and secondary glioblastoma. *Clinical cancer research*, 19(4):764–772, 2013.
- [56] T. Okegawa, R. C. Pong, Y. Li, and J. T. Hsieh. The role of cell adhesion molecule in cancer progression and its application in cancer therapy. *Acta biochim. pol.*, 51(2):445–457, 2004.

- [57] M. Papadogiorgaki, P. Koliou, X. Kotsiakis, and M. E. Zervakis. Mathematical modelling of spatio-temporal glioma evolution. *Theor. biol. med. model.*, 10, 2013.
- [58] Paraview. 2013. URL: www.paraview.org.
- [59] R. Probstmeier, T. Fahrig, E. Spiess, and M. Schachner. Interactions of the neural cell adhesion molecule and the myelin-associated glycoprotein with collagen type I: involvement in fibrillogenesis. *J. cell biol.*, 116(4):1063–1070, 1992.
- [60] FEniCS Project. 2013. URL: <http://fenicsproject.org/>.
- [61] D. Purves, G.J. Augustine, D. Fitzpatrick, W.C. Hall, A.S. LaMantia, J.O. McNamara, and L.E. White. Neuroscience, 2008.
- [62] Radiopaedia.org. 2005-2014. URL: <http://radiopaedia.org/articles/glioblastoma>.
- [63] K.R. Rajagopal and L. Tao. Mechanics of mixtures, 1995.
- [64] Slicer3D. 2014. URL: <http://www.slicer.org/>.
- [65] N. R. Smoll, K. Schaller, and O. P. Gautschi. The cure fraction of glioblastoma multiforme. *Neuroepidemiology*, 39(1):63–69, 2012.
- [66] National Brain Tumor Society. 2014. URL: <http://www.braintumor.org/>.
- [67] E.O. Stejskal and J.E. Tanner. Spin diffusion measurements: spin echoes in the presence of a time-dependent field gradient. *The journal of chemical physics*, 42(1):288–292, 1965.
- [68] R. Stupp. Radiotherapy plus Concomitant and Adjuvant Temozolomide for Glioblastoma. *The new england journal of medicine*, 48, 2005.
- [69] C. Suarez, F. Maglietti, M. Colonna, K. Breitburd, and G. Marshall. Mathematical modeling of human glioma growth based on brain topological structures: study of two clinical cases. *Plos one*, 7(6), 2012.
- [70] E. A. Swabb, J. Wei, and P. M. Gullino. Diffusion and convection in normal and neoplastic tissues. *Cancer res.*, 34(10):2814–2822, 1974.
- [71] K. R. Swanson, E. C. Alvord, and J. D. Murray. A quantitative model for differential motility of gliomas in grey and white matter. *Cell prolifer.*, 33(5):317–329, 2000.
- [72] K. R. Swanson, C. Bridge, J. D. Murray, and E. C. Alvord. Virtual and real brain tumors: using mathematical modeling to quantify glioma growth and invasion. *J. neurol. sci.*, 216(1):1–10, 2003.
- [73] K. R. Swanson, R. C. Rockne, J. Claridge, M. A. Chaplain, E. C. Alvord, and A. R. Anderson. Quantifying the role of angiogenesis in malignant progression of gliomas: in silico modeling integrates imaging and histology. *Cancer res.*, 71(24):7366–7375, 2011.

- [74] Johns Hopkins Health System. 2014. URL: <http://www.hopkinsmedicine.org/>.
- [75] M. L. Tanaka, W. Debinski, and I. K. Puri. Hybrid mathematical model of glioma progression. *Cell prolifer.*, 42(5):637–646, 2009.
- [76] Tetgen. 2014. URL: <http://wias-berlin.de/software/tetgen/>.
- [77] A. Toma, L.R. Castillo Cisneros, T.A. Schuetz, S. Becker, A. Mang, A. Regnier-Vigouroux, and M. T. Buzug. A validated mathematical model of tumour-immune interactions for glioblastoma. *Current medical imaging reviews*, 9(2):145–153, 2013.
- [78] J. D. Tournier, S. Mori, and A. Leemans. Diffusion tensor imaging and beyond. *Magn. reson. med.*, 65(6):1532–1556, 2011.
- [79] Cancer Research UK. 2014. URL: <http://www.cancerresearchuk.org/cancer-help/type/brain-tumour>.
- [80] G. Vilanova, I. Colominas, and H. Gomez. Capillary networks in tumor angiogenesis: from discrete endothelial cells to phase-field averaged descriptions via isogeometric analysis. *Int. j. numer. method biomed. eng.*, 29(10):1015–1037, 2013.
- [81] F. G. Vital-Lopez, A. Armaou, M. Hutnik, and C. D Maranas. Modeling the effect of chemotaxis on glioblastoma tumor progression. *Aiche journal*, 57(3):778–792, 2011.
- [82] K. Wilmanski. Continuum theories of mixtures - lecture notes, 2005.
- [83] S. M. Wise, J. S. Lowengrub, H. B. Frieboes, and V. Cristini. Three-dimensional multispecies nonlinear tumor growth—I. Model and numerical method. *J. theor. biol.*, 253(3):524–543, 2008.